Title
Reorganization of Dentate Gyrus Microcircuits During Epileptogenesis

Author
Jones, Ryan Thomas

Publication Date
2014

Peer reviewed|Thesis/dissertation

University of California

Los Angeles

Reorganization of Dentate Gyrus Microcircuits During Epileptogenesis

A dissertation submitted in partial satisfaction

of the requirements for the degree

Doctor of Philosophy in Neurobiology

by

Ryan Thomas Jones

2014

Abstract of the Dissertation

Reorganization of Dentate Gyrus Microcircuits During Epileptogenesis

by

Ryan Thomas Jones

Doctor of Philosophy in Neurobiology

University of California, Los Angeles, 2014

Professor Felix E. Schweizer, Co-chair

Professor Istvan Mody, Co-chair

Temporal lobe epilepsy (TLE) is a form of acquired epilepsy characterized by recurrent and unprovoked seizures. TLE often develops following a precipitating neurological insult, such as traumatic brain injury, stroke, infection, prolonged febrile seizures or status epilepticus. These insults can initiate a constellation of genetic, functional, network and systems level reorganization that transforms a normal non-epileptic brain into one capable of generating recurrent and unprovoked seizures. The period of time between neurological insults and the onset of epilepsy is known as the latent period and is believed to be the period of time during which underlying epileptogenic processes occur.

The dentate gyrus (DG) region of the hippocampus plays a key role in contextual learning and memory and strongly regulates the flow of neural activity from cortical regions into seizure-prone hippocampal regions through emergent properties of its neural microcircuit. In TLE, this filtering function is disrupted and can contribute to generation of seizures. Recent studies have described pathological high-frequency oscillations (pHFOs) in the DG and identified them as potential biomarkers of underlying proconvulsant network abnormalities. Moreover, pHFOs appear to be harbingers of TLE and are generated in the DG prior to the

onset of an epileptic phenotype and therefore may reflect underlying network reorganization during the epileptogenesis. Currently, little is known about the emergence of pHFOs after epilepsy-inducing neuronal insults or the pathological microcircuit that generates them. To address this we used a new mouse model of TLE to track the temporal and spectral evolution of pHFOs during epileptogenesis. Moreover, we investigated how disrupted integration of newly generated granule cells into the DG during epileptogenesis contributes to the disruption of DG microcircuit function.

We found that DG pHFOs are generated in bursts *in vivo* during epileptogenesis but that their burst properties do not evolve over time. In contrast, pHFO spectral dynamics appear to evolve during the latent period, suggesting that pHFO properties change according to the epileptogenic stage. *In vitro* electrophysiologcal and optogenetic experiments revealed that NGCs abnormally integrate into the DG microcircuit during epileptogenesis and that optogenetic activation of these neurons is sufficient to induce pHFOs in the DG.

The dissertation of Ryan Thomas Jones is approved.

Jerome Engel Jr.

Carolyn R. Houser

Felix E. Schweizer, Committee Co-chair

Istvan Mody, Committee Co-chair

University of California, Los Angeles

2014

"Any man can, if he so wishes,

become the sculptor of his own mind"

- Santiago Ramón y Cajal

Contents

List of Figures

List of Tables

Acknowledgments

Every personal achievement is the culmination of the guidance, support and the love of others. I am eternally indebted to those who have helped me throughout my journey and who have contributed to my growth as a scientist and as a person. If we are defined by the company we keep, then I am honored to have been defined by such great company.

I am grateful for the guidance and wisdom of my advisor, Professor Istvan Mody. I am thankful for his generosity, patience and scientific knowledge. I have learned more than I could have ever expected under his mentorship, and I will always remember his lessons throughout my career. I am also thankful for the mentorship and professional guidance of Professor Felix Schweizer. I could not have picked better committee members than Professors Carolyn Houser and Jerome "Pete" Engel Jr. Lastly, I am thankful for the encouragement, guidance and friendship of Professor Peter Patrylo, who introduced me to research as an undergraduate and has continually provided personal and scientific advice. I am humbled by all of my mentors, and I hope to make them proud as I continue throughout my scientific career.

To my family and friends for their continuous support. To my father, who has always been there for me and provided unwavering support and encouragement throughout my personal and professional endeavors. I am grateful for my friends and colleagues, who have enriched my life throughout my graduate career. Particularly, I must thank my friends Marco Treven, Yong-Seok Lee, Isabella Ferando, Guido Faas and Mike Baca for their technical support, scientific input and friendship.

Finally, to my wife, Kate. The love of my life. My best friend. My Favorite.

Thank you.

Chapter 1 is a version of a manuscript in preparation: Jones RT, Barth AM, and Mody I. Temporal and spectral dynamics of dentate gyrus pHFOs during epileptogenesis.

Chapter 3 is a reprint, with permission, of the publication: Jones RT, Faas GF and Mody I (2014). Intracellular Bicarbonate Regulates Action Potential Generation via KCNQ Channel Modulation. *J. Neurosci.* 34:4409-4417.

Chapter 4 is a reprint, with permission, of the publication: Santhakumar V, Jones RT and Mody I (2010). Developmental regulation and neuroprotective effects of striatal tonic $GABA_A$ currents. *Neurosci.* 167:644-655.

Vita

2007	B.S., Physiology. Southern Illinois University, Carbondale
2007-2014	Graduate Student Researcher
	Departments of Neurobiology and Neurology
	David Geffen School of Medicine, UCLA
2010-2012	Neural Microcircuits Graduate Fellow
	NINDS 5T32NS058280-05
	University of California, Los Angeles
2010	Teaching Assistant, Neuroanatomy
	David Geffen School of Medicine, UCLA
2011	Teaching Assistant, Neuroanatomy
	David Geffen School of Medicine, UCLA
2012-2014	Editor and Contributing Author
	www.KnowingNeurons.com
2013	Society for Neuroscience Travel Award
	Brain Research Institute
2013	Business of Science Certificate
	Business of Science Center
	University of California, Los Angeles

Publications and Presentations

Willingham A, Tokhi A, **Jones RT**, Patrylo PR. Enhanced susceptibility to kainate-induced epileptiform activity in hippocampal slices from aged rats. American Epilepsy Society Meeting, 2006. Program No. 3.102

Jones RT, Tyagi I, Patrylo PR. Synaptic transmission is compromised preferentially in the aged CNS during metabolically challenging conditions: A potential mechanism for aging-related cognitive decline. Society for Neuroscience, 2006. Program No. 80.13/KK20.

Kopjas NN*, **Jones RT***, Bany B, Patrylo PR. Reeler mutant mice exhibit seizures during recovery from isoflurane-induced anesthesia. Epilepsy Research 69:87-91 (2006).

Santhakumar V, **Jones RT**, Mody I. Developmental regulation and neuroprotective effects of striatal tonic inhibition. Neuroscience 167, 644-655 (2010).

Jones RT, Mody I. Strategies for measuring properties of native extrasynaptic GABAA receptors in granule cells of the mouse dentate gyrus. Society for Neuroscience, 2010. Program No. 338.15/E36.

Kanak DJ, **Jones RT**, Tokhi A, Willingham AL, Zaveri HP, Rose GM, Patrylo PR. Electrical and pharmacological stimuli reveal a greater susceptibility for CA3 network excitability in hippocampal slices from aged vs. adult Fisher 344 Rats. Aging and Disease, 2(4):318-331 (2011).

Jones RT, Faas GF, Mody I. Bicarbonate is a physiologically relevant intraneuronal calcium buffer and regulates CA3 pyramidal cell excitability. Society for Neuroscience, 2012. Program No. 540.05.

Baca SM, **Jones RT**, Mody I, Charles A. Selective activation of astrocytes can trigger cortical spreading depression. American Academy of Neurology Meeting, 2013. Program No. S55.002.

Jones RT, Ormiston L, Mody I. Abnormal integration of adult-generated granule cells two weeks old at the time of epilepsy inducing insult disrupts local dentate microcircuit during epileptogenesis. Society for Neuroscience, 2013. Program No. 248.20.

Jones RT, Faas GF, Mody I (2014) Intracellular Bicarbonate Regulates Action Potential Generation via KCNQ Channel Modulation. J Neurosci 34:4409-4417.

Jones RT, Barth AM, Ormiston LD, Mody I. Temporal and spectral dynamics of dentate gyrus pHFOs during epileptogenesis. Society for Neuroscience, 2014.

Ormiston LD, **Jones RT**, Mody I. Behavioral tests as potential biomarkers for the development of post-status epilepticus temporal lobe epilepsy. Society for Neuroscience, 2014.

Baca SM*, **Jones RT***, Chen K, Dietz CJK, Sofroniew M, Mody I, Charles A. Cortical spreading depression triggered by selective activation of astrocytes. *in preparation*

Jones RT, Barth A, Mody I. Temporal and spectral dynamics of dentate gyrus pHFOs during epileptogenesis. *in preparation*

* Authors contributed equally to this study

CHAPTER 1

Temporal and Spectral Dynamics of Dentate Gyrus pHFOs During Epileptogenesis

Abstract:

The dentate gyrus (DG) plays a central role in regulating the propagation of neural activity from extrahippocampal areas through the hippocampus. In temporal lobe epilepsy (TLE), however, this gatekeeper function is compromised, resulting in excessive activation of the seizure-prone CA3 and CA1 regions. The DG has been shown to generate pathological high frequency oscillations (pHFOs, 100-600 Hz) in both animal models and TLE patients, which have been proposed as a biomarker of epileptogenesis. Here we use a unilateral suprahippocampal kainic acid (KA) mouse model of TLE to characterize the development of pHFOs in the DG during epileptogenesis. Local field potential (LFP) recordings from the DG hilar region were made during the epileptogenic period in head-fixed awake-behaving mice at regular intervals after KA-induced status epilepticus (SE). We found that pHFOs, detected as early as 4 days post-SE, ride on top of large DC deflections, occur exclusively

during quiet wakefulness, and persist through the onset of TLE. We used burst quantification methods developed for single ion channel analyses to show that DG pHFOs occur in bursts, but that burst parameters (duration, inter-burst interval and number of pHFOs per burst) remain remarkably constant during epileptogenesis. Moreover, the probability of number of pHFOs per burst is random (i.e., follows a negative binomial distribution) throughout epileptogenesis. In contrast, pHFO duration and spectral dynamics appear to evolve from short events at 4 days post-SE to prolonged discharges with complex spectral characteristics by 14 days post-SE. Finally, we found that simultaneous dural EEG recordings were extremely unreliable for DG pHFO detection. Taken together, our results demonstrate that pHFOs exhibit a quantifiable evolution after epilepsy-inducing SE, which may reflect underlying network reorganization. If the evolution of pHFO spectral dynamics faithfully follows the epileptogenic process, then their analysis could be used characterize the developmental stage of epileptogenesis prior to the onset of spontaneous seizures.

Introduction:

Temporal lobe epilepsy (TLE) is the most common form of acquired epilepsy and often develops following neurological insults such as head trauma, infection, ischemia, prolonged febrile seizures or status epilepticus (SE) (Hesdorffer et al., 1998; French et al., 1993). This period of time between neurological insult and the development of an epileptic phenotype has been termed the latent period due to the lack of overt behavioral seizures that typically define clinical onset of an epileptic phenotype (Bragin et al., 2000; Engel, 1996; Stables et al., 2003). Wilder Penfield highlighted his "silent period of strange ripening" over 50 years ago and emphasized that a fundamental question of acquired epilepsies was determining why some develop spontaneous seizures following neurological insult while others do not (Penfield, 1961). Unfortunately, the underlying mechanisms of epileptogenesis remain unclear. It is clear, however, that considerable network reorganization and functional changes occur during the silent period that convert the normal brain into one capable of generating recurrent and

unprovoked seizures (Lukasiuk and Pitkänen, 2012; Goldberg and Coulter, 2013; Noebels et al., 2012)

The dentate gyrus (DG) region of the hippocampus is a critical structure involved in TLE since it regulates the propagation of extrahippocampal activity into the sensitive hippocampal networks and its filtering function is severely disrupted in TLE (Behr et al., 1998; Heinemann et al., 1992; Lothman et al., 1992). The emergence of DG network dysfunction reflects the accumulation of both functional and anatomical abnormalities after a precipitating insult and results in a proconvulsant DG microcircuit (Sloviter et al., 2006; Babb et al., 1991; Houser, 1990; Buckmaster and Dudek, 1997; Sutula et al., 1989; Tauck and Nadler, 1985).

The DG has been previously shown to generate pathological high-frequency oscillations (pHFOs, 100-600 Hz) during epilepsy. Although normal high-frequency oscillations (HFOs), or ripples, from 80-200 Hz have been well characterized in the hippocampus and parahippocampal regions, HFOs are never observed in the non-epileptic DG (Buzsáki, 2006; Chrobak and Buzsáki, 1996; Staba et al., 2004). Normal ripples reflect coordinated synchronous inhibitory and excitatory post-synaptic potentials (IPSCs and EPSCs, respectively) from local interneurons and principal cells and are necessary for memory consolidation (Siapas and Wilson, 1998; Buzsáki, 2006; Chrobak and Buzsáki, 1996; Jadhav et al., 2012), while pHFOs appear to originate near regions of seizure genesis, are believed to reflect synchronous dischargers of principle cells and correlate with the accumulation of proconvlusant DG network alterations (Bragin et al., 1999, 2002, 2003, 2004, 2007). Importantly, the onset of pHFOs in the DG precedes the emergence of epilepsy and spontaneous seizures in an intra-hippocampal kainite (KA) rat model of TLE, and the latency to the first pHFO correlates well with the latency and frequency of behavioral seizures (Bragin et al., 2003, 2004). Interestingly, rats that experience an epileptogenic insult but dont possess pHFOs do not develop spontaneous seizures, providing further evidence that pHFOs are connected with the epileptogenic process (Bragin et al., 2004). Despite extensive investigations into pHFOs and their relationship with

the onset of TLE, little is known about the temporal patterns of pHFO generation within the DG during the latent period. Moreover, the frequency of pHFOs can varry (100-600 Hz) and it is unclear if and to what extent the spectral properties of pHFOs evolve during epileptogenesis.

In the present study, we investigated the temporal profile, burst and spectral properties of DG pHFOs in awake-behaving mice during epileptogenesis after unilateral suprahippocampal KA-induced SE. We found that pHFOs are present in the DG hilus as early as 4 days post-SE and persist throughout the latent period. The pHFOs appear occur in bursts, but surprisingly, their burst properties do not evolve over time. In contrast, the spectral properties of pHFOs evolve during the latent period, which may reflect underlying proconvulsant network reorganization.

Materials and Methods:

Suprahippocampal kainite mouse model of TLE: In this study, we utilized a modified version of a previously described unilateral intrahippocampal KA mouse model of TLE (Suzuki et al., 1995; Riban et al., 2002; Marx et al., 2013; Volz et al., 2011). The suprahippocampal model of TLE was developed in the laboratory of Dr. Christian Steinhäuser and was adopted for this study after personal correspondance with Dr. Steinhäuser. We chose this model of TLE over the pilocarpine mouse model for several reasons: 1) Unilateral KA injection produced reliable and reproducible SE with a very low mortality rate. 2) The resulting KA-induced lesion is reminiscent of human TLE, which typically presents with unilateral hippocampal sclerosis (HS) and seizure onset (Wieser and ILAE Commission on Neurosurgery of Epilepsy, 2004). 3) KA-injected mice exhibit spontaneous focal seizures following a latent period, which mirror complex partial seizures observed in human TLE patients.

Animal surgery and KA injection: Surgeries were performed under aseptic conditions on male mice weighing 25-30 g (2-3 months of age). Mice were anesthetized with isoflurane (1.2 %, 100% O_2) and mounted into a standard Stoelting instrument stereotaxic frame with

blunt ear bars. Body temperature was maintained at 37 °C using a rectal probe and a water-circulated heating pad. The cranium was exposed with a small midline scalp incision, the bone was dried and holes were drilled for the future recording sites (coordinates adjusted to take into account the angles of the electrodes with the vertical and transversal planes; from the rostral confluence of the venous sinus rostrocaudal, RC, 5.1 mm; mediolateral, ML, 2.7 mm) and for grounding (RC: 3 mm caudal, ML: 1.6 mm). Next, the tips of the head holder for the spherical treadmill, covered by thin parafilm, were positioned above the caudal part of the skull bilaterally and dental-acrylate (Ortho-Jet, Lang Dental Manufacturing Co., Inc.) was used to embed the tips of the head holder. After the dental-acrylate had hardened, the head holder was removed, leaving slots bilaterally in the implant. These slots allowed repeated head fixation on the spherical treadmill without the need of anesthesia. Finally, the skull surface and the holes were covered with a silicone sealant (Kwik-Sil, World Precision Instruments, Inc.). Immediately after surgery, the mouse was continuously monitored until recovered, as demonstrated by their ability to maintain sternal recumbency and to exhibit purposeful movement. During the recovery period after surgery, warm saline solution (0.01-0.02 ml/g/twice/day) was administered subcutaneously to prevent dehydration. Because the head implant surgery could take up to 2 hours to complete, mice routinely took up to 1 hour to fully away from surgery. Consequently, KA was not injected at this time point to minimize confounding effects of lingering anesthesia on KA-induced SE.

After 3 days of recovery, mice were lightly anesthetized with isofluorane (1.2%, 100% O_2) and the Kwick-Sil was removed to expose the hole for KA injection. Next 70-75 nl of 20 mM kainic acid (KA, Tocris, in 0.9% sterile saline) was stereotaxically (Kopf Instruments) injected just above either the right or left dorsal hippocampus using the following coordinates, measured from bregma in mm: -1.9 RC, -1.5 mediolateral and 0.8 below the dura. Control mice were injected with 70-75 nl of 0.9% sterile saline. The KA or saline solution was injected using a pulled and beveled glass pipette (Wiretrol II, Drummond Scientific) over a 3 minute period an the injection needle was allowed to rest for an additional 5 minutes to prevent reflux

along the needle track. Following completion of injection, mice were given saline injections (0.3 cc, s.c.), removed from isofluorane and placed in an observation box for continuous video monitoring during SE. KA-injection surgeries typically took less than 20 minutes to complete and mice awoke from anesthesia within 5 minutes of surgery completion and SE typically began 30 min to 1 hour post-surgery. Four hours following the onset of SE, mice were injected with lorazepam (6 mg/kg) to abort seizures. Additional saline injections were provided as needed to replenish fluid loss. Mice were housed on a 12/12 h light/dark cycle and provided with food and water *ad libitum*. In a subset of experiments, Sstr2-EGFP mice (Tg(Sstr2-EGFP)119Gsat, Gensat) were injected with KA or saline using the aforementioned procedures but were not used for *in vivo* recording experiments. Two-weeks post-SE, Sstr2-EGFP were killed and prepared for histological analyses (see tissue preparation and imaging). All protocols were approved by the University of California, Los Angeles, Chancellors Animal Research Committee (ARC) and comply with National Institutes of Health guidelines.

In vivo local field potential (LFP) recordings: Local field potential (LFP) recordings were performed in awake head-fixed animals at different time points after the KA injection (Days: 4, 7, 11 and 14). Recordings were started at 4 days post-SE since because mice typically require 2-3 days to fully recover from the lingering effects of KA-induced SE (Riban et al., 2002). Mice were positioned and head-fixed to a spherical treadmill without anesthesia. The Kwik-Sil protective layer was removed and borosilicate glass recording electrodes (King Precision Glass, Claremont, CA), filled with 150 mM NaCl solution, were advanced through the preformed holes (ipsilaterally to the KA injection site) into the hilar region of the DG (1880 μm axially from dura). Mouse activity was recorded with two optical computer mice positioned close to the ball along the equator at 90 $^\circ$ apart (Dombeck et al., 2007; Harvey et al., 2009). All data were analyzed with custom procedures written in Igor Pro (Wavemetrics, Lake Oswego, OR).

Tissue preparation and imaging: Following the completion of *in vivo* electrophysiological recording on day 14, mice were deeply anesthetized with sodium pentobarbatol (90 mg/kg,

i.p.) and transcardially perfused with phosphate buffered saline (PBS, 0.12 M, pH 7.1) followed by 4% paraformaldehyde (PFA). The brains were removed and postfixed overnight in 4% PFA at 4 °C. After rinsing in PBS, brains were cryoprotected for two days in 30% sucrose solution at 4 °C, frozen in OCT compound and 50 μm coronal sections were cut with a cryostat (Leica Microsystems). Granule cell (GC) dispersion and mossy fiber sprouting, classic markers of epileptogenesis (Tauck and Nadler, 1985; Houser, 1990), were visualized with a DAPI nuclear stain and immunofluorescent labeling of ZnT-3 (McAuliffe et al., 2011), respectively. Briefly, free-floating sections were incubated in blocking solution containing 10% normal goat serum in Tris-buffered saline (TBS; pH 7.3) and 0.3% Triton X-100 for 2 hours at 25 °C. Slices were rinsed in TBS for 30 minutes and incubated at 25 °C overnight in primary monoclonal rabbit anti-ZnT3 (1:1000, Synaptic Systems), followed by incubation in goat anti-rabbit Alexa Fluor 555 (Invitrogen). Slices were mounted on slides using a DAPI-containing mounting medium (Vector Labs) and coverslipped for imaging. Sstr2-EGFP mice were used to visualize mossy cells in the hilar region and their terminals in the inner molecular layer of the DG. Coronal sections from Sstr2-EGFP mice were washed in TBS after cryosectioning and immediately mounted on slides for imaging. Epifluorescent images were obtained using an Olympus BX51 microscope equipped with a CCD camera (QImaging, Surry BC) and confocal z-stacks were acquired on a Leica TCS SP5 II using LAS AF software (Leica Microsystems). Images were compiled and analyzed using ImageJ.

pHFO detection, extraction and wavelet analysis: pHFOs were detected by band-pass filtering the record from 200 to 600 Hz and calculating the Hilbert transform of the band-passed trace. The standard deviation (S.D.) of the band-pass filtered trace was calculated and pHFOs were detected when the Hilbert magnitude exceeded 2.5xS.D. The termination of the pHFO was defined as the point at which the Hilbert magnitude reverted below 2.5xS.D. The pHFO duration was calculated as the difference between these two time points. Detected pHFOs were then extracted and used for further analysis. Time-frequency analysis was performed using continuous wavelet transform procedures in Igor Pro. The Morlet mother

wavelet was used and scales were chosen to reflect frequencies between 1 and 1000 Hz (ω_0 = 6). The S.D. of the wavelet transform was calculated for each frequency band, and the Z-score calculated to represent relative changes in magnitude. The Z-score was plotted as a function of time and frequency (corresponding to scale). Warmer colors represent greater Z-scores.

pHFO burst analysis: We utilized classic single ion channel burst analysis techniques to assess the temporal patterns of pHFOs within the DG hilus during epileptogenesis (Colquhoun, 1994; Lieberman and Mody, 1999; Sigworth and Sine, 1987). Typically, single ion channel analysis is performed by assessing the distributions of channel openings, closed times and burst durations, and these metrics reveal underlying biophysical properties (Colquhoun, 1994). Here, we applied this technique to the analysis of pHFOs by substituting channel open times for pHFO durations and channel closed times for pHFO inter-event intervals. pHFO burst properties were calculated by constructing log-binned histograms (10 bins per decade) plotted on a square root ordinate (McManus et al., 1987). Exponential curves were fit to each inter-event interval histogram using the following equation:

$$f(x) = B\sum_{i=0}^{n}\left(A_i e^{-\left(\frac{x}{\tau_i}-e^{\frac{x}{\tau_i}}\right)}\right) \tag{1.1}$$

where B is a normalization factor, A_i is the scaling factor of each exponential fit and τ_i is the mean inter-event interval for each distribution. Next, critical inter-event times (T_c) were calculated from the respective time constants by solving the following equation for T_c.

$$1 - e^{-\frac{T_c}{\tau_i}} = e^{-\frac{T_c}{\tau_{i+1}}} \tag{1.2}$$

where τ_i is the i^{th} time constant for the distribution of inter-event intervals. Thus, the T_c provides an internal threshold for determining the appropriate point to divide adjacent distributions. Finally, pHFO bursts were defined using T_c as a cutoff for inter-burst and intra-burst, and in some cases intra-cluster, intervals. Histograms of the number of pHFOs

per burst were generated and fit with a negative binomial distribution (Bernoulli) of the form:

$$P\left(x; r, p\right) = p^{r}\left(1-p\right)^{x-r} \tag{1.3}$$

where p^{r} is the probability of a pHFO within a burst.

Statistical analysis: Statistics were calculated using GraphPad Prism 6 (La Jolla, CA) and statistics procedures in R. Data are presented as mean ± standard error of mean. Significance level (α) was set to 0.05. For ANOVAs with significance levels below 0.05, post-hoc paired tests were performed and corrected for multiple comparisons. Nonparametric statistical analyses were used from datasets deviating from normality. Abbreviations: Kruskal-Wallis one-way ANOVA = K-W ANOVA

Results:

Suprahippocampal kainate injection recapitulates a previously described mouse model of TLE. We first sought to verify that our modification of an established intrahippocampal KA mouse model of TLE produced similar histopathology to what has been previously described (Fritschy, 2004; Suzuki et al., 1995; Riban et al., 2002; Marx et al., 2013; Volz et al., 2011). To avoid hippocampal damage by the KA injection needle, we raised the final injection site from -1.9 mm (Riban et al., 2002; Suzuki et al., 1995) to -0.8 mm from the dura, which results in KA injection just over the surface of the hippocampus. Unilateral suprahippocampal KA injection (see methods) produced reliable and consistent limbic SE, characterized by mild forelimb clonus and circling. Generalized tonic-clonic seizures were rare during SE, with only 10% of mice experiencing at least one generalized seizure during the 4 hour SE. A cohort of post-SE mice (n = 5) were continuously video monitored for up to 3 months post-SE and were confirmed to develop spontaneous seizures as previously described (Bouilleret et al., 1999; Riban et al., 2002).

Histological analysis of KA and saline injected mice was performed 2 weeks post-SE fol-

lowing the completion of *in vivo* recordings. DAPI nuclear labeling in the hippocampi of saline injected mice showed no overt abnormalities, indicating that the saline injection and subsequent repeated electrode insertions over the two-week recording period did not cause significant hippocampal damage (Figure 1.1 A). In contrast, KA-injected mice exhibited prominent hippocampal sclerosis on the ipsilateral, KA injected side and relatively normal anatomy in the contralateral, un-injected hippocampus (Figure 1.1 B, left - KA injected, right - uninjected). Furthermore, the KA-injected hippocampus showed significant cell loss in the hilus, CA3 and CA1 regions and prominent GC dispersion while the uninjected granule cell layer was normal (Figure 1.1 B, C and D). Finally, we assessed the level of mossy fiber sprouting in this model using anti-ZnT-3 immunofluorescence. Previous studies have demonstrated strong expression of ZnT-3 in mossy fiber boutons, which reliably labels aberrant mossy fiber synapses (mossy fiber sprouting) that develop in the inner third of the molecular layer during epileptogenesis (Tauck and Nadler, 1985; Sutula et al., 1989; McAuliffe et al., 2011). Similar to these findings, mossy fiber sprouting was apparent in the inner molecular layer of the KA-injected hippocampus, while the contralateral DG showed no signs of mossy fiber sprouting (Figure 1.1 C and D)(Volz et al., 2011; Mitsuya et al., 2009).

Hilar mossy cells are known to be particularly sensitive to insult-induced cell death and are some of the first neurons to die after an epilepsy-inducing neurological insult (Margerison and Corsellis, 1966; Scharfman and Myers, 2012). We utilized an Sstr2-EGFP transgenic mouse strain that strongly expresses GFP in hilar mossy cells assess mossy cell death two-weeks post-SE. Saline injected mice (n = 2) demonstrated numerous GFP^+ mossy cells in the hilar region of the DG that was consistent along the whole rostral-caudal axis of the hippocampus (Figure 1.1 E) and confocal images revealed robust axonal arborization in the inner 1/3 of the molecular layer (Figure 1.1 G). In contrast, mossy cells were absent from the hilus of the dorsal hippocampus on both the KA-injected and uninjected sides two-weeks post-SE (n = 2, Figure 1.1 F). Mossy cells were present at more caudal regions of the un-injected dorsal hippocampus while the KA-injected sides continued showed no GFP^+ cell

bodies within the hilus (Figure 1.1 F). Both ventral hippocampi, however, showed conserved mossy cell labeling, indicating that mossy cell death occurred predominantly in the dorsal hippocampus, near the site of KA injection. Confocal images of the inner molecular layer of the dorsal hippocampus showed reduced mossy cell axon labeling in the inner molecular layer of both the KA-injected and uninjected hippocampi. Despite the complete absence of mossy cells within the dorsal hippocampus, some axonal labeling persisted in the inner molecular layer (Figure 1.1 H and I, arrows). These axons may originate from mossy cells in the ventral hippocampus that are known to send axons rostrally along the septo-temporal axis (Scharfman and Myers, 2012). Interestingly, we observed that a noticeable proportion of granule cells on the KA-injected side became GFP^+, while granule cells in the uninjected or saline treated hippocampi showed very few GFP^+ GCs. It is unclear at this time why a subset of GCs may begin expressing SstR2 after SE when previous immunohistochemical studies have not reported Sstr2 expression in epileptic DG (Csaba et al., 2004, 2005). This distribution of mossy cell death confirms a previous study utilizing unilateral intrahippocampal KA injection (Volz et al., 2011) and contrasts other studies using systemic chemiconvulsant-induced TLE, which demonstrated extensive mossy cell loss in both hippocampi along the whole septo-temporal axis (Buckmaster and Jongen-Rêlo, 1999).

Spontaneous recurrent seizures are the defining characteristic of epilepsy. Previous studies and data from our own lab have established that unilateral or suprahippocampal KA injection leads to the onset of behavioral seizures around two-weeks post-SE (Riban et al., 2002). Figure 1.2 illustrates an example seizure that was recorded in the DG hilus of a head-fixed mouse on the spherical treadmill at 14 days post-unilateral suprahippocampal KA injection. This seizure exhibited behavioral characteristics similar to complex partial seizure with secondary generalization, reminiscent of seizures observed in human TLE patients. Although demarcating seizure onset is often difficult, we observed a transient LFP synchronization with simultaneous ipsilateral eye and ear twitches lasting for $\sim$1 second (Figure 1.2, seizure onset), accompanied by a slow positive DC ramp of $\sim$100 V. Approximately 5 seconds after

seizure onset, the mouse exhibited ipsilateral facial automatisms with contralateral forepaw clonus followed by opisthotonus and bilateral forepaw clonus. The seizure then generalized, producing stereotyped tonic-clonic convulsions with large discharges in the DG hilus for 5-7 seconds (Figure 1.2, generalization). Seizure termination was associated with a silent LFP and motionless behavior (Figure 1.2, termination).

Taken together, our suprahippocampal KA injection model of TLE recapitulates many of the morphological changes previously observed in the intrahippocampal KA injection mouse model and exhibits many characteristics reminiscent of human TLE. Importantly, the seizures seem to originate in the DG, as opposed to other systemic chemoconvulsant models where the DG merely follows distant brain regions (Sloviter and Bumanglag, 2013; Queiroz et al., 2009). Moreover, this spontaneous seizure exhibited strikingly similar DC kinetics to hippocampal seizures induced with local penicillin/alum administration in rhesus monkies (Mayanagi and Walker, 1975) or perforant path-evoked seizures in the rat dentate gyrus (Wadman et al., 1992).

Properties and temporal dynamics of pHFOs: Pathological high-frequency oscillations (pHFOs, 100-600 Hz) have been previously described in the DG of epileptic rats and are thought to represent local network dysfunction in the DG circuit (Engel et al., 2009). Although pHFOs appear prior to the spontaneous seizures, it is unknown if they undergo temporal or spectral progression during the epileptogenic process. We were able to record prominent pHFOs in the ipsilateral DG hilus (Figure 1.3 A-D, black traces), which could be visualized by band-pass filtering the records from 200-600 Hz (Figure 1.3 A-D, red traces) and by their spectral characteristics (Figure 1.3 A-D, wavelet transform). These events were present at 4 days post-SE in 5 of 7 KA-injected mice and pHFOs persisted throughout the two-week recording period (Figure 1.3 A-D). Previous studies have investigated pHFO properties in high-pass filtered recording conditions (Bragin et al., 2007; Staba et al., 2004). Here, we recorded LFPs in the DC mode and observed that pHFOs consistently ride on top of large LFP deflections (133±40 V, Figure 1.3 A-D, black traces). However, the amplitude of LFP

deflections did not change throughout the epileptogenic period (p = 0.34, one-way ANOVA, Figure 1.3 E). In contrast, the decay time constant of the LFP deflections became more prolonged from 13.6 ms at 4 days post-SE to 206.4 ms at 14 days post-SE (p = 0.01, K-W ANOVA).

We next assessed the temporal properties of pHFOs generated in the DG. Records from all animals across all four time points revealed that pHFOs are generated in bursts (Figure 1.4A). To assess the bursts we utilized quantification techniques (see methods) originally developed for single ion channel analysis (Colquhoun, 1994; Lieberman and Mody, 1999). We found that the pHFO inter-event interval (IEI) histograms exhibited distributions that were always well fit with at least two exponential distributions (Figure 1.4C, red and blue fits). Occasionally, three exponential distributions could be fit to the data although this was not consistent across animals or recording days (Figure 1.4C, black fit). A critical tau (τ_c) was calculated from the two exponential IEI distribution fits and was used to define the cutoff IEI for defining a burst. Therefore, the burstiness of pHFOs was determined using each recordings own IEI distributions. We found that pHFOs occurred in bursts throughout the epileptogeneic period and that the intra-burst and inter-burst intervals were consistent across all time points (intra-burst interval: 0.52±0.2 s, inter-burst interval: 7.63±2.5 s, p >0.05, one-way ANOVA, Figure 1.4 C-E). Finally, we constructed histograms equivalent to burst length from single channel recordings which contained single pHFO durations and multi-event burst durations as defined by the τ_c (Figure 1.4 F). These distributions could be fit by the sum of a Gaussian and exponential distribution (Figure 1.4 F). Single pHFO durations contributed almost exclusively to the narrow peak of each histogram, indicating the pHFO durations follow log-normal distribution (Figure 1.4 F, red fit and graph), and pHFO durations were consistent across time (90±6.5 ms, p >0.05, one-way ANOVA, Figure 1.4 F). The second, right shifted, distribution represents pHFO burst length (with N >1 pHFOs/burst), and could be well fit with an exponential distribution (Figure 1.4 F and G, blue traces). Surprisingly, the pHFO burst duration remained stable over the four recording

periods during epileptogenesis (1.43±0.4 s, p >0.05, one-way ANOVA, Figure 1.4 F blue fit and graph). Taken together, these data demonstrate that DG pHFO are generated in bursts with stereotyped parameters that do not evolve throughout epileptogenesis.

We next investigated whether the number of pHFOs per burst (N pHFOs/burst) evolved throughout the epoleptogenic process. Initial analysis revealed that pHFO bursts contained 3.8±0.34 pHFOs and that the N of pHFOs/burst did not evolve after SE (p >0.05, one-way ANOVA, Figure 1.5 F). As expected from a random process, closer analysis of N pHFOs/burst histograms revealed that N pHFOs/burst followed a negative binomial (Bernoulli) distribution at all time points (Figure 1.5 A-D) with an average binomial probability (p) of 0.617±0.05 (Figure 1.5 A-D). The binomial probability was surprisingly consistent across all animals and time points, indicating no progression of N pHFOs/burst (p >0.05, one-way ANOVA, Figure 1.5 E). Therefore, we find that pHFOs are generated in a random Bernoulli process, with a slightly greater than chance probability ($p = 0.6$) of generating a pHFO within a burst. Given these data, we conclude that pHFOs are generated in bursts as early as 4 days post-SE, their burst properties do not evolve throughout epileptogenesis and that pHFOs are generated following a Bernoulli process with a probability of 0.6.

Spectral dynamics of pHFOs: Hippocampal oscillations are traditionally identified and defined based upon their frequency ranges, the behavioral states in which they occur and the underlying network dynamics that generate them (Buzsáki, 2006). Normal high-frequency oscillations (ripples) are generated in the CA3 and CA1 regions of the hippocampus and reflect synchronous summated IPSCs but are never observed in the DG under normal conditions (Buzsáki et al., 1992; Ylinen et al., 1995a). Consequently, any HFOs observed in the DG have been defined as pathological, but it is unclear if the spectral characteristics of pHFOs evolve during epileptogenesis (Engel et al., 2009).

We found that spectral properties of pHFOs do indeed evolve prior to the onset of TLE. To quantify changes in pHFO properties over time, raw LFP recordings were band-pass filtered from 200-600 Hz and the envelope of the oscillation was calculated using the Hilbert

transform (see methods). The resulting Hilbert magnitude of each pHFO was aligned by its peak, averaged and normalized. The normalized pHFO Hilbert magnitudes were then compared across all four recording days (Figure 1.6 A-D, colored insets). We found that pHFOs showed a progressive increase in duration from 4 to 14 days post-SE (Figure 1.6 E), which corresponded to a significant increase in the area of the Hilbert magnitude ($p = 0.01$, one-way ANOVA, Figure 1.6 F). This increase in pHFO duration was due to a prolonged decay time constant of the pHFO Hilbert magnitude, increasing from 4.5±0.5 to 13.1±2.2 ms from 4 to 14 days post-SE, respectively ($p = 0.01$, K-W ANOVA, Figure 1.6 G). This finding was initially at odds with the lack of obvious changes in pHFO duration with burst analysis methods (Figure 1.4 G). However, pHFO durations reported in (Figure 1.4 G) were determined by calculating the time between the point at which the pHFO-filtered Hilbert magnitude rose above 2.5xS.D and when it dropped back below the same threshold. Consequently, the actual pHFO durations may have been underestimated. Given this observation, we further investigated the spectral properties of pHFOs using continuous wavelet transform analysis. Average Z-scored wavelet transforms revealed that pHFOs at 4 days post-SE have broad frequency components, ranging from 200-800 Hz that terminated abruptly. Interestingly by 11 days post-SE, the spectral dynamics of pHFOs appear to spread out and pHFOs developed a prominent spectral tail with temporally decaying frequency components by 14 days post-SE (Figure 1.6 A vs 1.6 D, arrows). These data demonstrate that pHFOs exhibit an evolution of spectral properties during epileptogenisis, though the underlying network contributions have yet to be elucidated.

Dural EEGs are unreliable for pHFO monitoring: Pathological high frequency oscillations have been previously shown to correlate with the development of TLE in rats (Bragin et al., 2004). Here, we also identified pHFOs as reliable pathological network activity that preceded TLE onset. Since pHFOs are candidate biomarkers of epileptogenesis (Engel et al., 2013; Staba et al., 2004), we wanted to see if DG HFOs could be recorded in conventional dural EEG recordings and potentially used as a less invasive way of monitoring epileptogenesis. We

used simultaneous DG hilus LFP and dural EEG recordings to identify the EEG waveforms that corresponded to pHFOs, but found no reliable EEG characteristic that correlated with hilar pHFOs (Figure 1.7 A-F). The EEG recordings were band-pass filtered in the pHFO range (200-600 Hz) and the probability of detecting an EEG pHFO (pHFO Hilbert magnitude >2.5xS.D., p(EEG pHFO|Hilus pHFO)) given the known time points of hilar pHFOs was calculated (Figure 1.7 F). The probability of detecting a corresponding EEG pHFO given the known time points of hilar pHFOs was very low, with an average probability of 0.14±0.07 (Figure 1.7 F). We also compared the probability of finding a hilus pHFO given a detected (putative) pHFO on the dural EEG and found this method to produce very high false positive rates across all time points with an average false-positive rate of 84±8% (Figure 1.7 G). Consequently, there were no reliable dural EEG correlates of pHFOs recorded in the DG to be applied for the monitoring of epileptogenesis without the need of depth electrode temporal lobe recordings.

Discussion:

In this study, we investigated the temporal and spectral properties of pHFOs in the DG during epileptogenesis in a suprahippocampal KA-induced SE mouse model of TLE. We found that pHFOs are present in the DG as early as 4 days post-SE and persist through the development of TLE. DC LFP recordings reveal that pHFOs ride on large DC deflections with decay time constants that become more prolonged over time. Interestingly, DG pHFOs are generated in bursts and exhibit consistent intra-burst and inter-burst properties throughout the latent period. Moreover, the number of pHFOs generated per burst follow a negative binomial distribution, with a p(pHFO) of 0.6. Despite no temporal changes in pHFO burst properties, we found that the duration of pHFOs, measured by the Hilbert magnitude of the band-passed (200-600 Hz) trace, increases over time due to prolonged pHFO decay time constant. This finding was supported by overt changes in the time-frequency properties of pHFOs using continuous wavelet transform analysis. Finally, despite prominent pHFOs in

the DG with strong burst characteristics, dural EEG recordings could not reliably detect hippocampal-generated pathological network activity.

The observation in this study that pHFOs are generated in bursts is intriguing because it is unclear whether these bursts follow synaptic barrages from the entorhinal cortex (EC) or are internally generated within the DG microcircuit. We observe that pHFOs ride on top of large negative deflections in the hilus of the DG, which may reflect synaptic input from layer II stellate cells; the major excitatory input to the DG from the EC (Steward and Scoville, 1976; Schwartz and Coleman, 1981). Layer II stellate cells have been shown to receive less GABAergic input between 3 and 7 days post-SE and corresponded to an increase in spontaneous field potentials recorded in the DG (Kobayashi and Buckmaster, 2003). Additionally, layer II stellate cells may possess previously unidentified excitatory collaterals in both the control and epileptic EC, which could exacerbate synaptic input into the DG (Kumar et al., 2007). It is possible that the burst patterns of pHFOs observed in this study reflect bursts of synaptic inputs from the EC during epileptogenesis. An alternate hypothesis, however is that pHFOs are initiated by paroxysmal depolarizing shifts (PDSs) in local DG neurons. PDSs have been described in cortical pyramidal cells (PCs) during epilepsy, are thought to reflect short high-frequency bursts, and underlie EEG inter-ictal spikes (McCormick and Contreras, 2001; Staley and Dudek, 2006). These PDSs have not been described in the DG, however. Consequently, future in vivo whole-cell patch clamp recordings will need to be made from DG GCs during pHFOs to distinguish between these two hypotheses (Pernía-Andrade and Jonas, 2014).

In vivo studies in rats have established that pHFOs are strong biomarkers of epileptogenesis and that the latency to developing pHFOs after SE correlates well with the latency to the first seizure (Bragin et al., 2004, 2003). Other studies have demonstrated that pHFOs exhibit spatial stability over time and can exist within regions of normal DG network function, suggesting that pHFOs may be generated by localized proconvulsant microcircuits (Bragin et al., 2002, 2003). Unfortunately, the exact mechanisms of pHFO generation in TLE are

still unclear (Jefferys et al., 2012; Engel and da Silva, 2012; Jacobs et al., 2012; Menendez de la Prida and Trevelyan, 2011; Staba, 2012). Multiunit activity and juxtacellular recordings from DG granule cells in epileptic mice revealed that pHFOs correlate with increases in neuronal firing and that DG granule cells participate in this activity, respectively (Bragin et al., 2011). Thus, pHFOs could reflect synchronous discharges of ensembles of glutamatergic neurons in the DG. This mechanism is in contrast to normal HFO generation (ripples) in CA3 and CA1 regions where ripples are generated by synchronous EPSCs and IPSCs from perisomatic innervating interneurons and only ∼10% of principal cells participate in the HFO (Ylinen et al., 1995b; Csicsvari et al., 2000). In the epileptic CA3 region, it is believed that pHFOs are generated by synchronous discharges of large ensembles of pyramidal neurons and that the high frequency components (200-600 Hz) of the LFP reflect out of phase neuronal ensemble bursts (Ibarz et al., 2010). A more recent in vitro study in the normal, non-epileptic, CA3 demonstrated that reducing extracellular calcium (Ca^{2+}) from 3 to 1 mM disrupts inhibitory drive onto CA3 pyramidal neurons, resulting in a transition from HFO to pHFO generation (Aivar et al., 2014). While the DG and CA3/CA1 microcircuits are not directly comparable, the underlying network mechanics may be generalizable.

The evolution of pHFO duration and spectral dynamics observed in our study may reflect underlying network reorganization during epileptogenesis. Somatostatin and NPY positive GABAergic interneurons and glutamatergic mossy cells are highly sensitive to neurological insult and begin to degenerate as early as a few days post-insult (Margerison and Corsellis, 1966; Sun et al., 2007; Buckmaster and Jongen-Rêlo, 1999; Maglóczky and Freund, 1993; Volz et al., 2011; Jiao and Nadler, 2007; Sloviter, 1987; Santhakumar et al., 2000). This dramatic loss of both excitatory and inhibitory neurons in the DG contributes to changes in DG excitability during the latent period (Sloviter et al., 2006; Noebels et al., 2012). Moreover, DG granule cells transiently exhibit depolarized GABA reversal potentials (+15 mV) that are present as early as 24 hours post-SE and persist until 2 weeks post-SE (Pathak et al., 2007). In the chronically epileptic DG, parvalbumin positive interneurons receive less

excitatory drive, display disrupted synaptic release probabilities and increased transmission failures (Zhang and Buckmaster, 2009). Consequently, early rapid loss of specific subtypes of neurons combined with disrupted GABA reversal potentials in DG GCs and changes in interneuron synaptic properties may be permissive for the generation of pHFOs (i.e. 4 days post-SE). The progression of pHFO duration and time-frequency characteristics observed at 11 and 14 days post-SE in this study may reflect further development of aberrant mossy fiber collaterals that establish new excitatory GC-to-GC connections (mossy fiber sprouting) (Tauck and Nadler, 1985; Sutula et al., 1989). Although the functional consequence of mossy fiber sprouting has been debated (Noebels et al., 2012), it is generally accepted that these new synapses are predominately excitatory and produce recurrent excitation within the DG microcircuit (Patrylo and Dudek, 1998; Wuarin and Dudek, 1996; Dyhrfjeld-Johnsen et al., 2007; Santhakumar et al., 2005; Morgan and Soltesz, 2008). Initial sparse mossy fiber sprouting has been observed at 7 days post-SE in KA-injected rats and was also present at 14 days post-SE in our study (Figure 1.1 C). Therefore, the emergence of mossy fiber sprouting may extend the duration of pHFOs and modify their spectral dynamics. Future studies that accurately correlate mossy fiber reorganization with quantitative changes in pHFOs during epileptogenesis will be required to substantiate this hypothesis.

We have provided further support that the silent period as described by Penfield in 1961 is decidedly unsilent prior to the onset of TLE (Goldberg and Coulter, 2013). Considerable functional and anatomical reorganization occurs, with sub-convulsive pathological activity emerging soon after insult and persisting through the onset of recurrent seizures. Consequently, precipitating neurological insults can initiate degenerative epileptogenic processes that continue until a threshold is crossed, at which point behavioral seizures manifest. Determining the genetic and environmental conditions that permit epileptogenesis, characterizing its essential biological processes, and developing accurate biomarkers to detect and monitor its progression will be critical for establishing future interventional therapies that will silence the epileptogenic cacophony.

Acknowledgements:

This work was supported by the US National Institutes of Health as follows: 5T32NS058280 to R.T.J., and R01NS075429 and the Coelho Endowment to I.M. We would like to thank Dr. Christian Steinhäuser for developing the suprahippocampal kainate mouse model of TLE and for suggesting it to us for our experiments. Confocal laser scanning microscopy was performed at the CNSI Advanced Light Microscopy/Spectroscopy shared resource facility at UCLA, supported with funding from NIH-NCRR shared resources grant (CJX1-443835-WS-29646) and NSF Major Research Instrumentation grant (CHE-0722519). Finally, we thank Laurel Ormiston for her extensive and varied technical support.

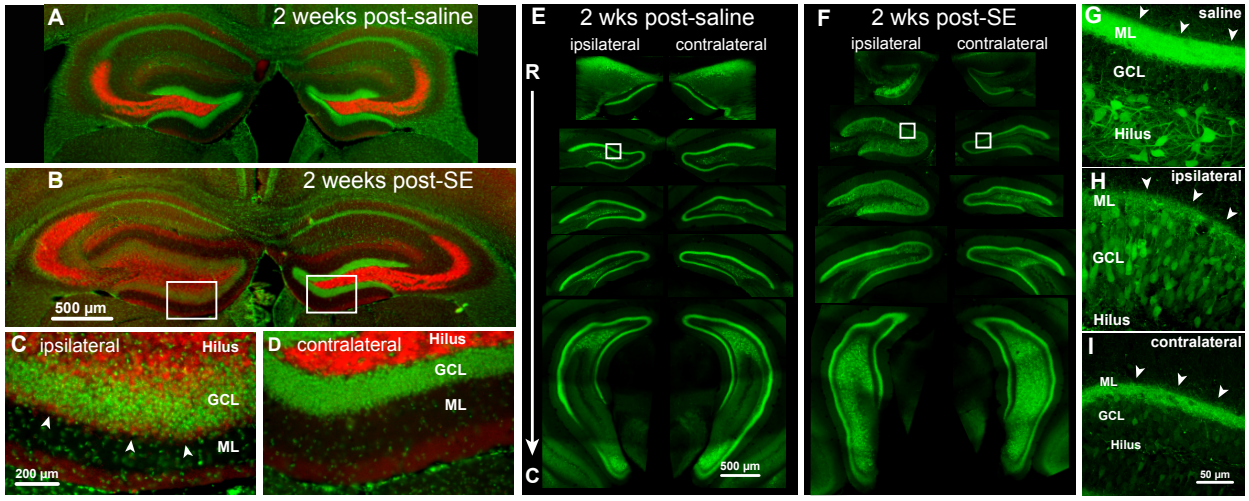

Figure 1.1: Unilateral suprahippocampal KA-injection recapitulates anatomical changes observed in previous models of TLE. **A,** DAPI and immunofluorescent ZnT-3 labeling of cell nulcei (green) and mossy fiber boutons (red), respectively, reveal normal hippocampal anatomy 2 wks post-saline injection. **B,** The same labeling revealed significant cell loss in the CA1 and hilar regions on the KA-injected hippocampus (left), prominent GC dispersion, and light mossy fiber sprouting (**C**, arrows) at 2 wks post-SE. The contralateral, uninjected hippocampus exhibited hilar cell loss but no other overt morphological abnormalities and no detectable mossy fiber sprouting **D**. **E,** Hilar mossy cells and their axonal arborizations within the DG molecular layer are easily visualized along the whole rostro-caudal axis of the hippocampus in a SstR-GFP (Gensat) transgenic mouse. **F,** Mossy cells are lost from both the KA-injected and uninjected dorsal hippocampus at 2 wks post-SE while mossy cells are preserved in the ventral hippocampus. **G,** Mossy cell bodies, dendrites and axonal arborizations are easily visualized in the hilus and inner molecular layer (ML) of the DG in saline-injected controls. In contrast, severe mossy cell loss and reduced axonal labeling was observed in the dorsal hippocampus both ipsilateral **H** and contralateral **I** to KA-injection. Granule cell layer - GCL.

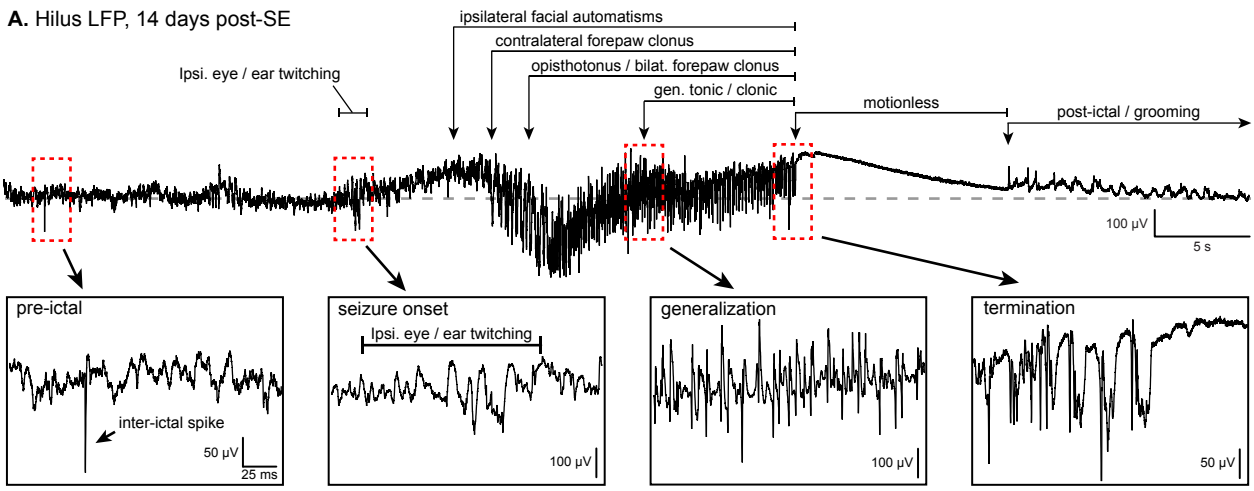

Figure 1.2: Spontaneous seizures in suprahippocampal KA-injected mice are limbic in origin. Simultaneous video and DG hilus LFP recording of a spontaneous seizure 14 days post-SE. Inter-ictal spikes and pHFOs were present preceding seizure onset (red box, pre-ictal). Seizure onset occurred with rapid eye and ear twitching on the ipsilateral (KA-injected) side, with corresponding LFP synchronization and a positive DC shift (red box, seizure onset). The seizure exhibited behavioral characteristics of a complex partial seizure with ipsilateral onset that then generalized to a full tonic-clonic seizure (red box, generalization). Seizure termination (red box, termination) corresponded to behavioral motionlessness followed by post-ictal grooming.

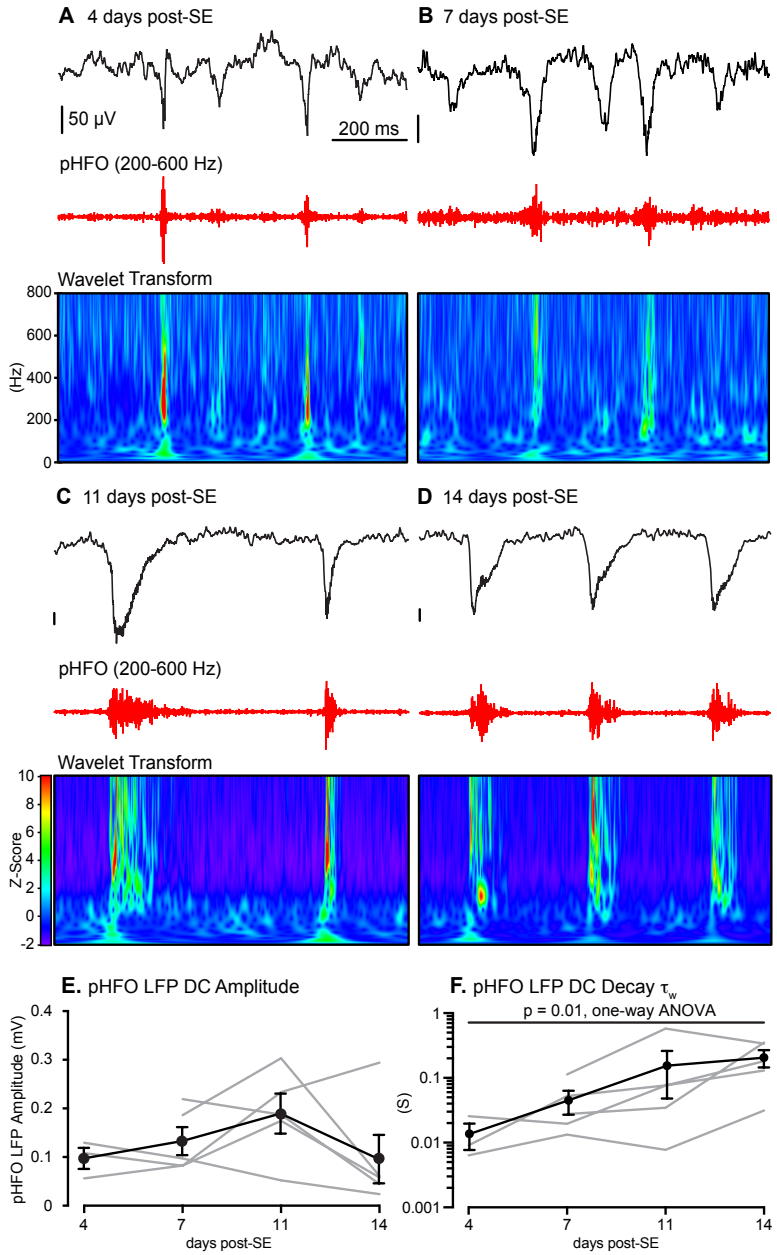

Figure 1.3: General properties of DG pHFOs during epileptogenesis. pHFOs were recorded in all post-SE mice (n = 5) at 4, 7, 11 and 14 days post-SE (n = 3). No pHFOs were detected in saline-injected controls (n = 3). **A-D,** PHFOs were generated on top of large LFP deflections (133±40 μV, black traces). Band-pass filtered records (200-600 Hz) revealed pronounced pHFOs near the peak of the LFP deflection (red traces) and time-frequency analysis with continuous wavelet transform revealed complex spectral properties. **E,** No significant change in LFP deflections was observed across all time points (p >0.05, one-way ANOVA). **F,** In contrast, the decay time constant of the LFP deflection increased significantly from 13.6±0.6 ms at 4 days post-SE to 206.4±6.0 ms at 14 days post-SE (p = 0.01, K-W ANOVA).

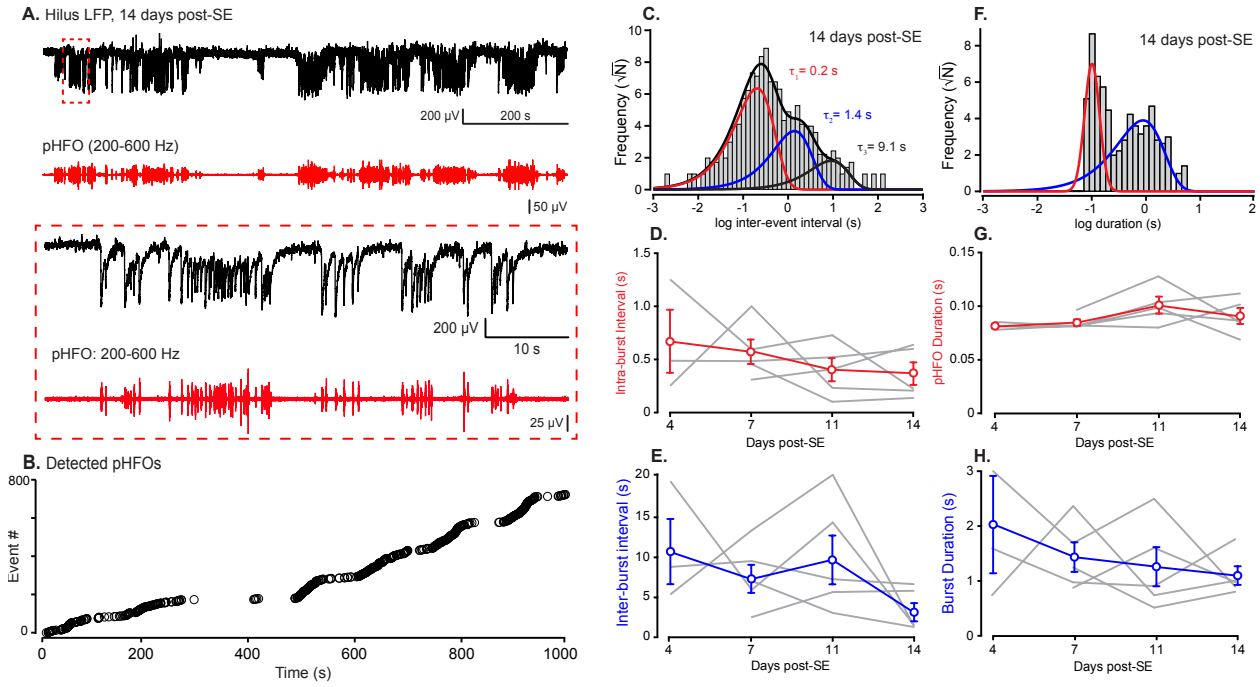

Figure 1.4: Burst properties of DG pHFOs during epileptogenesis. pHFOs occurred in bursts at all time points during the latent period. **A,** Raw DC LFP recordings (top trace) from the DG hilus showed prominent periods of pHFO bursting and regions of relative quiescence. Band-pass filtered records (200-600 Hz, red trace) and close inspection of LFP records (red box) further illustrated the burst character of pHFOs. **B,** Detected pHFO events from the 1000s record in **A** show periods of rapid pHFO generation. **C,** Log-binned pHFO inter-event interval (IEI) histograms exhibited two or three distributions that were well fit with multiple exponential distributions (colored fits) representing intra-burst (red fit), inter-burst (blue fit) and occasionally intra-cluster (black fit) intervals. **D & E,** Intra-burst and inter-burst intervals were 0.52±0.2 and 7.63±2.5 seconds, respectively and showed no significant change from 4 to 14 days post-SE ($p > 0.05$ for each, one-way ANOVA). **F,** Burst duration histograms exhibited two distributions, corresponding to individual pHFO (left distribution, red fit) and multi-pHFO burst (right distribution, blue fit) durations. **G,** Individual pHFO and **H,** multi-pHFO durations were consistent throughout the experimental period, with average durations of 90±6.5 ms and 1.43±0.4 s, respectively ($p > 0.05$ for each, one-way ANOVA).

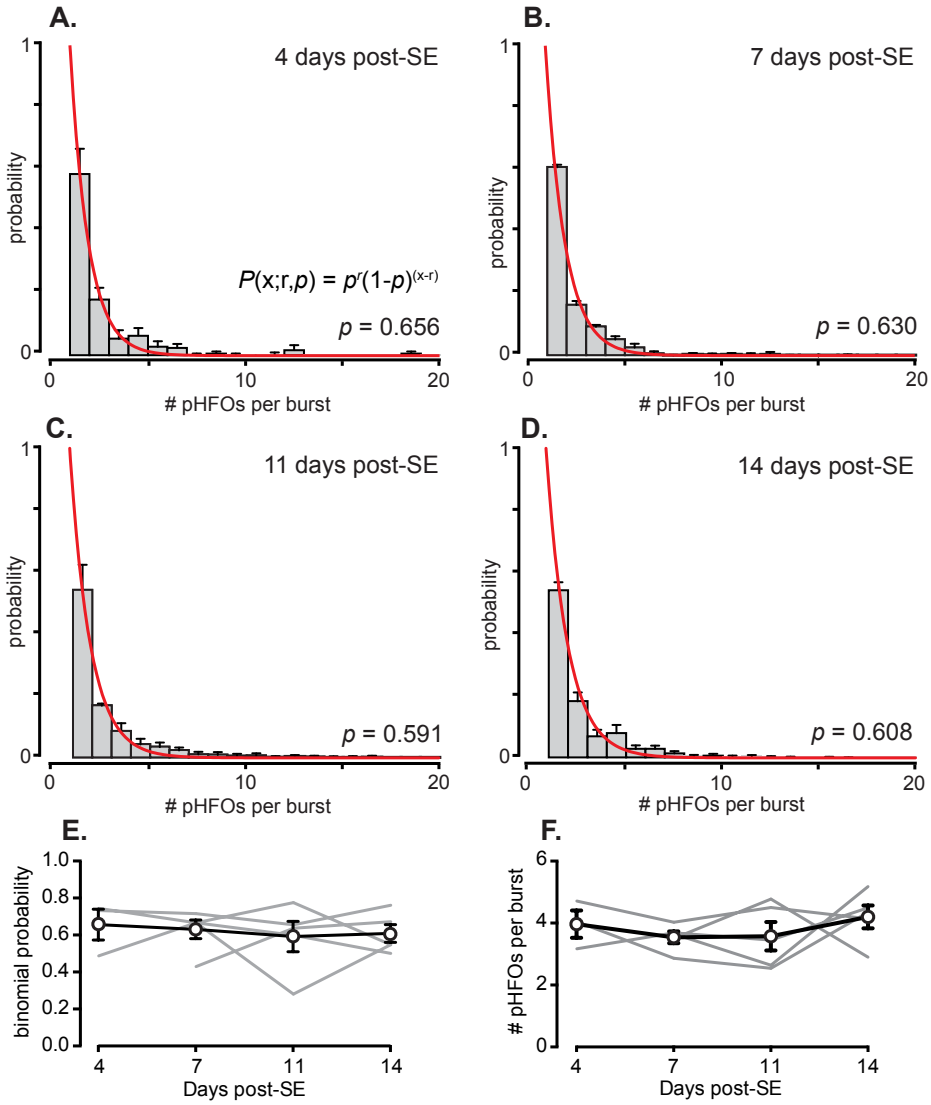

Figure 1.5: The generation of pHFOs follows a Bernoulli process. **A-D,** Histograms of the number of pHFOs per burst (N pHFOs/burst) illustrate that pHFOs are generated randomly and follow a negative binomial (Bernoulli) distribution, indicating that pHFOs are generated indipendantly of each other across all time points. Negative binomial distribution fits revealed that pHFOs are generated with a binomial probability (p) of 0.617±0.05. **E,** The pHFO binomial probability did not change across recording days (p >0.05, one-way ANOVA). **F,** Similarly, the average number of pHFOs per burst did not vary over time (p >0.05, one-way ANOVA).

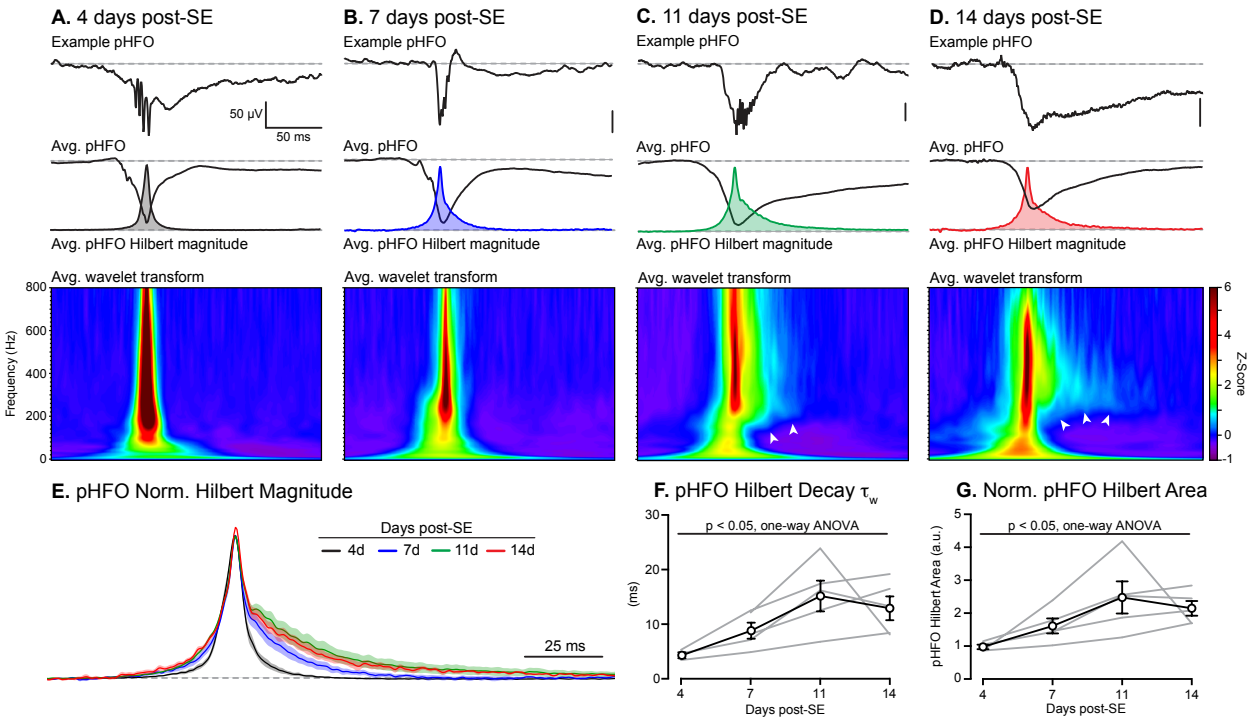

Figure 1.6: Spectral dynamics of pHFOs evolve during epileptogenesis. **A-D,** Example raw, averaged and normalized average Hilbert magnitudes of extracted pHFOs from the same animal at 4, 7, 11 and 14 days post-SE. **E,** pHFOs generated 4 days post-SE (black) exhibited sharp onset and fast delays, with an average weighted decay time constant (τ_w) of 4.4±0.5 ms. The pHFO Hilbert magnitude τ_w increased significantly across recording days (days post-SE: 4, black; 7, blue; 11, green; 14, red) increasing to 13.1±2.2 ms by 14 days post-SE. Traces represent mean±SEM. **F,** The pHFO Hilbert magnitude decay τ_w increased significantly over time (p = 0.01, n = 5, one-way ANOVA). **F,** Similarly, the area of the normalized Hilbert magnitude was significantly increased over the recording period (p = 0.01, n = 5, one-way ANOVA). Avg. Wavelet Transforms reveal complex spectral dynamics of pHFOs from 4 - 14 days post-SE. The average pHFO wavelet transform (aligned to the peak of the pHFO Hilbert magnitude) at 4 days post-SE demonstrated broad frequency components but short temporal lifetime at 4 days post-SE. By 11 and 14 days post-SE, pHFOs became more prolonged and exhibited a spectral tail (arrows) that lasted for up to 100 ms.

CHAPTER 2

Adult-generated granule cells abnormally integrate into the local DG microcircuit during epileptogenesis

Introduction:

The dentate gyrus (DG) is one of two regions of the brain in which neurogenesis continues throughout adult life (van Praag et al., 2002; Eriksson et al., 1998; Aimone et al., 2010a). Newly generated granule cells (NGCs) are constitutively generated from neural stem cells in the sub-granular zone of the DG (Song et al., 2005; Ma et al., 2009), producing approximately 9,000 NGCs each day in the rat hippocampus (Cameron and McKay, 2001). These NGCs develop over a 6-8 week time period, integrate into the local DG microcircuit and extend their axons into the CA3 region where they form functional synapses onto CA3 pyramidal neurons and local interneurons (Espósito et al., 2005; Zhao et al., 2006; Toni et al., 2008). Once fully integrated into the DG, NGCs appear to be indistinguishable from existing granule cells (GCs). During this developmental period, NGCs exhibit a window of enhanced

plasticity between 2 and 4 weeks post-mitosis. This period is characterized by a depolarized resting membrane potential, increased input resistance, depolarized $GABA_A$ reversal potential, lower threshold for LTP induction and greater LTP magnitude (Aimone et al., 2010a; Ge et al., 2007; Schmidt-Hieber et al., 2004). After passing this two-week plasticity window, NGCs exhibit much lower excitability, which appears to persist indefinitely (Aimone et al., 2010b). Previous studies have demonstrated that seizures accelerate both the proliferation and integration of NGCs into the DG microcircuit(Overstreet-Wadiche et al., 2006; Bengzon et al., 1997; Parent et al., 1997) and these NGCs often exhibit morphological abnormalities such as ectopic cell body location, recurrent mossy fiber collaterals and basal dendrites (Kron et al., 2010). Importantly, Kron et al. (2010) demonstrated that the developmental stage of NGCs determines the extent of their abnormal integration after an epilepsy-inducing neurological insult (i.e. status epilepticus, SE). NGCs that were 2-4 weeks post-mitotic at the time of SE had a high probability of exhibiting morphological abnormalities whereas those that were fully mature (>7 weeks post-mitotic) at the time of SE maintained normal morphological characteristics. These morphological abnormalities have been well described previously in GC of the epileptic DG, though it was not clear that developing NGCs exhibited a strong propensity for displaying these changes.

DG GC morphological abnormalities are thought to contribute to changes in DG circuit function during epilepsy. Recurrent abnormal axon collaterals (e.g. mossy fiber sprouting) have been well described in the epileptic dentate gyrus and are believed to form a *de novo* recurrent excitatory circuit within the DG microcircuit (Tauck and Nadler, 1985; Wuarin and Dudek, 1996; Patrylo and Dudek, 1998; Buckmaster and Dudek, 1997, 1999; Coulter et al., 1999). Whole-cell recordings from NGCs in the epileptic DG have revealed similar results, revealing that NGCs also participate in DG functional network reorganization.(Overstreet-Wadiche et al., 2006). In addition to mossy fiber sprouting, hilus-projecting basal dendrites have been identified on GCs in the epileptic DG (Franck et al., 1995; von Campe et al., 1997; Buckmaster and Dudek, 1999) and electron microscopy reconstructions revealed that

basal dendrites receive predominately excitatory synapses (95%) (Thind et al., 2008). Basal dendrites are never found on GCs in both rats and mice normally (Desmond and Levy, 1982). However between 5 and 20% of GCs in the epileptic possess basal dendrites (Walter et al., 2007; Spigelman et al., 1998). Interestingly, 22-47% of GCs in the human and primate DG exhibit basal dendrites normally (Lauer et al., 2003; Seress and Mrzljak, 1987). Given the extensive anatomical understanding of DG microcircuit reorganization during epilepsy, several studies have generated computer models designed to elucidate the fundamental qualities of a pro-convulstant microcircuit (Dyhrfjeld-Johnsen et al., 2007; Morgan and Soltesz, 2008; Santhakumar et al., 2005). These studies have revealed that mossy fiber sprouting and the presence of a small percentage of GCs with basal dendrites play a central role in the pro-convulsant reorganization of the DG.

Given these data, we sought to investigate their functional impact during epileptogenesis in vitro. To accomplish this, we utilized retroviral vectors (RV) to selectively express GFP or ChR2 in NGCs Tashiro et al. (2006) two-weeks prior to an epilepsy inducing insult (e.g. SE). We chose to induce SE two-weeks post-RV since NGCs exhibit enhanced plasticity at this time and because Kron et al. (2010) have previously demonstrated the NGCs displayed the most extensive morphological disruption at this point. SE was then induced 2 weeks post-RV using unilateral suprahippocampal kainate injection (Chapter 1, Methods) and recordings were made from RV-labeled NGCs *in vitro* 2 weeks following SE (Figure 2.1 B and C). The 2 wk post-SE time point was chosen because this time point is at the end of the epileptogenic period and is often the time point during which this mouse model begins exhibiting spontaneous seizures. We investigated the intrinsic excitability, synaptic connectivity and functional output of NGCs after SE using a combination of whole-cell current/voltage clamp and optogenetic approaches.

Materials and Methods:

Animals: Adult (10-12 wks) C57BL/6 were used for all experiments. All mice were housed

on a 12/12 h light/dark cycle and provided with food and water *ad libitum* and all protocols were approved by the University of California, Los Angeles, Chancellors Animal Research Committee (ARC) and comply with National Institutes of Health guidelines.

Retroviral vector production and injection: Retroviral vectors (RV) were produced in-house following previously described methods (Tashiro et al., 2006). Briefly, retroviral constructs were prepared by transient PEI transfection of HEK 293T cells (Clonetech) with a three plasmid system based off of the Moloney Murine Leukemia virus: 1. pCMV-Gag-Pol, 2. pCMV-VSVg (gift from Dr. Fred Gage, Salk Institute) and 3. CAG-EGFP-WPRE. For experiments expressing channelrhodopsin-2 (ChR2) in newborn granule cells, plasmid #3 was replaced with the following: CAG-ChR2(H134R)-EYFP-WPRE (modified from CAG-GFP-WPRE from Dr. Fred Gage, Salk Institute). Virus containing media was collected 48-72 hours post-transfection, sterile filtered, and concentrated using two successive rounds of ultracentrifugation (65,000 g). Virus pellets were re-suspended in phosphate-buffered saline and stored at $-80\,^{\circ}\mathrm{C}$. To express GFP or ChR2 in newly-generated granule cells (NGCs), 1.5 μl of virus was stereotaxically injected bilaterally into the dorsal dentate gyrus using the following coordinates (from the rostral confluence of the sinus, mm): -5.7 rostral/caudal, 1.6 medial/lateral, 1.8 dorsal/ventral from dura (Figure 2.1, Aii).

Suprahippocampal kainate-induced status epilepticus: Two weeks post-RV injection, mice were anesthetized with isoflorane (1.2%, 100% O_2, 1.2 lpm) and 65 nl of 20 mM kainite (KA) or sterile saline (0.9%) was stereotaxically injected above the dorsal hippocampus in the following coordinates (from Bregma): -1.9 rostral/caudal, 1.6 medial/lateral, 0.8 dorsal/ventral from dura (Figure 2.1, Aii). Following KA injection, each mouse was video monitored to observe KA-induced status epilepticus (SE). SE was dampened with lorazepam (6 mg/kg, s.c.) 4 hours post-KA injection and the mice were allowed to recover. Additional saline injections were provided as needed to replenish fluid loss. Mice were housed on a 12/12 h light/dark cycle and provided with food and water *ad libitum*.

Slice preparation: Accute coronal hippocampal brain slices (350 μm) were prepared two

weeks post-KA / saline injections according to protocols approved by the UCLA Chancellors Animal Research Committee (ARC). Mice were deeply anesthetized with isofluorane, and decapitated using a guillotine. The brain was quickly removed and cooled to 4 °C in a sodium-free cutting solution containing (in mM): 135 N-methyl-D-glucamine, 26 HEPES, 10 D-glucose, 4 $MgCl_2$, 1.2 KH_2PO_4, 1 KCl, and 0.5 $CaCl_2$ (bubbled with 100% O_2, pH 7.4, 290-300 mOsm). Slices were cut in the same sodium-free solution using a Leica V1200S vibratome and subsequently transferred to an interface holding chamber containing a reduced sodium artificial cerebrospinal fluid (aCSF) at 32 °C containing (in mM): 85 NaCl, 55 sucrose, 25 D-glucose, 26 $NaHCO_3$, 4 $MgCl_2$, 2.5 KCl, 1.25 NaH_2PO_4, 0.5 $CaCl_2$ (bubbled with 95%/5% O_2/CO_2, 290-300 mOsm). After 30 minutes, the slices were allowed to cool to room temperature ($23 - 25$ °C) and kept in this solution until used for recordings. Brain slices were transferred to a submerged recording chamber at 34 °C and perfused at 5 ml/min with aCSF containing (in mM): 126 NaCl, 26 $NaHCO_3$, 10 D-glucose, 2.5 KCl, 2 $MgCl_2$, 2 $CaCl_2$, 1.25 NaH_2PO_4, 1.5 Na-pyruvate, and 1 L-glutamine (bubbled with 95%/5% O_2/CO_2, 290-300 mOsm). All salts were purchased from Sigma Aldrich (St. Louis, MO).

Recording and Analysis: Patch-clamp recordings were obtained using either a MultiClamp 700A or Axopatch 200B amplifier (Molecular Devices, Sunnyvale, CA) for current or voltage clamp recordings, respectively. Analog signals were low-pass filtered at 5 kHz (Bessel, 8-pole) and digitized at 20 kHz with a National Instruments data acquisition board (NI USB-6221). All current clamp recordings were obtained using custom protocols were written in Igor Pro (WaveMetrics, Lake Oswego, OR). Voltage clamp recordings were obtained using Signal Express (National Instruments). All analyses were performed using custom procedures writtin in Igor Pro.

Current clamp recordings: To assess the intrinsic excitability of RV-labeled adult-generated granule cells, 3 mM kynurinic acid and 100 μM picrotoxin (PTX) were added to the aCSF to block ionotropic glutamate and $GABA_A$ receptors, respectively. Slices were visualized under IR-DIC with an epifluorescent upright microscope (Olympus BX-51WI, 20X XLUMPlan

FL N objective) and whole-cell recordings were obtained from GFP^+ granule cells with borosilicate patch pipettes (4-6 MΩ, King Precision Glass, Claremont, CA) filled with an internal solution containing (in mM): 140 K-methanesulphonate (KMet), 5 KCl, 10 HEPES, 2 $MgCl_2$, 3 NaCl, 0.2 EGTA, 2 Na_2ATP and 0.2 NaGTP, pH adjusted to 7.3-7.4 with KOH.

After achieving stable whole-cell configuration in voltage clamp, the amplifier was switched to current clamp mode. Only recordings with series resistances below 20 MΩ were used and bridge balance compensation was applied while in current clamp. After measuring the resting membrane potential, constant current was injected (no more than 50 pA) into the cell to keep its membrane potential between -60 and -65 mV. Current steps (300 ms) from -100 to +300 pA were injected at random every 30 seconds. Curent steps from -25 to +25 pA (5 pA/step) were injected into the cell to measure the membrane resistance (R_m) and capacitance (C_m). The second derivative of the record was also used to determine action potential (AP) threshold.

Voltage clamp recordings: Whole-cell recordings were obtained as described previously (*Current clamp recordings:*). The intracellular solution contained (in mM) 140 Cs-methanesulphonate (CsMet), 5 KCl, 10 HEPES, 2 $MgCl_2$, 3 NaCl, 0.2 EGTA, 2 Na_2ATP and 0.2 NaGTP, pH adjusted to 7.3-7.4 with CsOH. Recording synaptic currents with a CsMet based internal solution allowed measurement of both excitatory postsynapic currents (EPSCs) and inhibitory postsynaptic currents (IPSCs) in the same neuron by setting the command voltage to -70 mV ($GABA_A$ E_{rev}) or +0 mV (AMPA E_{rev}), respectively. In a subset of experiments, Alexa 488 dextran (Invitrogen) was included in the internal solution to better visualize NGC morphology.

Field recordings and optogenetic activation: Prior to beginning each experiment, brain slices were observed under fluorescence to confirm the presence of virally-transduced YFP^+ NGCs. Local field potential (LFP) recordings were obtained from the granule cell layer and hilar region of the DG using borocilicate glass electrodes (4-6 MΩ, King Precision Glass) filled with 150 mM NaCl. Signals were obtained using an Axon 200B (Molecular Devices, Sunnyvale,

CA), low-pass filtered at 5 kHz and digitized at 8192 Hz with a National Instruments data acquisition board (NI USB-6221). Virally-transduced NGCs were optogenetically activated with brief (5 ms) full-field light pulses (470/30 excitation filter) through the epifluorescence light path using a standard mercury arc lamp and shutter.

Statistical Analysis: Statistics were calculated using GraphPad Prism 6 (La Jolla, CA) and statistics procedures in R. Data are presented as mean ± standard error of mean. Significance level (α) was set to 0.05. For ANOVAs with significance levels below 0.05, post-hoc paired tests were performed and corrected for multiple comparisons. Nonparametric statistical analyses were used from datasets deviating from normality.

Results:

NGC intrinsic excitability during epileptogenesis: Whole-cell current-clamp recordings were made *in vitro* from RV-labeled GFP$^+$ NGCs ipsilateral to KA injection to determine if their intrinsic excitability was altered after SE. We found that NGCs exhibited no significant difference in resting membrane potential (RMP, saline control: -58.0±3.5 vs 2wks post-SE: -57.5±1.5 mV, p >0.5, Mann-Whitney, Figure 2.3 A), action potential threshold (AP threshold, saline control: -42.9±1.5 vs 2wks post-SE: -43.9±1.7 mV, p >0.5, Mann-Whitney, Figure 2.3 A), membrane capacitance (C_m, saline control: 21.6±4.5 vs 2wks post-SE: 25.1±2.3 pF, p >0.5, Mann-Whitney, Figure 2.3 B) or membrane resistance (R_m, saline control: 500±45 vs 2wks post-SE: 445±41 MΩ, p >0.5, Mann-Whitney, Figure 2.3 C). Intrinsic excitability was assessed with 300 ms current steps from -100 to 300 pA. GFP$^+$ NGCs exhibited similar input output curves, with NGCs recorded 2 weeks post-SE showing higher firing frequencies at current pulses greater than 200 pA (Figure 2.3 D). Two-way ANOVA revealed a significant treatment effect (p = 0.02), though subsequent post-hoc tests revealed a significant difference in firing frequency at the highest current step of 300 pA. Finally, we assessed whether NGCs post-SE exhibited a different excitability vs input resistance relationships to NGCs from saline-injected controls. NGCs are known to possess very high membrane resistance

(R_m, $\sim$ 1GΩ) until 2 wks of age, at which point the R_m begins to drop and stabilize at arround 300 MΩ by the time they fully mature. Concurrently, NGCs develop the ability to initate APs. Consequently, we evaluated the relationship of R_m vs. intrinsic excitability after SE. Interestingly, regression analysis found no significant difference in the slope or x intercept of R_m vs. excitability in saline and post-SE NGCs (slope: p = -.972, x-intercept: p = 0.66, Figure 2.3 E). Therefore, we concluded that the intrinsic excitability of NGCs is not altered 2 wks post-SE.

Synaptic connectivity of NGCs during epileptogenesis: We next evaluated the synaptic connectivity of NGCs 2 wks post-SE. Because our mouse model of TLE is generated by unilateral suprahippocampal KA injection, we were able to evaluate the synaptic connectivity of NGCs both ipsilateral and contralateral to KA injection at 2 wks post-SE. To do this, we injected retrovirus bilaterally into the DG to label NGCs with GFP two-weeks prior to SE induction. EPSCs and IPSCs were recorded from RV-labeled NGCs in both the ipsilateral and contralateral DG. We found that NGCs ipsilateral to KA injection exhibited significantly larger EPSC amplitudes compared to NGSs from saline-injected controls, with an average EPSC amplitude of 13.8$\pm$1.6 and 7.5$\pm$0.5 pA, respectively (p = 0.004, K-W one-way ANOVA, Figure 2.4 Ai and Aii). In contrast, EPSCs recorded from NGCs in the contralateral DG showed similar EPSC amplitudes (KA contra.: 9.2$\pm$0.6 vs control: 7.5$\pm$0.5 pA, p >0.05, K-W one-way ANOVA, Figure 2.4 Ai and Aii). Interestingly, the EPSC frequencies of NGCs ipsilateral to KA injection were no different from saline controls, while NGCs contralateral to KA injection received a significantly higher frequency of EPSCs (KA ipsi.: 12.8$\pm$3.5 vs control: 7.3$\pm$1.6 Hz, p >0.05; KA contra.: 19.8$\pm$3.7 vs control: 7.3$\pm$1.6 Hz, p = 0.02, K-W one-way ANOVA, Figure 2.4 Bi and Bii).

Next, we measured the IPSC amplitudes in NGCs from both DG 2 wks post-SE or saline and found no significant differences across groups (KA ipsi.: 30.2$\pm$8.1, KA contra.: 38.9$\pm$6.0 vs control: 23.1$\pm$2.9 Hz, p >0.05, K-W one-way ANOVA, Figure 2.4 Ci and Cii). Strikingly, the IPSC frequencies ipsilateral to KA injection were not different from control but IPSC

frequencies in the contralateral hippocampus were dramatically higher than saline injected controls (KA ipsi.: 12.1±3.0 vs control: 18.0±4.6 Hz, p >0.05; KA contra.: 40.0±9.2 vs control: 18.0±4.6 Hz, p = 0.01, K-W one-way ANOVA., Figure 2.4 Di and Dii).

Some RV-labeled NGCs exhibited basal dendrites: Previous studies have demonstrated that developing NGCs can exhibit basal dendrites after epilepsy-inducing insults (Kron et al., 2010). Consquently, we assesed the morphology of recorded NGCs by visualizing their expressed GFP under epifluorescence or by filling them with Alexa 488 dye for later confocal imaging. We were able to determine that a subset of recorded NGCs did possess basal dendrites ipsilateral to KA injection 2 wks post-SE. These cells had varried basal dendrite morphology by typically posessed a single process that extended deep into the DG (Figure 2.5 A). Confocal microscopy revealed prominent spines on basal dendrites, similar to previous reports (Thind et al., 2008). We found that some NGCs with basal dendrites exhibited significantly larger EPSCs and IPSCs than other NGCs in which basal dendrites were absent, although these metrics were highly variable (Figure 2.5 C & D). Figure 2.5 showes a NGC with basal dendrites (A), its corresponding E\IPSC cumulative probability distributions (arrows), and example traces of EPSC and IPSCs (D). Recordings from NGCs with basal dendrites were particularly rare, so it is difficult to draw conclusions on their role in the network.

ChR2 activation of NGCs can initiate pHFOs in vitro: Pathological high-frequency oscillations (pHFOs) have been well described in the DG during epileptogenesis and are thought to reflect the pro-convulsant reorganization of the DG network (See Chapter 1, Introduction). Despite some evidence that pHFOs may reflect transient synchronous firing of DG GCs, little is known about the microcircuit dynamics that initiate and generate pHFOs. Previous modeling studies have suggested that small numbers of highly interconnected GCs, posessing reuccrent mossy fiber collaterals and basal dendrites, could facilitate the propigation of abnormal activaty across the DG microcircuit (Morgan and Soltesz, 2008). Consequently, we hypothesized that NGCs may be good candidates as potential "hub cells" that could

initiate and propogate pathological activity. To test this hypothesis, we modified our GFP-expressing retroviral plasmid to express the H134R version of channelrhodopsin-2 with a EYFP fluorescent tag (ChR2-EYFP). We then injected this virus into the DG and followed the same experimental timeline that was used to evaluate the synaptic and intrinsic properties of NGCs during epileptogenesis (Figure 2.1 B). We found that RV-transduced NGCs strongly expressed ChR2 4 wks post-RV injection and 2 wks post-SE. Brief, 5 ms, pulses of blue light (488 nm) elicited 3-4 action potentials when measured in cell attached configuration (Figure 2.6 Ai). Whole-cell voltage clamp recordings from the same cell revealed large 400-600 pA photocurrents elicited by the same light pulse duration. APs could be reliably and repeatably elicited as revealed by 10Hz light stimulation in cell attached and whole-cell configurestions in FIgure 2.6 Bi and Bii.

Local field potential recordings were made from multiple points around the granule cell layer, and the same 5 ms light pulse was applied to the brain slice. We found that ChR2 activation of NGCs could produce transient high-frequency oscillations that were reminecent of pHFOs recorded *in vivo* (Engel et al., 2009) (Figure 2.6 Ci). Band-pass filtering between 200 and 600 Hz revealed a prominent high-frequency oscillation, with approximate durations of 60-80 ms. Additionally, wavelet transform analysis confirmed that the preak spectral components of ChR2-induced pHFOs was between 300 and 400 Hz, which is remarkably similar to spontaneously generated pHFOs that have been recorded in epileptic rats and TLE patients (Bragin et al., 2010). In addition to a strong oscillation in the pHFO range, a second oscillation in the high-gamma range (Buzsáki and Wang, 2012) was present at the tail end of the pHFO, with a peak frequency of 80 Hz (Figure 2.6 Cii, arrow). These pHFOs could be continuously elicited by 10Hz stimulation and were accompanied by continuous high-gamma oscillations (Figure 2.6 Di - Diii, arrow). ChR2 activation of NGS was also able to induce pHFOs in the hilar region of the DG (Figure 2.7). These pHFOs exhibited nearly identical spectral properties as those observed in the GCL but were slightly longer at 80-90 ms. Further, no associated high-frequency gamma oscillations were observed. PHFOs could

never be elicited in slices from saline-injected controls.

Discussion:

In this study, we investigated the intrinsic excitability, synaptic connectivity and functional impact of NGCs during epileptogenesis. We found that NGCs recorded in the ipsilateral KA-injected hippocampus appear to maintain normal intrinsic excitability despite extensive network-level reorganization. Synaptic connectivity of NGCs is altered during epileptogenesis, with NGCs ipsilateral to KA injection exhibiting significantly larger EPSC amplitude without a change in IPSC amplitude and E\IPSC frequencies compared to control. In contrast, NGCs recorded contralateral to KA injection exhibited significantly higher IPSC frequencies, with no change in EPSC frequencies or E\IPSC amplitudes. Finally, ChR2 activation of NGCs was sufficient to induce pHFOs *in vitro*. These data are intriguing because they are the first to characterize the properties of developing NGCs during epileptogeneis and provides some insights into how pHFOs may be generated during this process.

We were surprised to find no major changes in intrinsic excitability of NGCs after KA-induced SE. Two recent electrophysiological studies from human TLE tissue and the unilateral hippocampal KA mouse model have demonstrated that DG GCs exhibit significantly reduced intrinsic excitability due to an upregulation of Kir2 channels (Young et al., 2009; Stegen et al., 2009). Consequently, we expected to see prominent differences in NGC excitability during epileptogenesis. In fact, we observe a subtle, yet significant, enhancement of NGC excitability two-weeks post-SE (Figure 2.3 D). Our data may not be in conflict with these earlier findings. Neither study distinguished between developing and fully mature neurons. In fact, (Young et al., 2009) actively excluded GCs whose membrane potentials were >-65 mV, which would exclude a large portion of developing NGCs from their analysis. Secondly, these studies were performed in resected hippocampi from human TLE patients and chronically epileptic mice. Since the data presented here were collected two-weeks post-SE, it is possible that the epileptogenic process had not progressed far enough to induce

homeostatic dampening of GC excitability in response to the epileptic phenotype. To fully address this question, further studies are required to evaluate the excitability of birth-dataed NGCs after the onset of chronic epilepsy.

In contrast to the subtle intrinsic excitability changes observed in NGCs during epileptogenisis, we describe pronounced alterations in synaptic connectivity in both the KA-injected and uninjected hippocampi. Surprisingly, these alterations were contrasting, with NGCs in the ipsilateral DG exhibiting significantly larger EPSCs but otherwise normal synaptic properties and the NGCs in the contralateral DG receiving significantly higher frequencies of IPSCs and EPSCs without any changes in amplitudes (Figure 2.4). The network level reorganization that contributes to these changes in synaptic connectivity is unclear at this time and would require extensive work to elucidate.

Previous reports have assessed the synaptic integration of NGCs after pilocarpine-induced SE using a transgenic mouse line that expresses GFP only in NGCs that are two-weeks of age or younger. These studies have found that immature NGCs show accelerated integration into the DG microcircuit and receive both monosynaptic excitatory input via the medial perforant path and pollysynaptic input, possibly emerging from recurrent excitatory mossy fiber collaterals (Overstreet-Wadiche et al., 2006; Zhao and Overstreet-Wadiche, 2008). Importantly, however, the transgeneic mouse model used in the aforementioned studies only express GFP in NGCs until 2 weeks of age, and may not be directly comparable to the 4 wks post-mitotic NGCs investigated in this study. Given this caveat, it is possible that the enhanced EPSC amplitudes observed ipsilateral to KA-injection in this study reflect the enhanced synaptic integration of NGCs and potential polysynaptic inputs from mossy fiber sprouting. The anatomical data presented in Chapter 1 (Figure 1.1 B and C) indicate that light mossy fiber sprouting can be observed 2 wks post-SE in this model of TLE, which corroborates (Overstreet-Wadiche et al., 2006) and the electrophysiological data in Figure 2.4 (Ai and Aii).

The network level contribution to increased EPSC and IPSC frequencies in NGCs within

the contralateral DG are less clear. Multiple studies using unilateral hippocampal KA injections have found minor gross anatomical abnormalities and a lack of hippocampal sclerosis or mossy fiber sprouting but have identified significant reductions in excitatory mossy cells and subsets of interneurons (Volz et al., 2011; Mitsuya et al., 2009; Marx et al., 2013). Given these observations, one might initially expect a reduction in the frequencies of both EPSCs and IPSCs. However, our data show a significant increase in both, with the increase in IPSC frequencies being most pronounced. These observations could simply reflect the enhanced integration of NGCs into the local microcircuit in response to KA-induced SE and subsequent subconvulsant pathological activity (i.e. pHFOs). An alternate hypothesis is that the loss of a percentage of mossy cells in the contralateral DG (Volz et al., 2011) results in excessive excitatory and inhibitory drive onto DG GCs. This hypothesis, known as the "irritable mossy cell" hypothesis, is attractive and could account for the increase in both excitatory and inhibitory postsynaptic current frequencies without a change in amplitudes (Santhakumar et al., 2000; Dyhrfjeld-Johnsen et al., 2007; Ratzliff et al., 2002).

A final result of this study is the finding that ChR2 activation of NGCs during epileptogenesis is sufficient to initiate pathological high-frequency oscillations. This finding is perhaps most exciting because it provides some insight into the network dynamics that underlie pHFOs. We describe in detail the evolution of spontaneous pHFOs *in vivo* during epileptogenesis in Chapter 1. pHFOs appear to be harbingers of epileptogenesis and likely reflect the accumulation of proconvulsant network abnormalities in the DG. Given the anatomical and modeling studies described in the introduction of this chapter, NGCs with abnormal network integration appeared to be good candidates as initiators of pathological network activity. Indeed, photoactivation of these neruons was sufficient to initiate transient high-frequency oscillations that bear a striking resembalance to the pHFOs observed *in vivo* in Chapter 1 and previous studies in humans and rats (Bragin et al., 1999, 2002, 2003, 2004, 2007). Importantly, the retroviral methods used in this study do not label large percentages of granule cells. Rather, only 15-20 YFP^+ NGCs could be visualized in each hippocampal

slice. As a result, the initiation of pHFOs can only be attributed to the synchronous activation of only a small subset of DG GCs in these experiments, and yet, this activation appears to be sufficient to initiate prolonged high-frequency network oscillations lasting tens of milliseconds. Interestingly, we did not observe large DC offsets during ChR2-induced pHFOs *in vitro*, suggesting a decoupling of the DC offsets and pHFOs in a reduced hippocampal preparation. We believe that these results represent a step towards understanding the mechanism of pHFO generation in the DG and hopefully a deeper understanding of the silent cacophony within the hippocampus during epileptogenesis.

Acknowledgements:

This work was supported by the US National Institutes of Health as follows: 5T32NS058280 to R.T.J., and R01NS075429 and the Coelho Endowment to I.M. We would like to thank Dr. Christian Steinhäuser for developing the suprahippocampal kainate mouse model of TLE and suggesting it to us for our study. Finally, we thank Laurel Ormiston for her extensive and varied technical support.

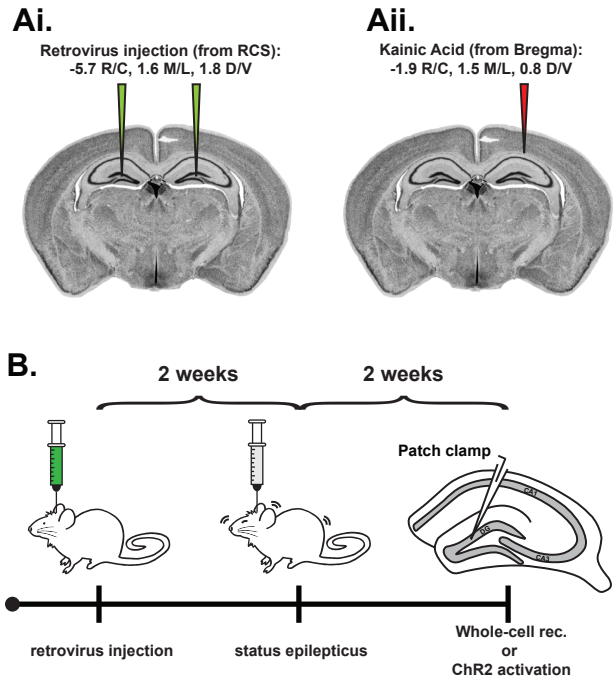

Figure 2.1: Experimental timeline **Ai,** Retrovirus injections were targeted bilaterally to the hilar region of the DG to achieve maximum labeling of NGCs. **Aii,** Two weeks following RV injection, status epilepticus was induced with a unilateral suprahippocampal kainate injection on either the left or right side. NGCs were 2 wks post-mitotic at this time point. **B,** RV-GFP was injectied bilaterally into the DG. Two weeks post-RV, status epilepticus was induced by unilateral suprahippocampal kainic acid injection (Aii). Two weeks following status epilepticus, *in vitro* whole-cell recordings were made from GFP^+ NGCs. For ChR2 experiments, local field potential recordings were made in the DG and ChR2-expressing NGCs were photoactivated with full field illumination at 488 nm. At this time point, NGCs are 4 wks post-mitotic.

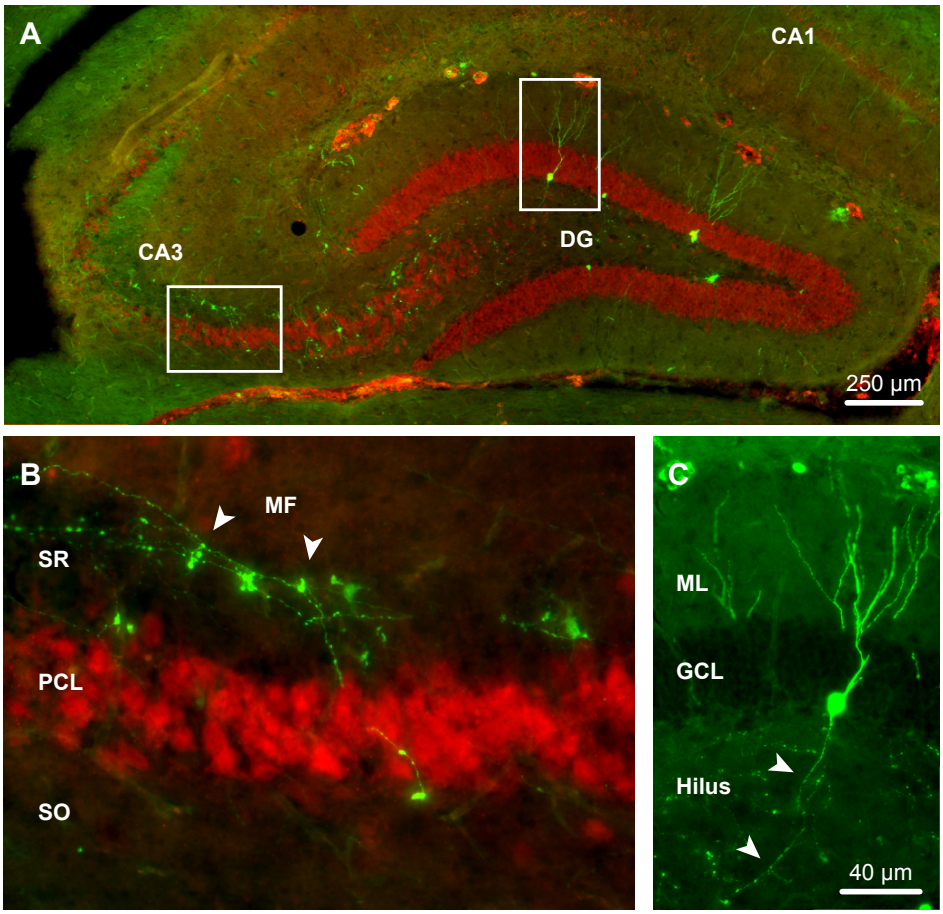

Figure 2.2: Retroviral labeling of adult-generated granule cells in the DG. **A,** GFP$^+$ NGCs (green) visualized in the DG 6 wks post-RV with NeuN immunofluorescence (red). NGC cell bodies were found in the inner GCL and extended their dendrites into the molecular layer of the DG. NGC axons extended into the CA3 region, where they formed putative synapses with CA3 pyramidal cells and local interneurons. **B,** RV-labeled NGCs exhibited typical mossy fiber boutons (MF) in the CA3 stratum radiatum (SR), adjacent to the pyramidal cell layer (PCL). **C,** RV-GFP labeled NGCs showed no overt morphological abnormalities due to RV transduction and had extensive axonal arborizations in the hilus (arrows). ML, molecular layer, GCL, granule cell layer, SR, stratum radiatum, PCL, pyramidal cell layer, SO, stratum oriens.

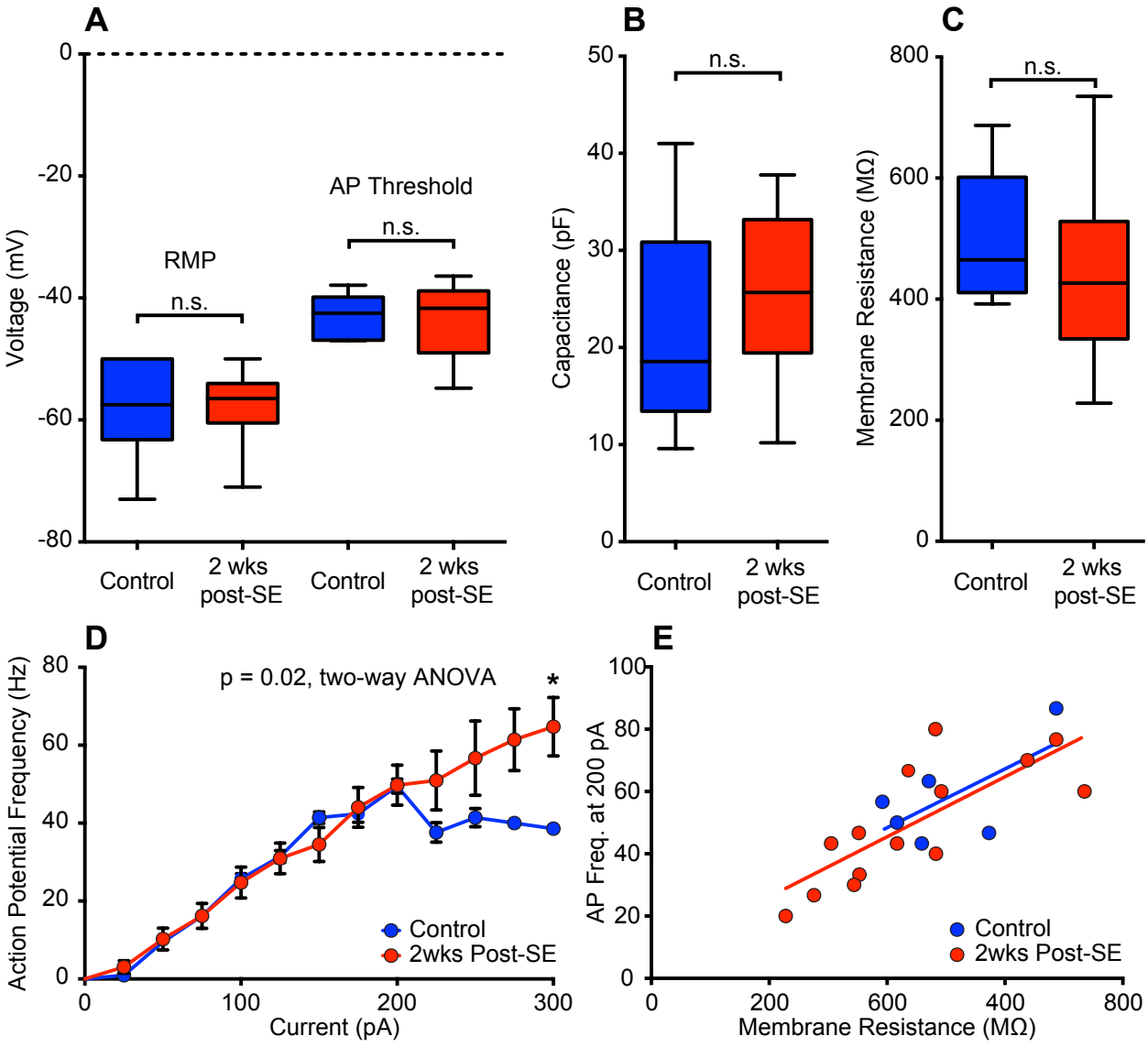

Figure 2.3: Immature granule cells do not exhibit changes in intrinsic excitability 2 wks post-SE **A,** 4 wk old NGCs, recorded 2 wks post-SE or saline, posessed similar resting membrane potentials (saline control: -58.0±3.5 vs 2wks post-SE: - 57.5±1.5 mV, p >0.5, Mann-Whitney) Action potential thresholds were also similar between conditions (saline control: -42.9±1.5 vs 2wks post-SE: -43.9±1.7 mV, p >0.5, Mann-Whitney). **B,** Cell capacitance (Saline control: 21.6±4.5 vs 2wks post-SE: 25.1±2.3 pF, p >0.5, Mann-Whitney) and **C,** membrane resistance were also similar (saline control: 500±45 vs 2wks post-SE: 445±41 MΩ, p >0.5, Mann-Whitney). **D,** Input-output curves were significantly differnt (p = 0.02, two-way ANOVA) although post-hoc tests only found significance at 300 pA current pulses. **E,** Plotting membrane resistance vs action potential frequency at 200 pA current steps revealed no significant differences in the slopes of the two groups (p = 0.9).

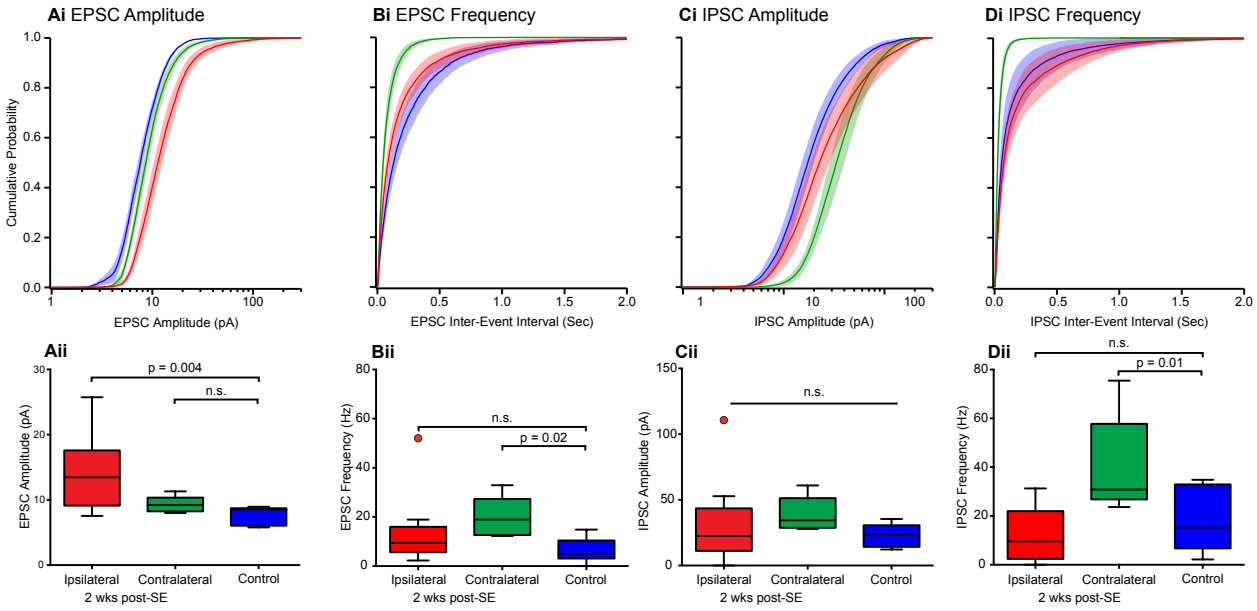

Figure 2.4: NGCs exhibit disrupted functional integration into the DG network 2 wks post-SE. **Ai,** Cumulative probability distributions and **Aii,** mean EPSC values (box plot, Tukey) determined by Hill fit from from individual cumulative distributions of each NGC. EPSCs in NGCs rcorded from the ipsilateral (red), KA-injected, DG were significantly larger than EPSCs recorded from saline-injected controls (blue) (KA ipsi.: 13.8±1.6 vs control: 7.5±0.5 pA, p = 0.004, K-W one-way ANOVA). NGCs recorded from the DG contralateral to KA injection (green) exhibited similar EPSC amplitudes to controls (KA contra.: 9.2±0.6 vs control: 7.5±0.5 pA, p >0.05, K-W one-way ANOVA). **Bi, Bii,** EPSC frequencies in NGCs ipsilateral to KA injection were not different from saline control (KA ipsi.: 12.8±3.5 vs control: 7.3±1.6 Hz, p >0.05, K-W one-way ANOVA) while NGCs recorded from the DG contralateral to KA injection received a higher frequency of EPSCs (KA contra.: 19.8±3.7 vs control: 7.3±1.6 Hz, p = 0.02, K-W one-way ANOVA). **Ci, Cii,** IPSC amplitudes were not significantly different across conditions (KA ipsi.: 30.2±8.1, KA contra.: 38.9±6.0 vs control: 23.1±2.9 Hz, p >0.05, K-W one-way ANOVA). **Di, Dii,** IPSC frequencies were similar between NGCs recorded ipsilateral to KA injection and saline-injected controls (KA ipsi.: 12.1±3.0 vs control: 18.0±4.6 Hz, p >0.05, K-W one-way ANOVA). In contrast, IPSC frequencies were significantly higher in NGCs recorded from DG contralateral to KA injection compared to controls (KA contra.: 40.0±9.2 vs control: 18.0±4.6 Hz, p = 0.01, K-W one-way ANOVA).

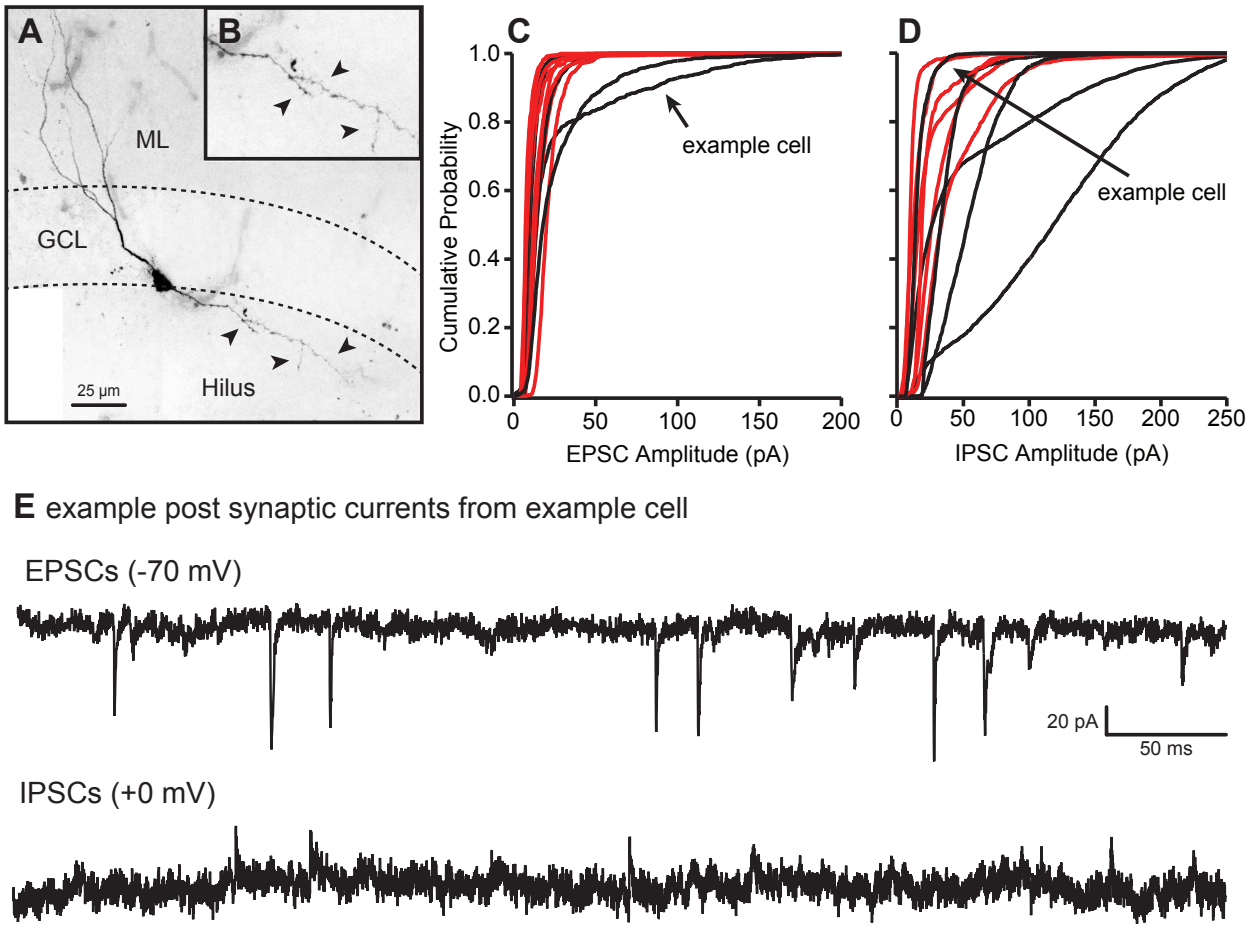

Figure 2.5: Some NGCs exhibit basal dendrites 2 wks post-SE. **A,** An example Alexa 488-filled NGC recorded ipsilateral to KA injection 2 wks post-SE posessed a large basal dendrite taht extended into the hilus (arrows). **B,** Close up image of basal dendrite revealed extensive spines (arrows). Individual NGC EPSC **C** and IPSC **D** amplitude cumulative probability distributions recorded ipsilateral to KA injection. Some NGCs with conformed basal dendrites exhibited dramatically larger EPSC and varried IPSC amplitudes. Arrows indicate EPSC and IPSC cumulative distributions of the representative cell in **A**. **E,** Example EPSC and IPSC recordings from the example cell in **A**.

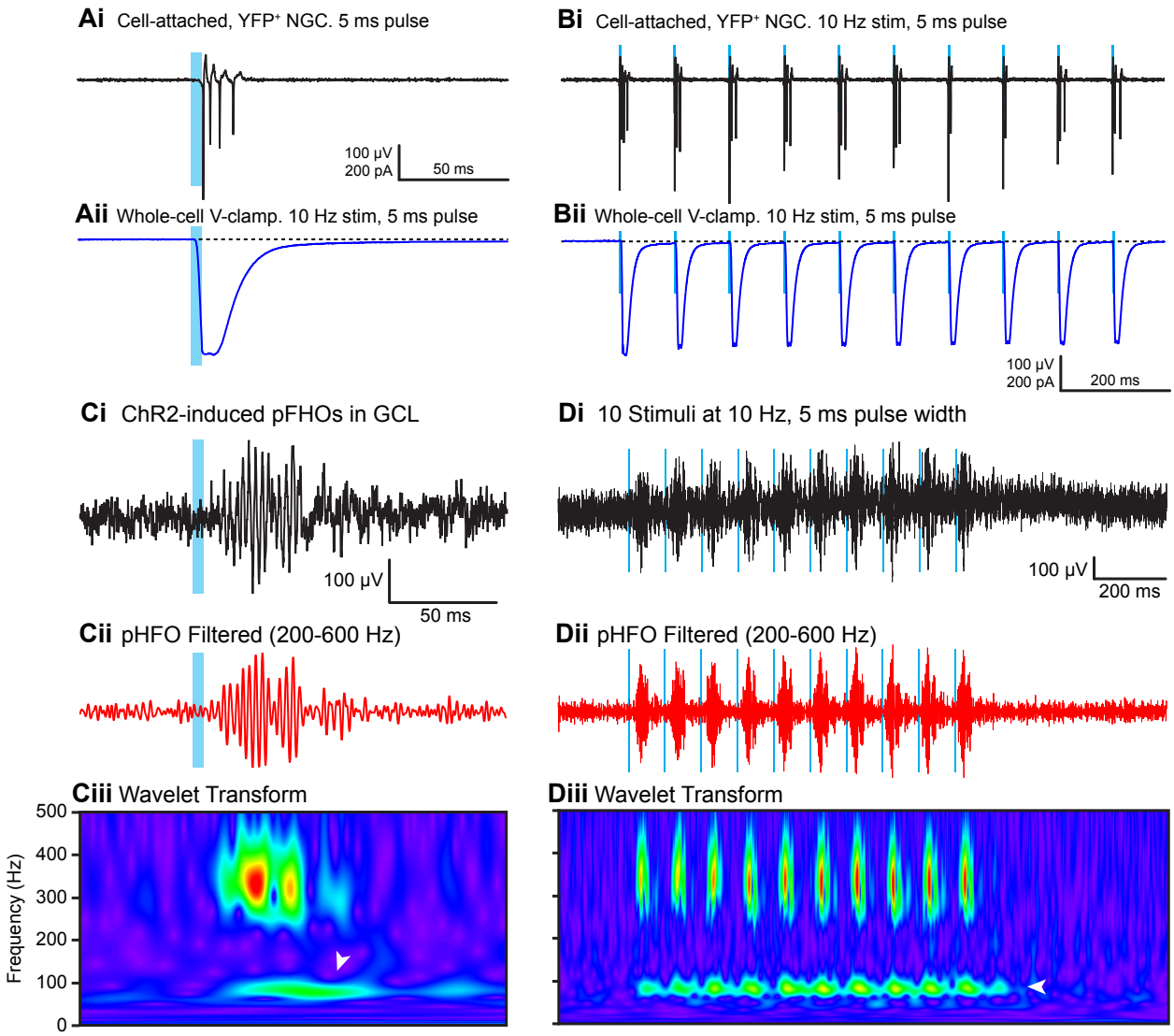

Figure 2.6: **Ai** Cell attached and **Aii** whole-cell voltage-clamp recordings from YFP$^+$ NGC ipsilateral to KA injection at 2 wks post-SE. A 5 ms light flash (488 nm) elicited 2-4 action potentials and large photo currents in cell attached and whole-cell configurations, respectively. **Bi,** 10 Hz light pulses showed that ChR2-expressing NGCs could produce reliable light-induced action potentials in cell attached configuation. **Bii,** ChR2 photocurrents were consistant across light pulses. **Ci,** Local field potential recordings of the DG GCL revealed transient pHFOs following ChR2 activation of NGCs with 5 ms light pulses *in vitro*. **Cii,** pHFO band-pass filtered (200-600 Hz) trace reveals strong high-frequency oscillations, lasting 70 ms. **Ciii,** Continuous wavelet transform of trace in **Ci** revealed the spectral dynamics of the ChR2-induced pHFO. The major frequency components ranged from 300 to 400 Hz. **Di, Dii, Diii** 10 Hz train of light pulses produced consistent pHFO generation in the DG GCL. Prominent high-frequency gamma oscillations were also elicited, with a spectral peak at 80 Hz.

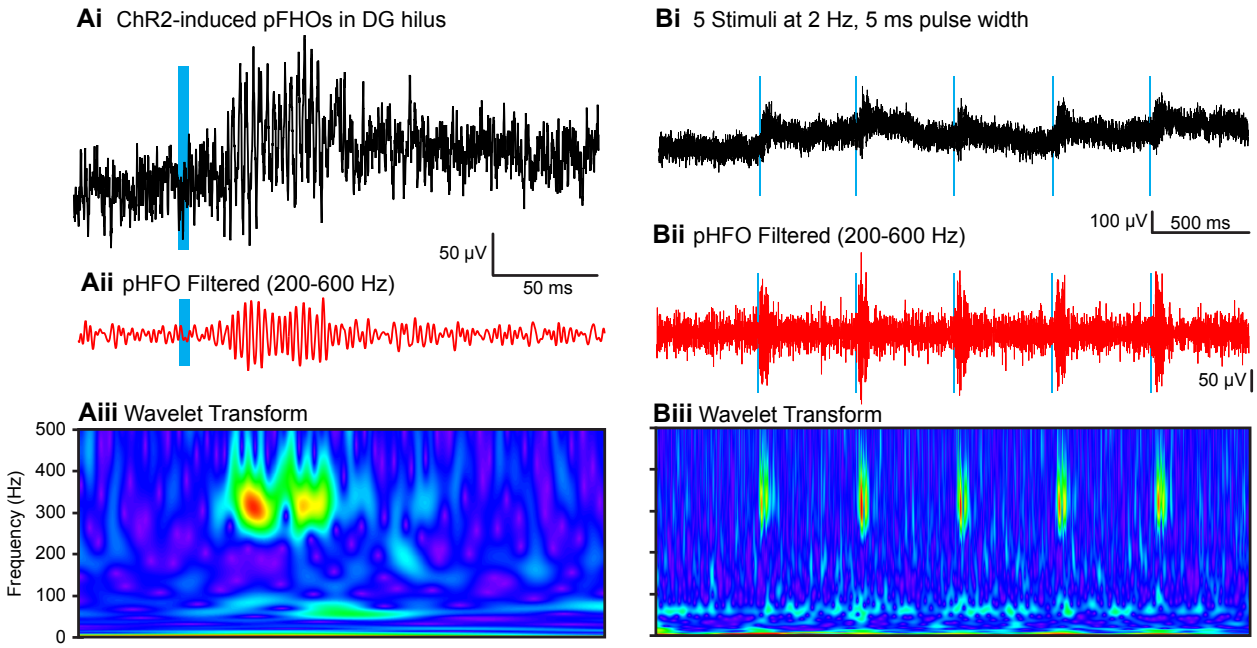

Figure 2.7: ChR2 activation of NGCs 2 wks post-SE initiates pHFOs in the hilus *in vitro*. **Ai,** Local field potential recordings of the DG hilus revealed transient pHFOs following ChR2 activation of NGCs with 5 ms light pulses *in vitro*. **Aii,** pHFO band-pass filtered (200-600 Hz) trace reveals strong high-frequency oscillations, lasting 80 ms. **Aiii,** Continuous wavelet transform of trace in **Ai** revealed the spectral dynamics of the ChR2-induced pHFO. The major frequency components ranged from 300 to 400 Hz. **Bi,** 2 Hz train of light pulses produced consistent pHFO generation in the DG hilus. **Bii, Biii,** Corresponding band-pass (200-600 Hz) and wavelet transforms of the trace in **Bi**. High-frequency gamma oscillations were not observed, however.

CHAPTER 3

Intracellular Bicarbonate Regulates Action Potential Generation via KCNQ Channel Modulation

Intracellular Bicarbonate Regulates Action Potential Generation via KCNQ Channel Modulation

Ryan T. Jones,[1] Guido C. Faas,[2] and Istvan Mody[2,3]

Departments of [1]Neurobiology Graduate Program, [2]Departments of Neurology, and [3]Physiology, The David Geffen School of Medicine, University of California Los Angeles, Los Angeles, California 90095

Bicarbonate (HCO_3^-) is an abundant anion that regulates extracellular and intracellular pH. Here, we use patch-clamp techniques to assess regulation of hippocampal CA3 pyramidal cell excitability by HCO_3^- in acute brain slices from C57BL/6 mice. We found that increasing HCO_3^- levels enhances action potential (AP) generation in both the soma and axon initial segment (AIS) by reducing Kv7/KCNQ channel activity, independent of pH (i.e., at a constant pH of 7.3). Conversely, decreasing intracellular HCO_3^- leads to attenuation of AP firing. We show that HCO_3^- interferes with Kv7/KCNQ channel activation by phosphatidylinositol-4,5-biphosphate. Consequently, we propose that, even in the presence of a local depolarizing Cl^- gradient, HCO_3^- efflux through $GABA_A$ receptors may ensure the inhibitory effect of axoaxonic cells at the AIS due to activation of Kv7/KCNQ channels.

Introduction

Bicarbonate (HCO_3^-) is a key product of cellular respiration, resulting from the hydration of CO_2 and the subsequent deprotonation of carbonic acid. Thus, HCO_3^- is one of the most abundant anions in cerebrospinal and intracellular fluids with a typical concentration of ~26 mM at physiological pH (7.3–7.4) and pCO_2 (5%; Jungas, 2006; Casey et al., 2010). Bicarbonate acts as the major pH buffer in most biological systems (under physiological conditions for CO_2/HCO_3^-, pK_a is ~6.1; Jungas, 2006; Casey et al., 2010). Hence, the steady-state intracellular and extracellular HCO_3^- concentrations ($[HCO_3^-]_i$ and $[HCO_3^-]_o$, respectively) and fluctuations thereof depend on local proton concentration (i.e., pH). For example, in both vertebrate and crayfish neurons HCO_3^- flux through $GABA_A$ receptor channels controls neuronal excitability by changing local pH (Chesler and Kaila, 1992; Jungas, 2006; Casey et al., 2010). Moreover, disturbance in this signaling mechanism might play an important role in some forms of epilepsy, and manipulation of brain pH may be a promising approach to therapeutic intervention (Pavlov et al., 2013). Apart from its well defined role as a pH buffer, HCO_3^- also is a weak Ca^{2+} buffer, with a K_d ~96 mM (Greenwald, 1941; Nakayama, 1971; Jacobson and Langmuir, 1974; Reardon and Langmuir, 1974; Schaer, 1974; Fry and Poolewilson, 1981; Hablitz and Heinemann, 1987). Despite a relatively low affinity for free Ca^{2+}, we initially hypothesized that the relatively high $[HCO_3^-]_i$ may provide physiologically relevant Ca^{2+} buffering, resulting in the modulation of neuronal excitability. To test this hypothesis, we examined the effects of changing $[HCO_3^-]_i$, at a set pH of 7.3, on the firing properties of hippocampal CA3 pyramidal cells (PCs), a cell type that lacks major Ca^{2+} buffering proteins such as parvalbumin, calbindin, and calretinin (Schwaller, 2010). We found that HCO_3^- has a significant effect on neuronal excitability, independent of pH. However, contrary to our initial hypothesis, the effects of HCO_3^- are not due to a direct modulation of Ca^{2+} signaling, but rather to an inhibition of Kv7/KCNQ channel activity. Moreover, fluctuations in $[HCO_3^-]_i$ may control Kv7/KCNQ channel activation through a phosphatidylinositol-4,5-biphosphate (PIP_2)-dependent mechanism.

Received Sept. 8, 2013; revised Feb. 11, 2014; accepted Feb. 18, 2014.

Author contributions: R.T.J., G.C.F., and I.M. designed research; R.T.J. performed research; R.T.J., G.C.F., and I.M. analyzed data; R.T.J., G.C.F., and I.M. wrote the paper.

This work was supported by the US National Institutes of Health Grant 5T32NS058280 to R.T.J., R21AG037151 to G.C.F., and R01NS075429 and the Coelho Endowment to I.M.

The authors declare no competing financial interests.

Correspondence should be addressed to either Dr Istvan Mody or Dr Guido Faas, 635 Charles Young Drive South, NRB1 Rm 575D, Los Angeles, CA 90095, E-mail: mody@ucla.edu or gfaas@ucla.edu.

DOI:10.1523/JNEUROSCI.3836-13.2014

 0270-6474/14/344409-09$15.00/0

Materials and Methods

Electrophysiology. Horizontal hippocampal brain slices (350 μm) were prepared from male C57BL/6J (4–6 weeks) mice according to protocols approved by the UCLA Chancellor's Animal Research Committee. Mice were deeply anesthetized with isofluorane, avoiding all handling and stress to the animals, and were decapitated using a guillotine. Their brains were quickly removed and cooled to 4°C in a sodium-free cutting solution containing the following (in mM): 135 *N*-methyl-D-glucamine, 26 HEPES, 10 D-glucose, 4 $MgCl_2$, 1.2 KH_2PO_4, 1 KCl, and 0.5 $CaCl_2$ (bubbled with 100% O_2, pH 7.4, 290–300 mOsm). Slices were cut in the same sodium-free solution using a Leica V1200S vibratome and subsequently transferred to an interface holding chamber containing a reduced sodium artificial CSF (aCSF) at 32°C containing the following (in mM): 85 NaCl, 55 sucrose, 25 D-glucose, 26 HEPES, 4 $MgCl_2$, 2.5 KCl, 1.25 NaH_2PO_4, 0.5 $CaCl_2$ (bubbled with 100% O_2, pH 7.4, 290–300 mOsm). After 30 min, the slices were allowed to cool to room temperature (22–23°C) and kept in this solution until used for recordings. Brain slices were transferred to a submerged recording chamber at 34°C and perfused at 5 ml/min with aCSF containing the following (in mM): 126 NaCl, 26 HEPES, 10 D-glucose, 2.5 KCl, 2 $MgCl_2$, 2 $CaCl_2$, 1.25 NaH_2PO_4, 1.5 Na-pyruvate, and 1 L-glutamine (100% O_2, pH 7.4, 290–300 mOsm). All salts were purchased from Sigma-Aldrich. DNQX (25 μM), D-AP5 (50 μM) and gabazine or picrotoxin (20 or 100 μM, respectively) were added to block ionotropic glutamatergic and GABAergic transmission (Tocris Biosciences). Slices were visualized under IR-DIC

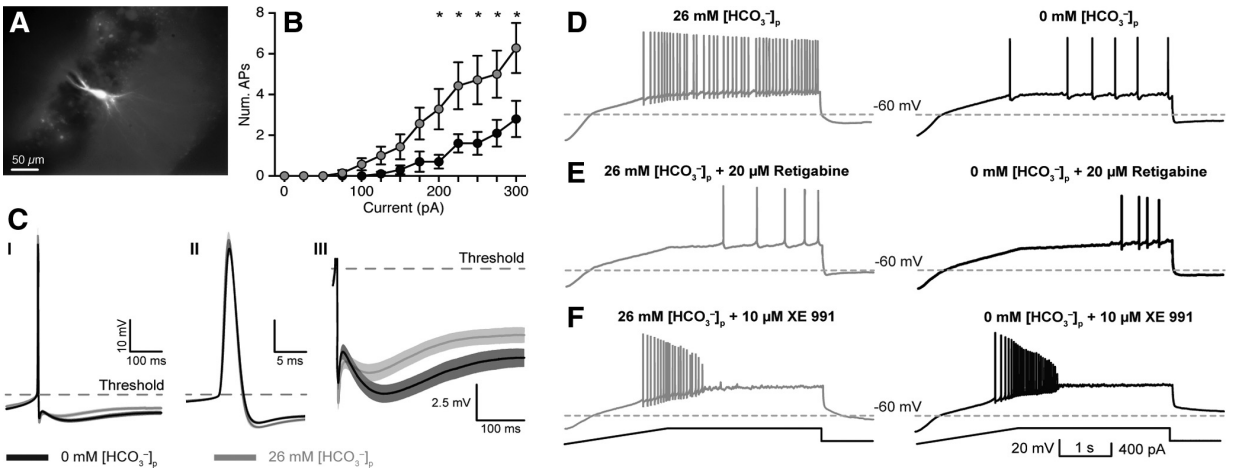

Figure 1. Intracellular HCO_3^- regulates intrinsic excitability via KCNQ channel activation. ***A***, Whole-cell current-clamp recordings were made from CA3 PCs. A subset of recorded neurons was filled with AlexaFluor 488 (50 μM) to confirm CA3 PC morphology. ***B***, Current steps (300 ms) evoked fewer APs with 0 mM $[HCO_3^-]_p$, black traces versus 26 mM $[HCO_3^-]_p$, gray traces ($n = 10$, $p = 0.01$, RM two-way ANOVA; asterisks indicate statistically significant *post hoc* paired tests). ***C***, Spontaneous AP waveforms recorded with 0 or 26 mM $[HCO_3^-]_p$ revealed significantly enhanced mAHP (***CI***, ***CIII***) in 0 mM $[HCO_3^-]_p$, whereas AP amplitude, threshold, and half-width were unaltered (***CII***). ***D***, Current ramp protocols (***F***, bottom) also revealed reduced AP generation in 0 versus 26 mM $[HCO_3^-]_p$, indicating reduced excitability. ***E***, The KCNQ channel activator retigabine (20 μM) reduced the number of APs/ramp in 26 mM $[HCO_3^-]_p$ to levels comparable to 0 mM $[HCO_3^-]_p$. ***F***, In contrast, the KCNQ channel antagonist XE 991 (10 μM) increased the number of APs in both 0 and 26 mM $[HCO_3^-]_p$ and removed the difference between conditions. Data shown as mean ± SEM.

upright microscope (Olympus BX-51WI, 20× XLUMPlan FL N objective) and whole-cell recordings were obtained from CA3 pyramidal neurons with borosilicate patch pipettes (4–6 MΩ, King Precision Glass) containing a mixture (according to the desired $[HCO_3^-]_p$, see below) of two internal solutions: (1) 0 mM HCO_3^- solution (in mM): 135 K-methanesulphonate, 5 KCl, 10 HEPES, 2 $MgCl_2$, 3 NaCl, 0.2 EGTA, 2 Na_2ATP, 0.2 NaGTP, pH 7.3–7.35 with KOH; or (2) 26 mM HCO_3^- solution (in mM): 120 K-methanesulphonate, 15 $KHCO_3$, 5 KCl, 10 HEPES, 2 $MgCl_2$, 3 NaCl, 0.2 EGTA, 2 Na_2ATP, 0.2 Na_2GTP. The pH was set to 7.3–7.35 while bubbling with 5% CO_2/95% O_2. Internal solutions were stored at −80°C in one ml aliquots. Before each experiment, intracellular solution aliquots were thawed to room temperature and the 26 mM HCO_3^- containing intracellular solution (solution 2) was bubbled with 5% CO_2/95% O_2 for 15–20 min. The pH of both solutions was confirmed to be between 7.3 and 7.35 before each day's experiments. The liquid junction potential (LJP) was +5 mV, but reported V_m values have not been adjusted to account for the LJP. The pH drift of the HCO_3^- containing intracellular solution was confirmed to be <0.1 pH/h when sealed in an airtight tube. If the HCO_3^- intracellular solution was exposed to the air, the pH gradually became more alkaline, drifting to pH ~7.6 as CO_2 left solution, but had a very slow time constant of ~4.5 h. The 26 mM HCO_3^- intracellular solution was diluted 1:2 or 1:4 with the 0 mM HCO_3^- solution to produce 13 or 6.5 mM containing pipette solutions, respectively. In a subset of recordings, AlexaFluor 488 dextran (50 μM, Tocris Bioscience) was included in the pipette solution to verify the neuronal morphology of CA3 neurons (Fig. 1*A*). For PIP_2 experiments, PIP_2 (Echelon Biosciences) was dissolved in deionized water at a stock solution concentration of 1 $\mu g/\mu l$ and stored at −20°C. Before each experiment, one aliquot of PIP_2 was thawed and diluted into 0 mM $[HCO_3^-]$ K-Met pipet solution to a final concentration of 10 or 30 μM.

Recording and analysis. Recordings were obtained using a MultiClamp 700A amplifier (Molecular Devices), low-pass filtered at 5 kHz (Bessel, 8-pole) and digitized at 20 kHz with a National Instruments data acquisition board (NI USB-6221). All recording protocols and analyses were performed using custom procedures written in Igor Pro (WaveMetrics).

Current-clamp protocol. After achieving stable whole-cell configuration in voltage-clamp, the amplifier was switched to current-clamp mode. Only recordings with series resistances <20 MΩ were used and bridge balance compensation was applied while in current-clamp. After measuring the resting membrane potential, constant current was injected (no more than ±50 pA) into the cell to keep its membrane potential between −60 and −65 mV. Current steps (300 ms) from −100 to +500 pA were injected every 30 s. To induce steady-state action potential (AP) firing, a steady current was injected through the pipette and was gradually increased until spontaneous action potentials were observed (~−40 to −30 mV). Spontaneous APs were detected and extracted by calculating the second derivative of the membrane voltage deflection and defining AP initiation as the point at which the second derivative deviated significantly from zero. The second derivative was also used to determine AP threshold and was used as the reference point to measure AP amplitude, fast afterhyperpolarization (fAHP; immediately following the AP) amplitude and medium afterhyperpolarization area. The mAHP was defined as the hyperpolarization immediately following the fAHP and lasting ~100 ms (Storm, 1987b, 1989). Statistical analysis of spontaneous AP threshold, amplitude, half-width, fAHP, and mAHP was performed by analyzing 10 consecutive APs and comparing 0 and 26 mM ($[HCO_3^-]_p$ conditions with a two-way repeated-measures (RM) ANOVA. Ramp protocols consisted of a −100 pA step for 1 s, followed by a current ramp to +400 pA (250 pA/s), and then a plateau stage for an additional 3 s. Ramps were applied every 60 s.

Antidromic action current protocols. Whole-cell voltage-clamp recordings were obtained with 0 mM HCO_3^- pipette solution containing AlexaFluor 488 (50 μM) to visualize the axon. A theta glass electrode was positioned near the labeled axon (~250 μm away from soma) and antidromic action currents were evoked with 50–100 μs stimuli. Stimulus trains were applied (5 stimuli, 50 Hz) and the stimulus intensity was adjusted so that the probability of evoking an antidromic action current was ~50%.

Statistical analysis. Statistics were calculated using GraphPad Prism 6 and statistics procedures in *R*. Data are presented as mean ± SEM. Nonparametric statistical analysis was used for datasets that deviated from normality (as determined using a QQ-plot) and the respective statistical tests are indicated in the text and figure legends. The median value (± SE of median) was reported in some cases, because it is a better representation of central tendency for skewed distributions compared with the mean. SE of medians was calculated using resampling procedures in *R*. For ANOVAs with significance levels <0.05, *post hoc* paired tests were performed and corrected for multiple comparisons. Significance level (α) was set to 0.05.

Table 1. Basic membrane properties of CA3 pyramidal neurons

$[HCO_3^-]_o$ (mM)	0	0	0	0		
$[HCO_3^-]_p$ (mM)	0	6.5	13	26	0	*p* value
Resting membrane potential (mV)	−63 ± 1	−57 ± 2	−60 ± 1	−63 ± 2	−66 ± 1	0.208
Input resistance (MΩ)	181 ± 12	185 ± 11	222 ± 30	199 ± 19	202 ± 26	0.638
n	23	5	8	14	5	

Resting membrane potentials and input resistances were not different across all HCO_3^- conditions. Values are mean ± SEM. Statistical comparisons were calculated using one-way ANOVA.

Table 2. Spontaneous AP properties

$[HCO_3^-]_o$ (mM)	0	0	
$[HCO_3^-]_p$ (mM)	0	26	*p* value
Threshold (mV)[a]	−29 ± 0.2	−31 ± 0.1	0.40
AP amplitude (mV)[a]	49 ± 0.6	53 ± 0.4	0.12
Half-width (μs)	784 ± 55	768 ± 39	0.65
fAHP amplitude (mV)[a]	8.8 ± 0.1	10.5 ± 0.1	0.02*
mAHP area (mV · s)[a]	−1.12 ± 0.01	−0.68 ± 0.01	<0.0001*
n	11	11	

Fast AP properties were not significantly affected by $[HCO_3^-]_p$. However, the area of the mAHP was significantly enhanced in 0 mM $[HCO_3^-]_p$. Values are mean ± SEM.

[a]Measured relative to AP threshold. *Indicates statistical significance, two-way RM ANOVA.

Results

Intracellular bicarbonate modulates CA3 pyramidal cell excitability

To assess the influence of $[HCO_3^-]_i$ on neuronal excitability, AP firing properties were measured in CA3 PCs in acute hippocampal slices in HCO_3^--free (0 mM $[HCO_3^-]_o$/HEPES buffered, pH 7.4) aCSF containing 25 μM DNQX, 50 μM D-APV, and either 20 μM gabazine or 100 μM PTX to block AMPA, NMDA, and $GABA_A$ receptors, respectively. Whole-cell recordings were made using pipette solutions containing 0, 6.5, 13, or 26 mM HCO_3^- ($[HCO_3^-]_p$) to set $[HCO_3^-]_i$. Because the conversion of HCO_3^- to CO_2 is catalyzed by multiple carbonic anhydrases and CO_2 readily passes through the membrane (Maren, 1967), it is difficult to set $[HCO_3^-]_i$ to an exact value. However, varying $[HCO_3^-]_p$ will result in correspondingly different values of $[HCO_3^-]_i$. Importantly, to test the effect of $[HCO_3^-]_i$ independent of pH, the pH was carefully set to 7.3 for each pipette solution directly before each experiment. Separate experiments confirmed that pH drift, due to CO_2 dissipation out of the pipette solution, was minimal (<0.1 pH unit) for the typical duration of an experiment.

To measure AP firing, square pulse current steps (300 ms, −100 to +300 pA) were injected into PCs recorded with either 0 or 26 mM $[HCO_3^-]_p$. PCs patched with 26 mM $[HCO_3^-]_p$ exhibited greater intrinsic excitability, measured by the number of APs, than cells recorded with 0 mM $[HCO_3^-]_p$ ($n = 10$ each, $p = 0.013$, R.M. two-way ANOVA; Fig. 1*A*,*B*), whereas resting membrane potentials and input resistances were unaffected (Table 1). Steady firing of spontaneous APs was elicited by gradually depolarizing the cells to −40 to −35 mV with constant current injections. AP properties were assessed at these depolarized potentials. We found that the area of the medium post-spike afterhyperpolarization (mAHP) was significantly larger with 0 mM $[HCO_3^-]_p$ compared with 26 mM $[HCO_3^-]_p$ (1.12 ± 0.1 vs 0.68 ± 0.1 mV*s; $n =$ 11 for both $[HCO_3^-]_p$, $p < 0.0001$; Fig. 1*CI*,*CIII*). However, AP threshold, amplitude, and half-width, were unaffected (Fig. 1*CII*; Table 2). Bicarbonate can act as a weak Ca^{2+} buffer (Greenwald, 1941; Nakayama, 1971; Jacobson and Langmuir, 1974; Reardon and Langmuir, 1974; Schaer, 1974; Fry and Poolewilson, 1981; Hablitz and Heinemann, 1987) and if the effect of HCO_3^- on the mAHP was Ca^{2+}-dependent, adding a strong Ca^{2+}-buffer or reducing Ca^{2+} entry should abolish this effect. However, the mAHP persisted in the presence of 5 mM intracellular BAPTA or

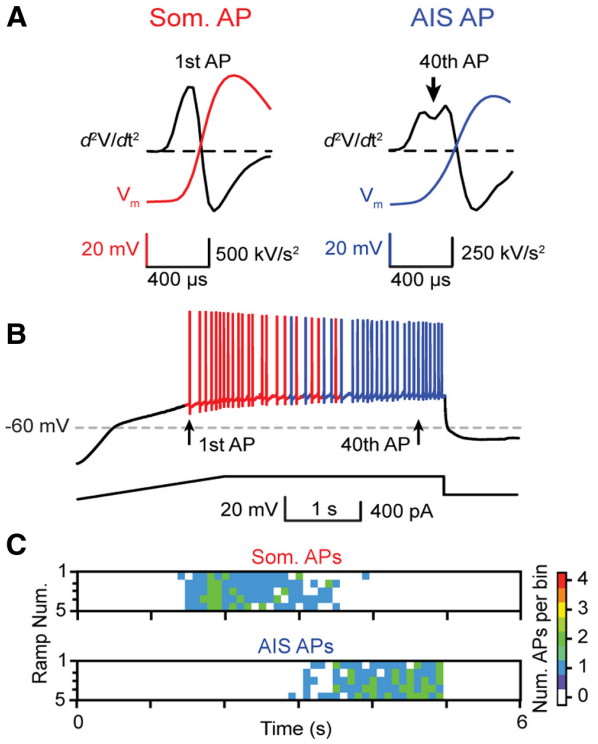

Figure 2. Detection and classification of somatic or axon initial segment generated APs. ***A***, Somatic (Som.; *red*) or AIS (blue) generated APs were determined by calculating the second derivative of each AP. As shown by previous studies (Meeks and Mennerick, 2007), the second derivative of the voltage traces of somatically generated APs exhibit a biphasic waveform during the rising phase, whereas AIS-generated APs exhibit a pronounced biphasic dip (arrow). ***B***, The site of AP generation transitioned from the soma to AIS during current ramps, most likely due to the large somatic voltage change caused by the current ramp injection protocol, and was consistent and reproducible over multiple ramps (***C***). The color scale indicates the number of APs in 100 ms bins.

when 50 μM Cd^{2+} was added to the aCSF (data not shown), confirming earlier observations (Storm, 1987a), and indicating that the reduction of mAHP by HCO_3^- was not due to fast modulation of Ca^{2+} signaling. In summary, these data indicate that intracellular HCO_3^- regulates intrinsic CA3 PC excitability by modulating postspike mAHP, independent of pH and Ca^{2+}.

Intracellular bicarbonate regulates action potential generation by modulating KCNQ channel activation

Previous reports suggest that a major component of the mAHP in CA1 PCs is mediated by Kv7/KCNQ K^+ channels, regulating intrinsic neuronal excitability (Gu et al., 2008; Tzingounis and Nicoll, 2008; Cooper, 2011; Klinger et al., 2011). Because the major effect of lowering $[HCO_3^-]_i$ (0 mM $[HCO_3^-]_p$) was a reduction in intrinsic excitability and an enhancement of the mAHP, we hypothesized that $[HCO_3^-]_i$ may regulate KCNQ channel ac-

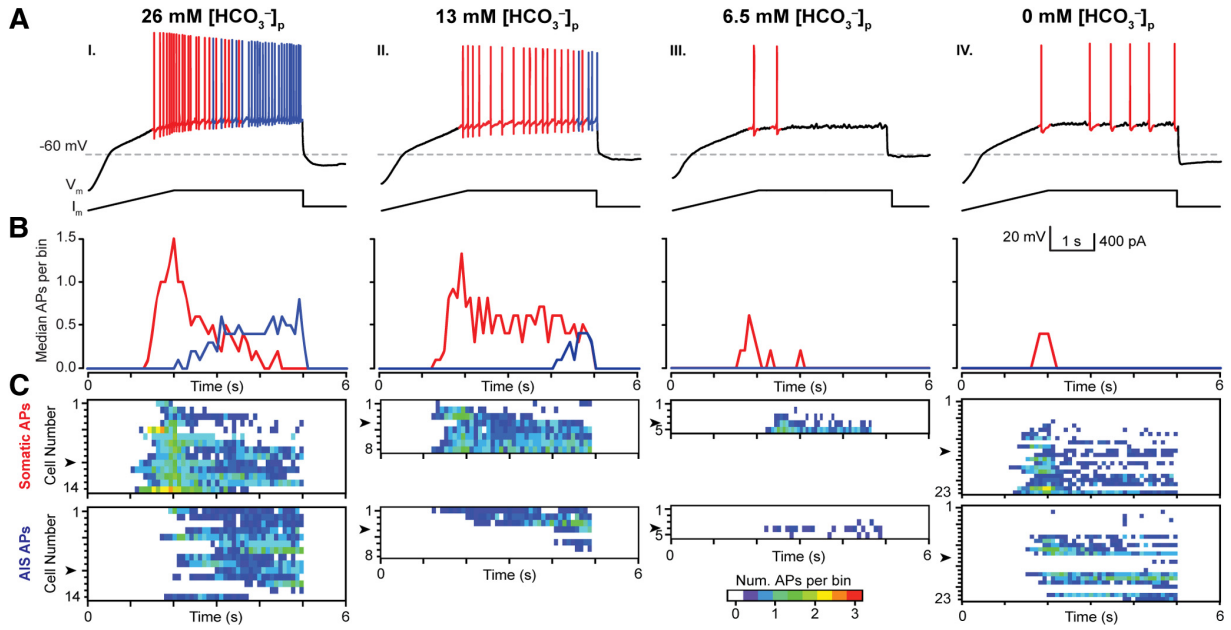

Figure 3. Intracellular HCO_3^- modulates somatic and axon initial segment action potential generation. ***A***, CA3 PCs exhibit a $[HCO_3^-]_p$ dose-dependent reduction in the number of somatic (som, red) and AIS (blue) APs/ramp. ***B***, Median spike time histograms (100 ms/bin) for all cells indicated in ***C*** illustrate the evolution of som to AIS generated APs during the ramp. ***AI–AIV***, Decreasing $[HCO_3^-]_p$ dramatically reduced the median number of som and AIS APs/bin. ***C***, Evolution of AP firing during the ramps is displayed as heat maps in each recorded neuron for different $[HCO_3^-]_p$. Arrowheads indicate the representative neurons shown in ***A***.

tivation. Similar to previous reports in CA1 PCs (Gu et al., 2005), bath-application of the KCNQ selective antagonist XE 991 (10 μM) abolished the mAHP in both 0 and 26 mM $[HCO_3^-]_p$ (data not shown), confirming that KCNQ currents constitute a major component of the mAHP in CA3 PCs.

To establish whether $[HCO_3^-]_i$ can regulate PC excitability by modulating KCNQ channels, we used a current ramp protocol to elicit APs that are sensitive to KCNQ channel activation (Hu et al., 2007). When these ramp protocols were performed in 0 mM $[HCO_3^-]_o$ with either 0 or 26 mM $[HCO_3^-]_p$, we found that PCs recorded with 0 mM $[HCO_3^-]_p$ generated significantly fewer APs/ramp (median = 12 ± 4 APs/ramp, $n = 23$) compared with PCs recorded with 26 mM $[HCO_3^-]_p$ (median = 36 ± 4 APs/ramp, $n = 14$, $p = 0.001$, Mann–Whitney; Fig. 1*D*). Bath application of the KCNQ channel activator retigabine (20 μM) reduced the number of elicited APs/ramp with 26 mM $[HCO_3^-]_p$ (median = 4 ± 3 APs/ramp, $n = 4$) to levels comparable to 0 mM $[HCO_3^-]_p$ plus retigabine (median = 1 ± 1 AP/ramp, $n = 4$, $p = 0.36$, Mann–Whitney; Fig. 1*E*). In contrast, XE 991 (10 μM) dramatically enhanced excitability in both 0 and 26 mM $[HCO_3^-]_p$, resulting in depolarization block, and rendered AP firing comparable between conditions (0 mM: 19 ± 4 APs/ramp, 26 mM: 22 ± 11 APs/ramp, median ± SEM, $n = 4$ each, $p = 0.65$, Mann–Whitney; Fig. 1*F*). Given these data, it is possible that $[HCO_3^-]_i$ regulates PC excitability by modulating KCNQ channel activation such that a decrease in $[HCO_3^-]_i$ increases KCNQ channel activity.

Kv7/KCNQ channels are enriched at the axon initial segment (AIS) of pyramidal cells, where they associate with Na_V channels via the scaffolding protein ankyrin-G and regulate AP initiation (Gu et al., 2005, 2008; Hu et al., 2007; Cooper, 2011). Because the AIS is the predominant site of AP generation in cortical PCs and has lower AP threshold than the soma (Meeks et al., 2005; Meeks

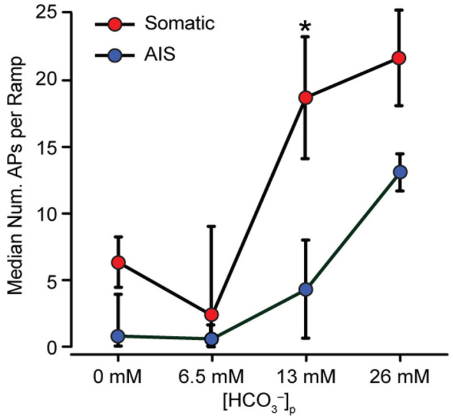

Figure 4. Intracellular HCO_3^- regulates somatic and AIS AP generation. ***A***, Two-way ANOVA shows a significant effect of $[HCO_3^-]_p$ on both somatic and AIS AP generation in 0 mM $[HCO_3^-]_o$ ($F_{(3,92)} = 8.40$, $p < 0.0001$), and an interaction between som. and AIS generated APs ($F_{(3,92)} = 2.76$, $p = 0.046$). AIS generated APs were particularly sensitive to a reduction of $[HCO_3^-]_p$ from 26 to 13 mM. Values given as median ± SE of median.

and Mennerick, 2007; Kole and Stuart, 2012), we investigated whether AP generation is particularly sensitive to $[HCO_3^-]_i$ regulation via KCNQ channels at the AIS. Previous studies have demonstrated APs generated in the soma or AIS exhibit subtle but measurable differences in AP waveforms (Meeks and Mennerick, 2007). To determine the origin of APs generated during current ramp protocols, the second derivative was calculated for each AP and was categorized as being either somatic or AIS in origin based on its distinct waveform (Fig. 2*A*). In our experiments, somatically generated APs preceded AIS generated APs during the ramp protocol and the number of APs/ramp remained

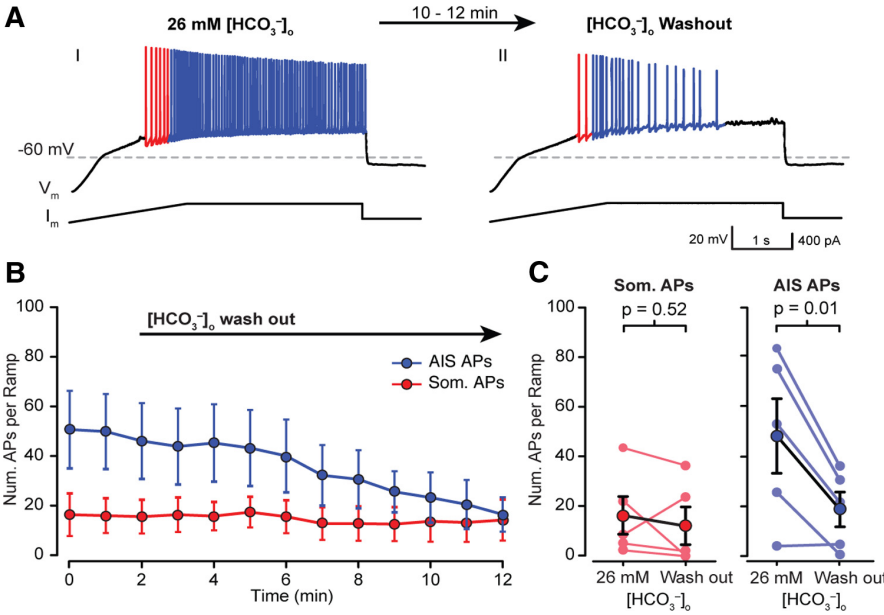

Figure 5. Wash out of extracellular HCO_3^- regulate somatic and AIS AP generation. ***AI***, A sample CA3 PCs exhibited robust AP generation under 0 mM $[HCO_3^-]_p$ and 26 mM $[HCO_3^-]_o$ conditions, likely due to diffusion of extracellular CO_2 through the membrane. ***AII***, Washing out $[HCO_3^-]_o$ with HEPES-buffered aCSF significantly reduced the number of APs generated in response to the same current ramp protocol. ***B***, PCs exhibit robust som and AIS AP generation in 0 mM $[HCO_3^-]_p$ and 26 mM $[HCO_3^-]_o$, (time = 0 min). ***B***, ***C***, AIS APs were significantly reduced after 10 min. of $[HCO_3^-]_o$ wash out (minimum not reached after 10 min), whereas som AP generation remained unchanged (***B***, AIS: $p = 0.02$, som: $p = 0.25$, $n = 5$, two-way ANOVA; ***C***, AIS: $p = 0.52$, som: $p = 0.01$, $n = 5$, paired *t* test).

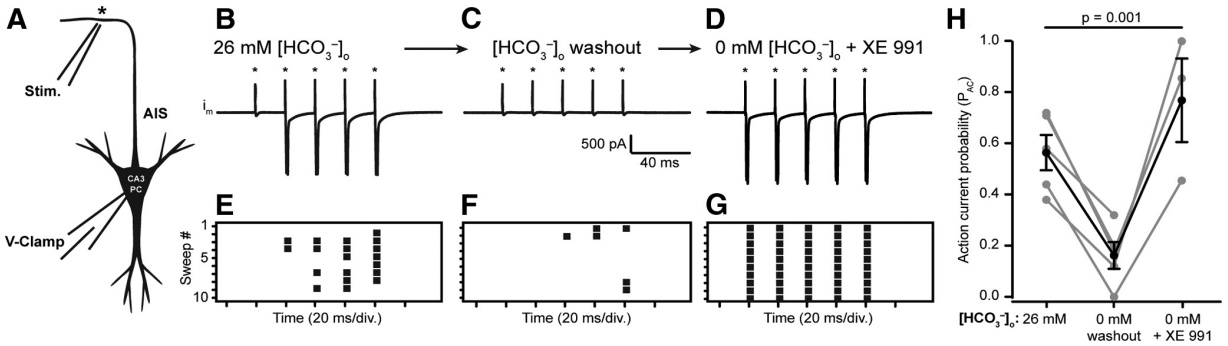

Figure 6. Wash out of extracellular HCO_3^- reduces back-propagation of antidromic APs. ***A***, Antidromic ACs were elicited by local axon stimulation (80 μs pulse width, ~250 μm away from the soma) of visually identified CA3 PCs. ***B***, ***E***, Trains of stimuli (5 stimuli, 50 Hz, asterisks) evoked antidromic ACs recorded with 0 mM $[HCO_3^-]_p$ and 26 mM $[HCO_3^-]_o$ and stimulus intensities were adjusted so that the $p_{AC} \approx 0.5$ over 10 successive stimulus trains (raster plot, ***E***). ***C***, ***F***, Wash out of $[HCO_3^-]_o$ significantly reduced the p_{AC}, illustrated with raster plots of ACs during 10 successive stimulus trains after 10–12 min ($n = 5$, $p = 0.009$, one-way ANOVA, Dunnet's test). ***D***, ***G***, The p_{AC} recovered upon subsequent XE 991 wash in ($n = 3$, $p = 0.143$, one-way ANOVA, Dunnet's test). ***H***, Individual recordings indicated with gray lines, $p = 0.001$, one-way ANOVA. Black lines represent mean $p_{AC} \pm$ SEM.

stable during successive ramps (Fig. 2*B*,*C*). When current ramps were performed with 26, 13, 6.5, and 0 mM $[HCO_3^-]_p$, we found that somatic and AIS AP generation was reduced in a dose-dependent manner in ($p < 0.001$, two-way ANOVA; Fig. 3*A–C*, Fig. 4). Interestingly, decreasing the $[HCO_3^-]_p$ by half (26 to 13 mM) dramatically reduced the median number of AIS APs per ramp (26 mM $[HCO_3^-]_p$: 13 ± 1 AIS APs/ramp vs 13 mM $[HCO_3^-]_p$: 4 ± 4 AIS APs/ramp, median, $p = 0.036$, Mann–Whitney; Fig. 4), whereas somatically generated APs were unaffected (26 mM $[HCO_3^-]_p$: 22 ± 4 somatic APs/ramp vs 13 mM $[HCO_3^-]_p$: 19 ± 5 somatic APs/ramp, median, $p = 0.788$, Mann–Whitney; Fig. 4). These data provide evidence that $[HCO_3^-]_i$ modulates AP generation in both cellular compartments and that AIS-generated APs are particularly sensitive to variations in $[HCO_3^-]_i$.

Extracellular bicarbonate regulates action potential generation by modulating KCNQ channel activation

CO_2 diffuses freely through the lipid bilayer according to the CO_2/HCO_3^- concentration gradient (Maren, 1967). Consequently, it should be possible to (locally) achieve an $[HCO_3^-]_i >$ 0 mM even with 0 mM $[HCO_3^-]_p$ by changing $[HCO_3^-]_o$. This gives us the ability to modulate $[HCO_3^-]_i$ during an experiment simply by changing $[HCO_3^-]_o$. To address this, whole-cell recordings were made from CA3 PCs with 26 mM $[HCO_3^-]_o$, and 0 mM $[HCO_3^-]_p$ and were held for ~10 min before beginning each

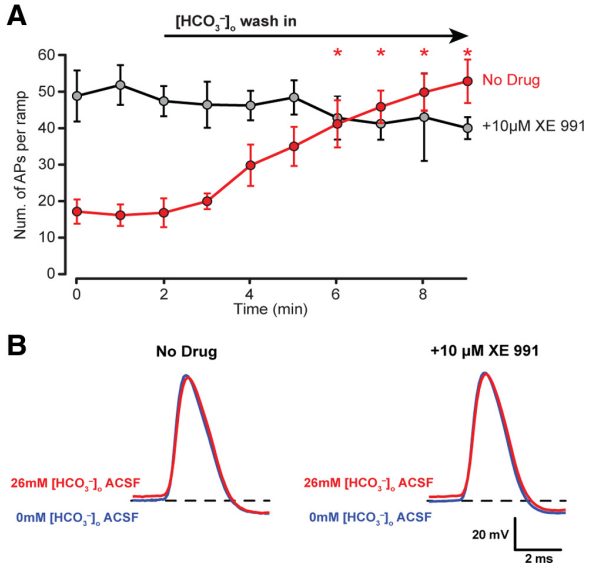

Figure 7. $[HCO_3^-]_o$ wash in increases PC excitability and does not affect the fast components of APs. ***A***, The wash in of 26 mM $[HCO_3^-]_o$ under conditions of 0 mM $[HCO_3^-]_p$ increases AP firing (*red*, No Drug; $p < 0.001$, RM two-way ANOVA), but no such effect is seen when the KCNQ selective antagonist XE 991 is present (gray, +10 μM XE 991; $p = 0.943$, RM two-way ANOVA). ***B***, Wash in of 26 mM $[HCO_3^-]_o$ aCSF does not alter the fast AP components (AP amplitude, half-width, and fAHP amplitude) both in the absence (No Drug) and in the presence of the XE 991 (+10 μM XE 991, $p > 0.05$, RM two-way ANOVA).

Table 3. Fast AP properties

$[HCO_3^-]_o$ (mM)	0	26	0	26
XE 991 (10 μM)	−	−	+	+
Threshold (mV)	−40 ± 2	−38 ± 2*	−43 ± 1	−41 ± 1*
AP amplitude (mV)	75 ± 3	71 ± 3	70 ± 2	67 ± 3
Half-width (μs)	800 ± 33	858 ± 47	866 ± 55	878 ± 68
fAHP amplitude (mV)[a]	7.8 ± 0.5	8.4 ± 0.5	6.3 ± 1.4	6.1 ± 1.5
n	6		5	

AP amplitude, half-width, and fAHP properties were unaffected by wash-in of $[HCO_3^-]_o$ or KCNQ channel block by XE 991 ($p > 0.05$ for HCO_3^- effect, XE 991 effect and interaction, two-way RM ANOVA). AP thresholds were ~2 mV higher in 26 mM $[HCO_3^-]_o$ both with and without XE 991 ($p = 0.04$ for HCO_3^-; effect and $p > 0.05$ for XE 991 effect and interaction, two-way RM ANOVA). Values are mean ± SEM.

[a]fAHP amplitude was measured relative to AP threshold. *Indicates statistical significance, two-way RM ANOVA.

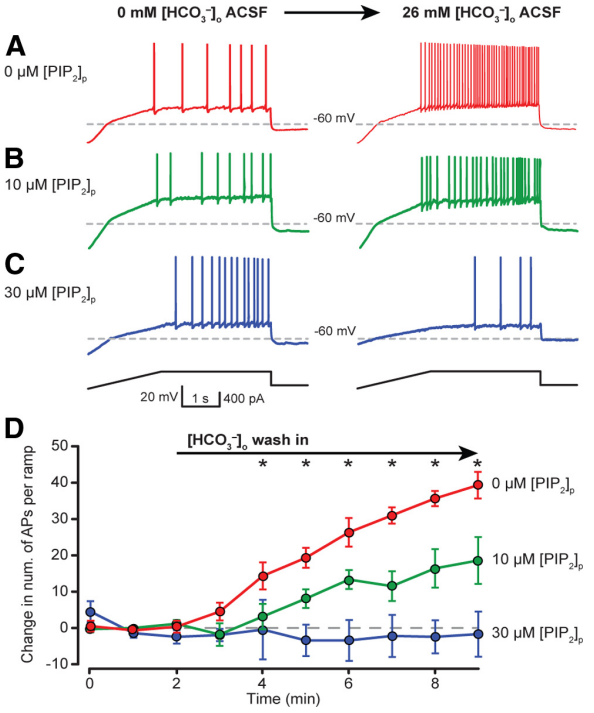

Figure 8. $[HCO_3^-]$ regulates neuronal excitability by modulating intracellular PIP_2 concentration. PCs exhibited dampened excitability in HEPES-buffered (0 mM $[HCO_3^-]_o$) aCSF, and wash in of 26 mM $[HCO_3^-]_o$ significantly increased the number of APs/ramp (***A***, ***D***, red). Increase in PC excitability during 26 mM $[HCO_3^-]_o$ wash in was dampened or absent when 10 μM (***B***, ***D***, green) or 30 μM PIP_2 (***C***, ***D***, blue) was included in the patch solution, respectively. ***D***, Current ramp protocol assessed relative neuronal excitability during transition from 0 to 26 mM $[HCO_3^-]_o$. Recordings made with 0 mM $[HCO_3^-]_p$ pipette solution and 0 μM PIP_2 (red) showed a robust increase in the number of APs/ramp during 26 mM $[HCO_3^-]_o$ wash in. Including 10 (green) or 30 (blue) μM PIP_2 to the patch solution dampened or blocked the increase in neuronal excitability, respectively, upon 26 mM $[HCO_3^-]_o$ wash in (mean ± SEM). *Indicates statistically significant *post hoc* paired tests with correction for multiple comparisons, RM two-way ANOVA.

experiment to dialyze each cell with the pipette solution. Under these conditions, current ramp protocols generated robust APs (median = 60 ± 8 APs/ramp; Fig. 5*A*), with most APs generated at the AIS (blue colored APs). Subsequent $[HCO_3^-]_o$ wash out significantly reduced the number of AIS APs/ramp (26 mM $[HCO_3^-]_o$: 48 ± 15 AIS APs/ramp; 0 mM $[HCO_3^-]_o$: 19 ± 7 AIS APs/ramp, mean ± SEM, $p < 0.001$, R.M. two-way ANOVA; Fig. 5*B*,*C*) while the number of somatically generated APs was unaffected (26 mM $[HCO_3^-]_o$: 16 ± 7 somatic APs/ramp; 0 mM $[HCO_3^-]_o$: 12 ± 7 somatic APs/ramp, mean ± SEM, $p > 0.999$, RM two-way ANOVA; Fig. 5*B*,*C*). No effect of $[HCO_3^-]_o$ was observed when the experiments were repeated in the presence of XE 991 (data not shown).

To further evaluate the effect of reduced $[HCO_3^-]_i$ on AP generation at the AIS, we performed voltage-clamp recordings on CA3 PCs with 0 mM $[HCO_3^-]_p$ and 26 mM $[HCO_3^-]_o$. Recorded neurons were visualized by filling with AlexaFluor 488, and antidromic action currents were generated by local axon stimulation (~250 μm away from the soma; Fig. 6*A*). Stimulation intensity was adjusted to produce ~0.5 probability of antidromic action currents (p_{AC}) in response to stimulus trains (5 stimuli, 50 Hz; Fig. 6*C*). When $[HCO_3^-]_o$ was washed out with HEPES-buffered aCSF, pH 7.4, the p_{AC} was dramatically reduced from 0.56 ± 0.10 in 26 mM $[HCO_3^-]_o$ to 0.16 ± 0.05 in 0 mM $[HCO_3^-]_o$ (mean ± SEM, $p = 0.009$, $n = 5$, one-way ANOVA; Fig. 6*B*,*C*,*E*,*F*,*H*). The p_{AC} recovered to 0.77 ± 0.16 upon subsequent XE 991 (10 μM) application after $[HCO_3^-]_o$ washout ($n = 3$, $p = 0.142$, one-way ANOVA, Fig. 6*D*,*G*,*H*). These data support the hypothesis that reductions in $[HCO_3^-]_i$ can reduce the probability of AP generation at the AIS though a KCNQ channel-dependent mechanism.

Previous studies have demonstrated that changes in $[HCO_3^-]_o$ can alter intracellular pH and alter neuronal excitability (Schwiening and Boron, 1994; Bonnet et al., 1998). In our experiments, the intracellular solution used in our recordings was buffered to pH 7.3–7.35 with 10 mM HEPES. Although 10 mM HEPES is typically used to set the pH of pipette solutions during whole-cell recordings, previous reports have demonstrated that 10 mM HEPES may not provide sufficient buffering capacity during periods of high neuronal activity or in the absence of HCO_3^--dependent intraneuronal buffering (Schwiening and Boron, 1994; Trapp et al., 1996). Therefore, we sought to determine to what extent fluctuations in intraneuronal pH

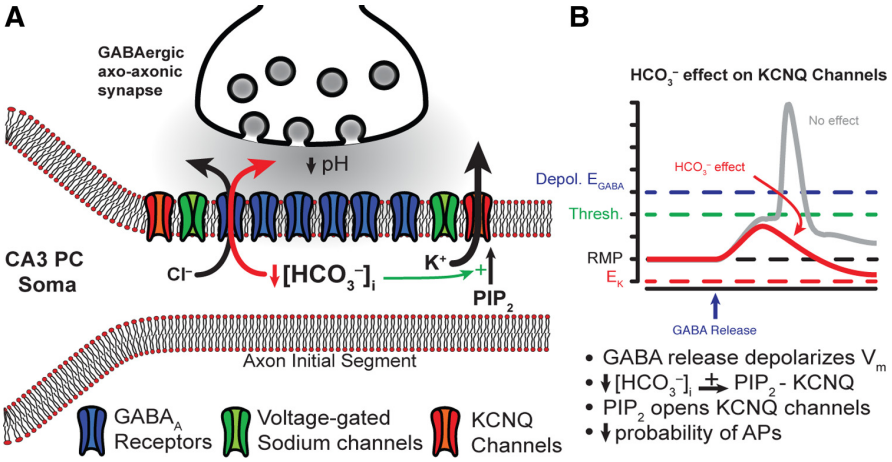

Figure 9. Proposed function of HCO_3^--dependent regulation of KCNQ channels at the AIS. ***A***, Schematic representation of CA3 PC axon initial segment and axo-axonic GABAergic synapse. ***B***, With a depolarized E_{GABA}, activation of synaptic $GABA_A$ receptors ($GABA_A$Rs) during synaptic GABA release would result in membrane depolarization leading to an increased AP firing probability at the AIS (gray trace). However, local depletion of $[HCO_3^-]_i$ through $GABA_A$Rs facilitates PIP_2-KCNQ channel interactions and consequently KCNQ channel activity (green arrow). Enhanced KCNQ channel activation dampens excitability at the AIS and reduces AP probability, thus ensuring an inhibitory effect of axoaxonic cell activation despite a depolarized E_{GABA} (red trace).

may contribute to the excitability of PCs in response to our current ramp protocol. We recorded from CA3 PCs in 0 mM $[HCO_3^-]_o$ using intracellular solutions buffered with 50 mM HEPES and the pH set to either 7.0 or 7.6. Current ramp protocols performed at these halved or doubled $[H^+]$ relative to our controls (pH = 7.3) revealed no significant effect of intraneuronal pH on the number of APs generated per ramp (pH 7.0: 14 ± 3 vs pH 7.6: 14 ± 4 APs/ramp, median, $n = 6$ and 5, respectively, $p > 0.99$, Mann–Whitney). These data demonstrate that pH fluctuations between 7.0 and 7.6 do not significantly affect CA3 PC excitability in our experimental conditions, and therefore the observed changes in excitability are likely to be directly caused by changes in HCO_3^-.

PIP_2 prevents HCO_3^--mediated increase in PC excitability

KCNQ channels are subject to a number of regulatory pathways and can be controlled via Ca^{2+}, diacylgycerol, and Src tyrosine kinase, though primary control runs through the phosphoinositide-phospholipase C cycle via PIP_2 (Delmas and Brown, 2005; Suh and Hille, 2008; Andrade et al., 2012; Telezhkin et al., 2012). Intracellular PIP_2 facilitates KCNQ channel opening in a dose-dependent manner and recent findings demonstrated that PIP_2 is required to couple the voltage sensing domain to pore opening (Zhang et al., 2003; Telezhkin et al., 2012; Zaydman et al., 2013). Consequently, we tested the hypothesis that HCO_3^- regulates KCNQ channel activation through intracellular PIP_2.

We first tested to see whether CA3 PCs would exhibit an increase in excitability when switching from 0 to 26 mM $[HCO_3^-]_o$, analogous to the previous $[HCO_3^-]_o$ wash out experiments. Whole-cell current-clamp recordings from CA3 PCs were performed in 0 mM $[HCO_3^-]_o$ and 0 mM $[HCO_3^-]_p$ and each recording was held for ~10 min before beginning the experiment to allow adequate dialysis of the PC with the pH buffered (7.3) internal solution. Wash in of 26 mM $[HCO_3^-]_o$ aCSF elicited a robust increase in PC excitability from 17 ± 3 APs/ramp to 53 ± 6 APs/ramp after 10 min of wash in (mean ± SEM, $n = 6$, $p < 0.01$, two-way RM ANOVA; Fig. 7*A*, red trace). When $[HCO_3^-]_o$ wash in experiments were repeated in the presence of 10 μM XE 991, PCs exhibited strong AP generation in 0 mM $[HCO_3^-]_o$ aCSF, with an average of 49 ± 7 APs/ramp (Fig. 7*A*, gray trace). Wash in of 26 mM $[HCO_3^-]_o$ aCSF, did not significantly increase CA3 PC excitability (0 mM $[HCO_3^-]_o$: 49 ± 7 APs/ramp to 26 mM $[HCO_3^-]_o$: 40 ± 3 APs/ramp, $n = 5$, $p = 0.943$, two-way RM ANOVA, Fig. 7*A*, gray trace).

To confirm that $[HCO_3^-]_o$ does not affect other conductances underlying AP generation, fast AP waveform properties (i.e., amplitude, half-width, and fAHP) were assessed before and after 26 mM $[HCO_3^-]_o$ wash in and in the presence of XE 991 (Fig. 7*B*; Table 3). No significant effects were observed on AP amplitude, half-width, or fHAP before or after 26 mM $[HCO_3^-]_o$ wash in with or without XE 991, suggesting that no other major conductances underlying AP generation are affected by HCO_3^- other than KCNQ channels ($p > 0.05$ for $[HCO_3^-]_o$ effect, XE 991 effect, and interaction, RM two-way ANOVA; Fig. 7*B*; Table 3). Interestingly, AP threshold was ~2 mV higher in 26 mM $[HCO_3^-]_o$ whether or not XE 991 was present, but the biological significance of this finding is unclear at this time (p values: $[HCO_3^-]_o$ effect = 0.04, XE 991 effect = 0.11, interaction = 0.85, RM two-way ANOVA; Fig. 7*B*; Table 3).

Having established that 26 mM $[HCO_3^-]_o$ wash in could dramatically increase the excitability of CA3 PCs and that this effect was dependent on KCNQ channels, we sought to determine whether the HCO_3^- dependent increase in neuronal excitability could be due to modulation of intracellular PIP_2. Whole-cell current-clamp recordings from CA3 PCs were performed in 0 mM $[HCO_3^-]_o$ and 0 mM $[HCO_3^-]_p$ containing 0, 10 or 30 μM PIP_2 ($[PIP_2]_p$) and current ramps were used to assess PC excitability in 0 mM $[HCO_3^-]_o$ and in 26 mM $[HCO_3^-]_o$. Wash in of 26 mM $[HCO_3^-]_o$ with 0 μM $[PIP_2]_p$ significantly increased the number of APs/ramp (+40 ± 4 APs/ramp, $n = 6$; $p < 0.001$, two-way ANOVA; Fig. 8*A*,*D*). In contrast, including 10 or 30 μM $[PIP_2]$ in the pipet solution dampened or completely occluded the increase in PC excitability during 26 mM $[HCO_3^-]_o$ wash in, respectively (10 μM $[PIP_2]_p$: +19 ± 6 APs/ramp, $n = 6$, 30 μM $[PIP_2]_p$: −2 ± 5 APs/ramp, $n = 4$; $p < 0.001$, two-way ANOVA; Fig. 8*B*–*D*). Therefore, $[HCO_3^-]$ appears to inhibit KCNQ channel activation by interfering with the actions of PIP_2 on the channel, resulting in increased neuronal excitability.

Discussion

Here we describe a novel mechanism whereby $[HCO_3^-]_i$ profoundly modulates the excitability of hippocampal CA3 pyramidal neurons through KCNQ channel regulation. Moreover, HCO_3^- may regulate KCNQ channels by preventing PIP_2 from activating the channels, a fundamental mechanism previously shown to exert a strong control over KCNQ channel opening. Our findings are the first demonstration of a direct regulation of neuronal excitability by $[HCO_3^-]_i$, independent of pH.

Discovering the molecular identity of the HCO_3^- sensor and of the precise pathway leading to interference with the PIP_2-dependent KCNQ channel modulation will require further extensive studies. To date, only two signaling molecules are known to be directly activated by HCO_3^- independently of pH: guanylyl cyclase-D (GC-D; Guo et al., 2009; Luo et al., 2009) and a soluble form of adenylyl cyclase (sAC; Chen et al., 2000; Tresguerres et al., 2010). GC-D has been described to play a role in the olfactory detection of CO_2 in some species and has only been found in olfactory bulb neurons (Fülle et al., 1995; Scott, 2011). Therefore, GC-D is unlikely to play a role in regulating KCNQ channels in our results. Soluble adenylyl cyclase has been shown to directly sense HCO_3^- in a pH-independent manner, resulting in an increase in local cAMP levels and protein kinase A (PKA) activation (Chen et al., 2000). Recent studies have demonstrated strong expression of sAC in astrocytes, where it modulates astrocyte-neuron metabolic coupling, and immunoelectron microscopy has also revealed the presence of sAC in neurons (Choi et al., 2012; Chen et al., 2013). Importantly, the rate-limiting enzyme for PIP_2 generation, PIP5 kinase, is strongly inhibited by phosphorylated PKA (Park et al., 2001; Delmas and Brown, 2005). Thus, sAC may be an attractive candidate as the molecular detector that couples HCO_3^- to KCNQ channel modulation in CA3 PCs. However, activation of PKA has also been shown to have a direct long-lasting potentiating effect on Kv7/KCNQ channels (Wu et al., 2008). Considering these dual and potentially opposing effects of PKA activation on Kv7/KCNQ channels, the identification of PKA as the downstream effector of HCO_3^- will require extensive future studies.

The reduction in KCNQ channel activity by HCO_3^- could be significant in the context of GABAergic innervation of the AIS by chandelier or axoaxonic cells. The excitatory or inhibitory nature of this innervation is highly controversial. Anatomical studies have demonstrated the absence of the Cl^- extruding transporter KCC2 and the presence of the Cl^- importing transporter NKCC1 at the AIS, leading to a depolarizing E_{GABA} (by ~20 mV) relative to somatic and dendritic compartments (Khirug et al., 2008; Woodruff et al., 2009; Báldi et al., 2010) and possibly resulting GABAergic excitation (Fig. 9; Szabadics et al., 2006). Other studies, however, have provided evidence for GABAergic inhibition by AIS-innervating interneurons (Glickfeld et al., 2009). The inhibitory nature of the GABAergic input onto the AIS, regardless of the relationship between E_{GABA} and the membrane potential, may be further supported by our present findings. Synaptic $GABA_A$ receptors are permeable to HCO_3^-, with a permeability ratio of $P^-_{HCO3}/P^-_{Cl} = 0.2$ (Kaila, 1994). At the synapse, $E_{HCO3} \approx -10$ mV due to active intracellular HCO_3^- regulation (Kaila, 1994). Consequently, $GABA_A$ receptor activation at normal resting membrane potential (~−70 mV) results in HCO_3^- efflux through the channel and local decreases in $[HCO_3^-]_i$. However, during heavy synaptic transmission, the outward driving force for HCO_3^- may be even larger than ~60 mV due to acidification of the synaptic cleft. The luminal pH of synaptic vesicles is ~5.5 (Miesenböck et al., 1998), and even single-vesicle release (e.g., miniature IPSCs) has been shown to acidify the synaptic cleft at GABAergic synapses (Dietrich and Morad, 2010). Therefore, periods of heavy GABAergic activity (Dugladze et al., 2012) may cause considerable synaptic cleft acidification at axoaxonic synapses, further decreasing the local $[HCO_3^-]_o$ in the cleft and increasing the HCO_3^- driving force (ΔE_{HCO3} ~60 mV/pH unit). Given the large surface-to-volume ratio of the AIS and its low intracellular volume, the rapid outflow of HCO_3^- could conceivably cause a sharp drop in local $[HCO_3^-]_i$.

Previous reports have demonstrated that HCO_3^- efflux through the GABA receptor promotes the accumulation of intracellular Cl^-, resulting in decreased GABAergic efficacy during periods of high GABAergic activation (Staley et al., 1995; Kaila et al., 1997). Additionally, the activity of neuronal carbonic anhydrases (II and VII) was recently shown to be required for this HCO_3^--dependent intracellular Cl^- accumulation (Ruusuvuori et al., 2013), providing more evidence for a strong interplay between HCO_3^- and GABA receptor efficacy. Given the data presented in this study, it is possible that a large drop in local $[HCO_3^-]_i$ at the AIS during heavy GABAergic activity could facilitate local KCNQ channel activity and greatly reduce AP generation despite the accumulation of intracellular Cl^- and the reduction of GABAergic efficacy (Fig. 9). Although this hypothesis will require further investigation, such a mechanism would ensure that the GABAergic input to the AIS is predominantly inhibitory regardless of E_{GABA}.

References

Andrade R, Foehring RC, Tzingounis AV (2012) The calcium-activated slow AHP: cutting through the Gordian knot. Front Cell Neurosci 6:47. CrossRef Medline

Báldi R, Varga C, Tamás G (2010) Differential distribution of KCC2 along the axo-somato-dendritic axis of hippocampal principal cells. Eur J Neurosci 32:1319–1325. CrossRef Medline

Bonnet U, Wiemann M, Bingmann D (1998) CO2/HCO3 $^-$-withdrawal from the bath medium of hippocampal slices: biphasic effect on intracellular pH and bioelectric activity of CA3-neurons. Brain Res 796:161–170. CrossRef Medline

Casey JR, Grinstein S, Orlowski J (2010) Sensors and regulators of intracellular pH. Nat Rev Mol Cell Biol 11:50–61. CrossRef Medline

Chen J, Martinez J, Milner TA, Buck J, Levin LR (2013) Neuronal expression of soluble adenylyl cyclase in the mammalian brain. Brain Res 1518:1–8. CrossRef Medline

Chen Y, Cann MJ, Litvin TN, Iourgenko V, Sinclair ML, Levin LR, Buck J (2000) Soluble adenylyl cyclase as an evolutionarily conserved bicarbonate sensor. Science 289:625–628. CrossRef Medline

Chesler M, Kaila K (1992) Modulation of pH by neuronal activity. Trends Neurosci 15:396–402. CrossRef Medline

Choi HB, Gordon GR, Zhou N, Tai C, Rungta RL, Martinez J, Milner TA, Ryu JK, McLarnon JG, Tresguerres M, Levin LR, Buck J, MacVicar BA (2012) Metabolic communication between astrocytes and neurons via bicarbonate-responsive soluble adenylyl cyclase. Neuron 75:1094–1104. CrossRef Medline

Cooper EC (2011) Made for "anchorin": Kv7.2/7.3 (KCNQ2/KCNQ3) channels and the modulation of neuronal excitability in vertebrate axons. Semin Cell Dev Biol 22:185–192. CrossRef Medline

Delmas P, Brown DA (2005) Pathways modulating neural KCNQ/M (Kv7) potassium channels. Nat Rev Neurosci 6:850–862. CrossRef Medline

Dietrich CJ, Morad M (2010) Synaptic acidification enhances GABAA signaling. J Neurosci 30:16044–16052. CrossRef Medline

Dugladze T, Schmitz D, Whittington MA, Vida I, Gloveli T (2012) Segregation of axonal and somatic activity during fast network oscillations. Science 336:1458–1461. CrossRef Medline

Fry CH, Poole-Wilson PA (1981) Effects of acid-base changes on excitation-contraction coupling in guinea-pig and rabbit cardiac ventricular muscle. J Physiol-London 313:141–160. Medline

Fülle HJ, Vassar R, Foster DC, Yang RB, Axel R, Garbers DL (1995) A recep-

CHAPTER 4

Developmental Regulation and Neuroprotective Effects of Striatal Tonic $GABA_A$Currents

DEVELOPMENTAL REGULATION AND NEUROPROTECTIVE EFFECTS OF STRIATAL TONIC $GABA_A$ CURRENTS

V. SANTHAKUMAR,[a1] R. T. JONES[a,b] AND I. MODY[a]*

[a]*Departments of Neurology and Physiology, David Geffen School of Medicine at the University of California, Los Angeles, CA 90095, USA*

[b]*Neurobiology Graduate Program, University of California, Los Angeles, CA 90095, USA*

Abstract—Striatal neurons are known to express $GABA_A$ receptor subunits that underlie both phasic and tonic inhibition. Striatal projection neurons, or medium spiny neurons (MSNs), are divided into two classes: MSNs containing the dopamine D1 receptor (D1-MSNs) form the direct pathway to the substantia nigra and facilitate movement while MSNs expressing the dopamine D2 receptor (D2-MSNs) form the pallidal pathway that inhibits movement. Consequently, modulating inhibition in distinct classes of MSNs will differentially impact downstream network activity and motor behavior. Given the powerful role of extrasynaptic inhibition in controlling neuronal excitability, we examined the nature of striatal tonic inhibition and its potential role in preventing excitotoxicity. Consistent with earlier studies in young (P16–P25) mice, tonic GABA currents in D2-MSNs were larger than in D1-MSNs. However, with age (>P30 mice) the tonic GABA currents increased in D1-MSNs but decreased in D2-MSNs. These data demonstrate a developmental switch in the MSN subtype expressing larger tonic GABA currents. Compared to wild-type, MSNs from adult mice lacking the $GABA_AR$ δ subunit (*Gabrd*$^{-/-}$ mice) had both decreased tonic GABA currents and reduced survival following an *in vitro* excitotoxic challenge with quinolinic acid. Furthermore, muscimol-induced tonic GABA currents were accompanied by reduced acute swelling of striatal neurons after exposure to NMDA in WT mice but not in *Gabrd*$^{-/-}$ mice. Our data are consistent with a role for tonic inhibition mediated by $GABA_AR$ δ subunits in neuroprotection against excitotoxic insults in the adult striatum.

Key words: medium spiny neuron, excitotoxicity, Huntington's disease, cell swelling, delta subunit.

The striatum, a major input nucleus of the basal ganglia, is crucial for extrapyramidal motor processing and psychomotor behaviors (Nakano et al., 2000; Schultz, 2006; Balleine et al., 2007). Both the local-circuit and projection neurons of the striatum are inhibitory (Tepper et al., 2004), with cortical and thalamic afferents constituting the primary source of excitation. Over 95% of the striatal neurons are medium spiny neurons (MSNs), which are GABAergic projection neurons. MSNs are divided into two classes based on their axonal projection and differential expression of dopamine receptor subtypes (Gerfen et al., 1990). MSNs that contain the dopamine D1 receptor (D1-MSNs) give rise to the direct pathway projections to the basal ganglia output nuclei, which includes the internal segment of the globus pallidus (GP_i) and the substantia nigra. Activation of the direct pathway disinhibits the thalamus and facilitates movement (Le et al., 1991; Wilson, 2007). The indirect, pallidal projecting, MSNs express the dopamine D2 receptor (D2-MSNs) and result in inhibition of movement (Gerfen and Young, 1988; Surmeier and Kitai, 1994). Given its pivotal role in feedback regulation of movement, it is not surprising that degenerative diseases affecting striatal circuits, such as Huntington's and Parkinson's disease, are associated with severe motor deficits.

Medium spiny neurons receive afferent excitation and local-circuit inhibition and are also synaptically interconnected through GABAergic collaterals (Wilson and Groves, 1980; Koos et al., 2004; Taverna et al., 2008). Given the preponderance of inhibitory connections, striatal neurons express an abundance of $GABA_A$ receptor ($GABA_AR$) subunits including α1–5, β1–3, γ1–3 and δ (Fujiyama et al., 2000; Schwarzer et al., 2001). The subunit composition of the pentameric $GABA_ARs$ varies depending on their anatomical location (Pirker et al., 2000), and developmental stage, and determines the physiological and pharmacological properties of GABA currents (Hevers and Luddens, 1998; Mody and Pearce, 2004). Generally, $GABA_ARs$ containing a γ subunit in combination with α and β subunits are located at the synapse and mediate fast phasic transmission. Receptors containing δ in combination with α4 or α5 subunits form high affinity extrasynaptic receptors that open tonically in low ambient GABA levels and give rise to a steady-state GABA conductance. Interestingly, recent studies in young (P16–25) mice have indicated that a higher expression of $GABA_AR$ containing α5 subunits in D2-MSNs, as compared to D1-MSNs, may contribute to the larger tonic GABA currents of D2-MSNs in young mice (Ade et al., 2008; Janssen et al., 2009). However, $GABA_AR$ subunits are developmentally regulated, with a progressive decline in α5 subunits and an increase in α4

[1] Present address: Department of Neurology and Neuroscience, UMDNJ-New Jersey Medical School, MSB-H-512, 185 S. Orange Avenue, Newark, NJ 07103, USA.

*Correspondence to: I. Mody, Department of Neurology, NRB1 Rm 575DThe David Geffen School of Medicine at UCLA, 635 Charles Young Drive South, Los Angeles, CA 90095, USA. Tel: +1-310-206-4481; fax: +1-310-825-0033.

E-mail address: mody@ucla.edu (I. Mody).

Abbreviations: aCAF, artificial cerebro spinal fluid; AP-5, D-2-amino-5-phosphonovalerate; BMI, bicuculline methiodide; DNQX, 6,7-Dinitroquinoxaline-2,3-dione; D1, dopamine receptor type 1; D2, dopamine receptor type 2; GABA, γ-aminobutyric acid; $GABA_AR$, $GABA_A$ receptor; GFP, green fluorescent protein; IR-DIC, infrared-differential interference contrast; L655, 708, 11,12,13,13a-tetrahydro-7-methoxy-9-oxo-9H-imidazo[1,5-a]pyrrolo[2,1-c][1,4]benzodiazepine-1-carboxylic acid, ethyl ester; MSN, medium spiny neuron; NMDA, N-Methyl-D-aspartic acid; NO-711, 1-[2-[[(diphenylmethylene)imino]oxy]ethyl]-1,2,5,6-tetrahydro-3-pyridine carboxylic acid hydrochloride.

0306-4522/10 $ - see front matter © 2010 IBRO. Published by Elsevier Ltd. All rights reserved.
doi:10.1016/j.neuroscience.2010.02.048

and δ subunits in the adult striatum (Laurie et al., 1992). Previous studies have also demonstrated an increase in tonic inhibition in striatal MSNs during development (Kirmse et al., 2008). Therefore, it is possible that the magnitude of, and the $GABA_AR$ subunit contribution to, tonic GABA currents in adult striatal neurons may be different from those in the developing striatum.

Inhibitory regulation of the adult striatum is of considerable interest due to the vulnerability of striatal MSNs to excitotoxic damage which has been suggested to contribute to neurodegenerative diseases, such as Huntington's disease (Graveland et al., 1985; Vonsattel et al., 1985). Tonic inhibition can greatly decrease cellular excitability (Farrant and Nusser, 2005), suggesting that extrasynaptic GABAergic inhibition could also reduce vulnerability to excitotoxic injury. The selective loss of projections from presumed D2-MSNs in Huntington's disease (Reiner et al., 1988) is consistent with a differential MSNs vulnerability in neurodegenerative disease. Therefore, we examined whether differences in the amplitude of tonic GABA currents between adult D1- and D2-MSNs may contribute to non-uniform MSN loss during excitotoxic insults, and whether augmenting tonic inhibition could protect against excitotoxic injury. Parts of this study have been previously presented as an abstract at the Society for Neuroscience (Santhakumar and Mody, 2008).

EXPERIMENTAL PROCEDURES

Animals

Young (16–25 day old) and adult (>P30) male *Drd2-EGFP* (D2-GFP) and *Drd1a-EGFP* (D1-GFP) mice (Gong et al., 2003; generously provided by Dr. X William Yang at the University of California, Los Angeles) back-crossed for >10 generations with C57BL/6 mice were used in experiments distinguishing between MSNs expressing D1 and D2 subtype of dopamine receptors. Adult C57BL/6 and *Gabrd*$^{-/-}$ on the same genetic background (Jackson Laboratories, Bar Harbor, ME, USA) were used in experiments characterizing the role of the $GABA_AR$ δ subunit in striatal inhibition. Since previous studies have shown that striatal MSNs express either D1 or D2 dopamine receptors (Gerfen et al., 1990; Day et al., 2008), D2-GFP mice were used in a majority of the experiments and GFP-negative MSNs were presumed to express the D1 dopamine receptor (Kreitzer and Malenka, 2007; Gertler et al., 2008; Ade et al., 2008). While recording from GFP-negative MSNs in D2-GFP mice, care was taken to record from cells located at the same depth where GFP-positive cells were also visible. Additionally, we determined the responses of GFP-negative striatal neurons to positive current injections and excluded those with firing characteristics of interneurons from further analysis. Moreover, data from confirmatory experiments performed in D1-GFP mice were similar to those using D2-GFP mice and the results from the two strains were pooled.

Slice preparation

Mice were anesthetized with halothane (Halocarbon laboratories, River Edge, NJ, USA) and decapitated according to a protocol approved by the UCLA Chancellor's Animal Research Committee. All efforts were made to minimize the number of animals and to reduce their suffering. Coronal brain slices (350 μm) were cut on a Leica VT1000S (Wetzlar, Germany) or a Microm HM 650 V (Thermo Scientific, Walldorf, Germany) in ice-cold sucrose artificial CSF (sucrose-aCSF) containing (in mM) 85 NaCl, 75 sucrose, 24 $NaHCO_3$, 25 D-glucose, 4 $MgCl_2$, 2.5 KCl, 1.25 NaH_2PO_4, and 0.5 $CaCl_2$. A sodium-free slicing solution containing (in mM) 135 N-methyl-D-glucamine, 130 HCl, 20 Choline-HCO_3, 10 D-glucose, 1.5 $MgCl_2$, 1.2 KH_2PO_4, 1.0 KCl and 0.5 $CaCl_2$ which was recently shown to promote interneuronal viability (Tanaka et al., 2008) was used to prepare slices for experiments measuring NMDA currents (Fig. 4D, E). Slices were incubated at 32±1 °C for 30 min in a submerged holding chamber containing an equal volume of sucrose-aCSF and recording aCSF and subsequently held at room temperature. The recording aCSF contained (in mM) 126 NaCl, 2.5 KCl, 2 $CaCl_2$, 2 $MgCl_2$, 1.25 NaH_2PO_4, 26 $NaHCO_3$, 10 D-glucose, 1 glutamine and 1.5 Na-Pyruvate. All solutions were saturated with 95% O_2 and 5% CO_2 and maintained at a pH of 7.4.

Electrophysiology

Slices were transferred to a submerged recording chamber and perfused with oxygenated aCSF at 34±1 °C. The perfusing aCSF contained the glutamate receptor antagonists D-2-amino-5-phosphonovalerate (10 μM D-AP-5, Tocris, Ellisville, MO, USA), 6,7-Dinitroquinoxaline-2,3-dione (25 μM DNQX, Tocris, Ellisville, MO, USA) and 5 μM GABA (Sigma-Aldrich, St. Louis, MO, USA). Green fluorescent protein (GFP) expression of the neurons was determined under epi-fluorescence microscopy (Fig. 1B) and striatal medium spiny neurons were recorded under IR-DIC videomicroscopy. Whole-cell voltage- and current-clamp recordings from dorsal striatal MSNs were obtained at a holding potential of −70 mV using Axon Instruments MultiClamp 700A (Molecular Devices, Sunnyvale, CA, USA). Recordings were low-pass filtered at 3 kHz and acquired with custom written LabView-based software (EVAN) at 10-kHz. The recording microelectrodes (5–7 MΩ) contained (in mM): 125 KCl, 10 K-Gluconate, 2 $MgCl_2$, 10 HEPES, 0.2 EGTA, 2 MgATP, 0.5 NaGTP, and 10 phospho-creatine at a pH of 7.26. Only cells showing the firing properties characteristic of MSNs (Kreitzer and Malenka, 2007; Ade et al., 2008) in response to depolarizing current steps were included in the analysis. Recordings were discontinued if series resistance increased by >25%. In some experiments, the GABA uptake inhibitor 1-[2-[[(diphenylmethylene)imino]oxy]ethyl]-1,2,5,6-tetrahydro-3-pyridinecarboxylic acid hydrochloride (10 μM NO-711, Sigma-Aldrich, St. Louis, MO, USA) and an inverse agonist selective for $GABA_ARs$ containing the α5 subunit (100 nM L655,708, Tocris, Ellisville, MO, USA) were included in the external solution. Tonic GABA current, the steady-state current blocked by the $GABA_AR$ antagonist bicuculline methiodide (100 μM BMI, Sigma-Aldrich, St. Louis, MO, USA) was measured using custom macros in IgorPro6.0 software (WaveMetrics, Lake Oswego, OR, USA) as described previously (Glykys and Mody, 2007). All salts were purchased from Sigma–Aldrich (St. Louis, MO, USA).

Experiments examining NMDA current–voltage relationships were performed in the presence of the $GABA_A$ antagonist, picrotoxin (100 μM) and the non-NMDA glutamate receptor antagonist 6,7-Dinitroquinoxaline-2,3-dione (DNQX, 25 μM, Tocris, Ellisville, MO, USA or Sigma, St. Louis, MO, USA). Whole-cell voltage-clamp recordings were obtained using Axopatch 200A (Molecular Devices, Sunnyvale, CA, USA) with a cesium based internal solution containing (in mM): 140 CsCl, 4 NaCl, 1 $MgCl_2$, 10 HEPES, 0.1 EGTA, 2 MgATP, 5 QX-314 at a pH of 7.26. MSNs were voltage clamped at −65 mV for 3–5 min before application of the voltage ramp protocol. The voltage was ramped from −65 to +40 mV for 1 s, followed by a 0.5 s holding period at +40 mV and a second ramp from +40 to −100 mV for 1 s and a return to −65 mV over 0.5 s. The ramps were repeated five times, with 15 s between each ramp. The averages of the five current traces obtained in the absence of NMDA were subtracted from those obtained after a 1–3 min perfusion of 10 or 50 μM NMDA to construct the NMDA current–voltage curves for each cell.

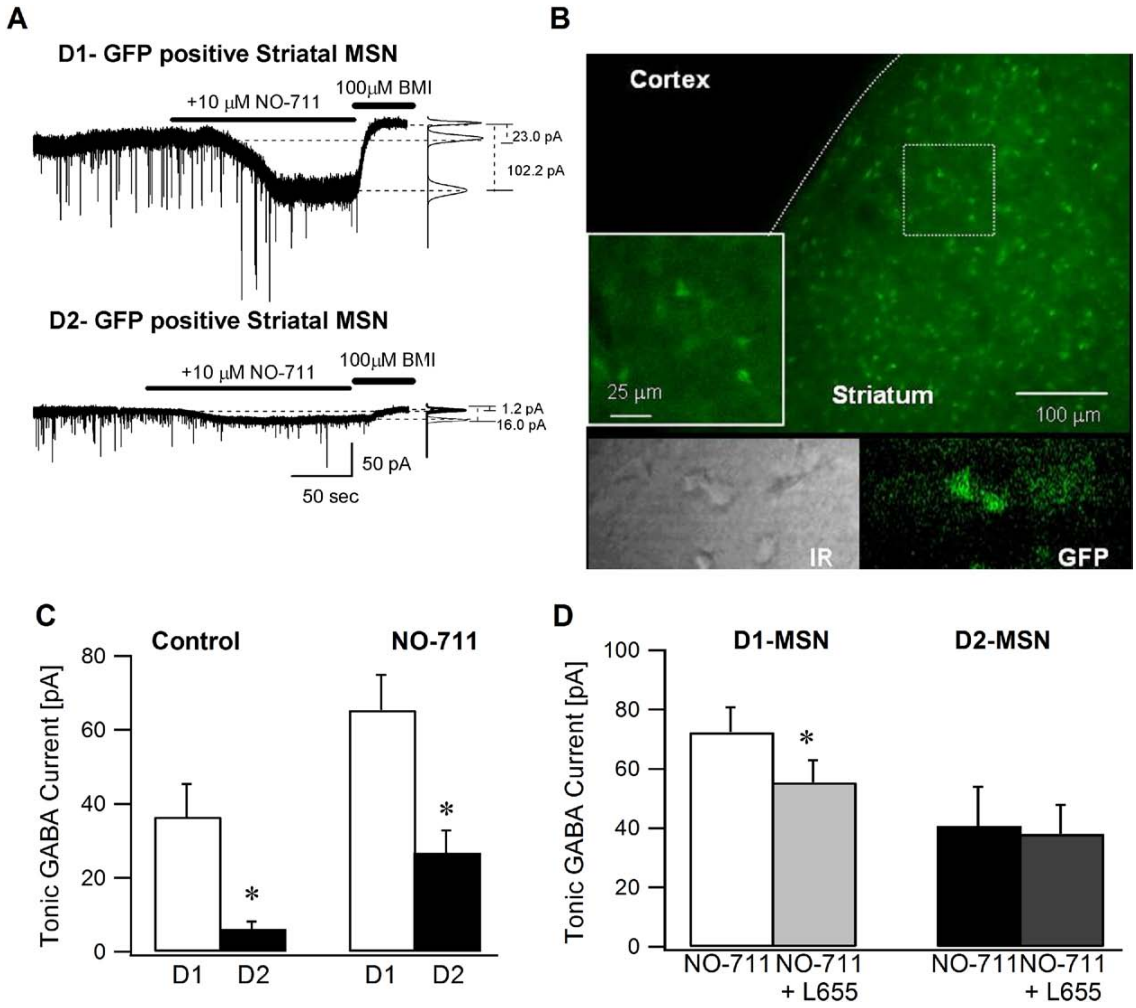

Fig. 1. Adult striatal medium spiny neurons expressing D1 receptors have larger tonic GABA currents. (A) Representative voltage-clamp recordings ($V_h = -70$ mV) from adult D1-MSNs (above) and D2-MSNs (below) illustrate the magnitude of tonic GABA current blocked by a saturating concentration of BMI (100 μM). Panels to the right show Gaussian fits to all-points histograms derived from 30 s recording periods in control conditions and in the presence of the GABA transporter-1 blocker NO-711 (10 μM) and a 15 s recording period during the perfusion of BMI used to determine the tonic current. The dashed lines indicate the Gaussian means and the difference currents are noted. (B) Confocal image of a cortico–striatal slice from a D2-GFP mouse shows that the GFP expression is restricted to the striatum. Inset illustrates a magnified image of the boxed area. The lower panel shows an IR-DIC (left) and fluorescence image (right) of a representative cortico-striatal slice from a D2-GFP mouse. (C) Summary histogram of the tonic GABA currents in D1- and D2-MSNs under control conditions and in the presence of the GABA transporter antagonist NO-711. (D) Histogram shows the effect of L655,708 (100 nM), an inverse benzodiazepine site agonist selective for $GABA_AR$ containing the α5 subunit on tonic inhibition in adult D1- and D2-MSNs in the presence of 10 μM NO-711. Tonic GABA currents were recorded in the presence of glutamate receptor blockers and 5 μM GABA. Asterisk denotes a statistically significant ($P<0.05$) difference in mean values using Student *t*-test.

Live-dead assay

Striatal slices from age-matched adult C57/BL6 and *Gabrd*$^{-/-}$ mice were prepared on the same day and incubated for 1 h at room temperature in quinolinic acid (0.5 mM QA, Tocris, Ellisville, MO, USA). Following incubation in quinolinic acid, the slices were incubated in 4 μM of ethidium homodimer-1 (to highlight the dead cells in red) and 2 μM of calcein acetoxymethyl ester (to highlight the live cells in green) in the dark for 30 min (LIVE/DEAD stain from Molecular Probes, Carlsbad, CA, USA). The slices were then washed in control aCSF at room temperature for 15 min (Monette et al., 1998). Care was taken to incubate pairs of slices from C57/BL6 and *Gabrd*$^{-/-}$ mice simultaneously in the various solutions. The number of live and dead cells in a given field of view was quantified at a depth of 30–70 μm below the surface of the slice using a 40× objective and epi-fluorescence microscopy with the appropriate filters (Ratzliff et al., 2004). Specifically, in each genotype a primary observer visualized and counted the green cells with calcein at a depth of 30 μm (where live cells were seen below slicing induced cell damage) and the number of live cells with calcein was determined by focusing down to a depth of 70 μm. Only cells showing localized somatic fluorescence were counted. Then the filters were changed and the observer counted the number of dead cells incorporating ethidium in the same field. Only cells with the strong nuclear staining within the observed depth and field were counted and care was taken to exclude the profiles with bleed through fluorescence from deeper cells. The correspondence between the depth at which the calcein and ethidium profiles were visualized was verified by switching filters

to ascertain that the counting was done at identical levels. A second investigator blind to the genotype obtained confocal image stacks from a depth of 30–70 μm in two slices each from a WT and *Gabrd*$^{-/-}$ mouse. The percent cell loss quantified using the confocal image stacks was not statistically different from those reported by the primary observer and the data from the two observations were pooled. Images for illustrative purposes were obtained using a confocal microscope with a 10× objective.

Cell swelling measurement

To assess NMDA induced swelling, slices were transferred to the submerged recording chamber and perfused for 6–8 min with control aCSF followed by 10 min perfusion of 50 μM NMDA (Sigma-Aldrich, St. Louis, MO, USA). The effect of muscimol (Tocris, Ellisville, MO, USA) on NMDA induced swelling was examined by perfusing the slices with muscimol (50 nM) first for 4–6 min followed by aCSF containing muscimol and NMDA (50 μM). Experiments were performed at room temperature and images at 40× magnification were acquired at 2 min intervals using a WAT-992H3 camera coupled to a Snappy image capture system. Cell outlines were determined using the "Cell Outliner" plugin or by manual selection of ROI in ImageJ Software (National Institutes of Health, Bethesda, MD, USA). Cell area and perimeter were calculated in ImageJ based on the outline. Data are presented as the percent increase in area or perimeter of a given cell 8–10 min after NMDA perfusion relative to the measurements obtained in the control period. No visible swelling was observed during a 15 min perfusion of aCSF or muscimol (50 nM, $n=2$ slices).

Statistics

All data are shown as mean±SEM. Statistical analysis was performed by paired and unpaired Student's *t*-test (Microsoft Excel) and two-way ANOVA with *post hoc* comparisons performed by Bonferroni's post-test (GraphPad Prism software, La Jolla CA, USA). Significance was set to $P\leq0.05$.

RESULTS

Adult striatal D1-MSNs express larger tonic GABA currents

Using coronal slices from adult (>P30) male *Drd2-EGFP* and *Drd1a-EGFP* mice (Gong et al., 2003) to distinguish between neurons expressing D1 and D2 subtype of dopamine receptors (Fig. 1B), we examined the magnitude of tonic GABA currents in the two types of striatal MSNs. Since previous studies have shown that MSNs express either D1 or D2 dopamine receptors (Gerfen et al., 1990), *Drd2-EGFP* mice were used in a majority of the experiments and GFP-negative MSNs were presumed to express the D1 dopamine receptor. Additionally, we examined the firing characteristics of all recorded neurons to distinguish between MSNs and striatal interneurons (Kawaguchi, 1993, 1995; Taverna et al., 2007).

The amplitude of tonic GABA currents in medium spiny neurons from adult mice was significantly larger in D1-MSN (36.5±8.9 pA, in $n=6$ cells from four mice, of which two were D1-GFP cells) compared to D2-MSN (6.2±2.0 pA in $n=9$ cells from five mice $P<0.05$) (Fig. 1A, C). The input resistance (R_{in}), measured as the voltage deflection elicited by a 400 pA hyperpolarizing current step from a membrane potential of −70 mV, was not significantly different between D1-MSN (126.17±9.65 MΩ) and D2-MSN (149.14±21.9 MΩ). R_{in} was measured in glutamate and $GABA_A$ receptor antagonists. Similarly, in the presence of glutamate and $GABA_A$ receptor antagonists, the difference in the current needed to hold D1- and D2-MSN at −70 mV (I_{hold}) did not reach statistical significance (D1-MSN: 25.8±26.4 pA and D2-MSN: 7.54±28.93 pA). The GABA transporter-1 (GAT-1) antagonist NO-711 (10 μM), added after recording the baseline currents in aCSF, enhanced tonic GABA currents in five of the six D1-MSN (63.8±8.5 pA, average of all six cells) and all D2-MSN (25.4±6.8 pA). In additional experiments performed in the presence of NO-711, tonic GABA currents were significantly larger in D1-MSN (D1-MSN: 65.4±9.5 pA in $n=13$ cells from nine mice; D2-MSN: 26.8±6.1 pA in $n=12$ cells from seven mice, $P<0.05$; Fig. 1C). In contrast to previous reports suggesting that adult MSN lack tonic GABA currents (Gertler et al., 2008), and in agreement with Janssen et al. (2009) we find that tonic GABA currents are expressed in adult MSNs. Our results demonstrate that in adult mice, D1-MSNs, which contribute to the direct pathway, have larger tonic GABA currents than D2-MSN that give rise to the indirect pathway.

$GABA_A$ receptors containing δ subunits mediate tonic GABA currents in adult striatal MSNs

$GABA_AR$ $\alpha5$ and δ subunits are expressed in the striatum (Laurie et al., 1992; Schwarzer et al., 2001), both subunits are known to mediate extrasynaptic inhibition. Since $GABA_AR$ subunit expression is developmentally regulated (Laurie et al., 1992), we examined which $GABA_AR$ subunits underlie tonic GABA currents in adult MSNs. In the presence of NO-711 (10 μM), to augment extrasynaptic GABA levels, perfusion of the $\alpha5$ selective $GABA_AR$ inverse agonist L655,708 (100 nM) caused a small decrease (22.7±6.7%) in tonic GABA currents in D1-MSNs (Fig. 1D; tonic GABA currents: 72.3±8.5 pA in NO-711 and 55.4±7.5 pA in L655,708 in $n=17$ cells from eight mice, $P<0.05$). Conversely, L655,708 failed to decrease tonic GABA currents in D2-MSN (Fig. 1D; tonic GABA currents: 40.7±13.2 pA in NO-711 and 38.0±7.3 pA in L655, 708; $n=9$ cells from five mice, $P>0.05$) indicating minimal contribution from receptors with $\alpha5$ subunits.

Next, we examined the contribution of $GABA_AR$ δ subunit to striatal extrasynaptic GABA currents using mice lacking the δ subunit (*Gabrd*$^{-/-}$ mice). Only cells that showed the delayed, repetitive non-adapting firing pattern characteristic of MSNs (Kawaguchi et al., 1989; Ade et al., 2008) were included in the analysis. Compared to wild-type, the magnitude of tonic GABA currents were significantly decreased in MSNs from *Gabrd*$^{-/-}$ mice (WT: 17.3±6.1 pA in $n=10$ cells from six mice; *Gabrd*$^{-/-}$: 1.8±1.1 pA in $n=8$ cells from four mice, $P<0.05$) (Fig. 2A, B). Similarly, tonic GABA currents in the presence of NO-711(10 μM) were also larger in the wild-type mice (56.2±8.1 pA in $n=9$ cells from six mice) compared to *Gabrd*$^{-/-}$ mice (15.8±1.1 pA in $n=8$ cells from four mice, $P<0.05$). The presence of the long whiskers, indicating the spread of data, in the box plot from wild-type mice (Fig. 2B) demonstrate the high degree of variability in the amplitude of tonic GABA currents (0 to

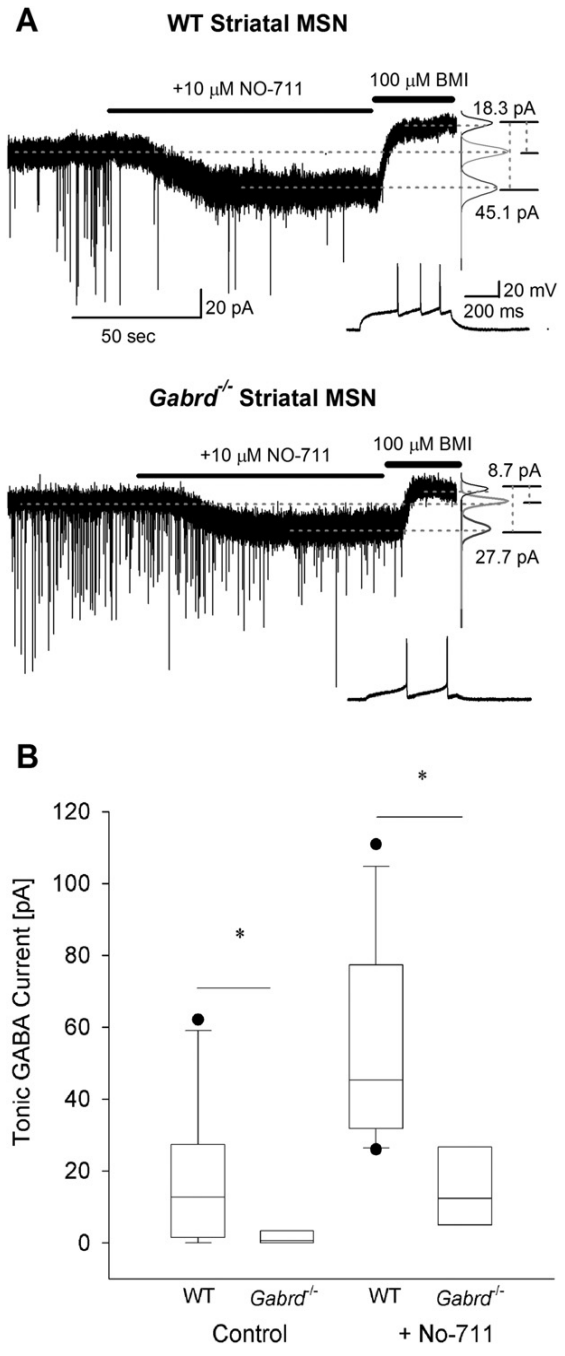

Fig. 2. Tonic GABA currents are decreased in *Gabrd*$^{-/-}$ mice lacking $GABA_A$ receptor delta subunits. (A) Example voltage-clamp traces from striatal MSNs in adult wild-type (above) and *Gabrd*$^{-/-}$ mice (below) show the difference in tonic GABA currents in control conditions and in the presence of NO-711 (10 μM) between the two genotypes. Recordings were obtained at a holding potential of -70 mV. To the right are panels showing Gaussian fits to all-points histograms derived from 30 s recording periods in control conditions and in the presence of NO-711 (10 μM) and a 15 s recording period during the perfusion of BMI used to determine the tonic current. The difference currents are noted to the right were calculated from the Gaussian means indicated by the dashed lines. Inset shows the characteristic firing pattern of the MSNs recorded in response to a depolarizing current injection ($+80$ pA in the WT in the upper panel and $+20$ pA in *Gabrd*$^{-/-}$ in the lower panel) from a holding potential of -70 mV. (B) Summary box-plot shows the decrease in tonic GABA currents in MSNs from *Gabrd*$^{-/-}$ mice in the absence and presence of NO-711. The upper and lower sides of the box represent the upper /lower quartiles and the median value is represented as a line. The maximum and minimum values are represented by the extent of the whiskers with outliers shown as black dots. Asterisk denotes a statistically significant ($P<0.05$) difference in mean values using Student's *t*-test. Recordings were obtained in the presence of glutamate receptor blockers and 5 μM GABA.

62.1 pA in aCSF and 26.0 to 110.9 pA in 10 μM NO-711) in MSNs from wild-type mice. This wide range is consistent with the inclusion of currents from both D1- and D2-MSNs among the recorded neurons. In contrast, tonic GABA currents in MSNs from *Gabrd*$^{-/-}$mice were confined to a narrow range of 0 to 8.7 pA under control conditions and 5.0 to 35.2 pA in NO-711 (10 μM), suggesting that the amplitude of tonic GABA currents in D1- and D2-MSNs was not different in *Gabrd*$^{-/-}$ mice (Fig. 2A, B). In four of four cells recorded in NO-711, the α5 selective inverse agonist L655,708 decreased tonic GABA currents in MSNs from wild-type mice (77.4$\pm$13.4 pA in NO-711 and 56.2$\pm$8.5 pA in L655,708 in $n=4$ cells from two mice, $P<0.05$). However, in MSNs from *Gabrd*$^{-/-}$ mice, the effect of L655,708 on tonic GABA currents was variable with a decrease observed in nine out of 15 cells tested (53.6$\pm$5.0 pA in NO-711 and 31.9$\pm$9.7 pA in L655,708, $n=9$ cells from five mice, $P<0.05$) and an increase in six out of 15 cells which did not reach statistical significance (37.3$\pm$11.1 pA in NO-711 and 42.0$\pm$10.2 pA in L655,708, $n=6$ cells from five mice, $P>0.05$). Interestingly, the R_{in} of WT MSNs in the presence of glutamate and $GABA_A$ receptor antagonists was significantly greater than in MSN from *Gabrd*$^{-/-}$mice (WT: 167.04$\pm$17.33 MΩ, *Gabrd*$^{-/-}$: 118.52$\pm$7.22 MΩ; $P<0.05$) suggesting the presence of compensatory changes to account for decreases in $GABA_A$ conductance in *Gabrd*$^{-/-}$ mice.

Taken together, these data demonstrate that in contrast to MSNs from young mice (Janssen et al., 2009), δ subunit-containing $GABA_A$Rs underlie the differential expression of tonic GABA currents between D1 and D2-MSNs in the adult striatum. The results also suggest that both $GABA_A$R α5 and δ subunits are expressed in adult D1-MSNs with the δ subunits contributing a major fraction of extrasynaptic GABA currents in adult MSN.

Developmental changes in tonic GABA currents in striatal MSNs

Contrary to our findings in adult MSNs, recent studies have shown that the magnitude of tonic GABA currents is larger in D2-MSNs than in D1-MSNs in young mice (Ade et al., 2008; Janssen et al., 2009). To determine whether these conflicting results were due to developmental differences, we examined the magnitude and cell type specificity of tonic GABA currents in young animals. Consistent with the earlier study (Ade et al., 2008) and in contrast to adult MSNs, we found that the amplitude of tonic GABA currents in P16–25 mice was significantly lower in the D1-MSNs (5.8$\pm$1.5 pA in $n=13$ cells from seven mice) than in D2-

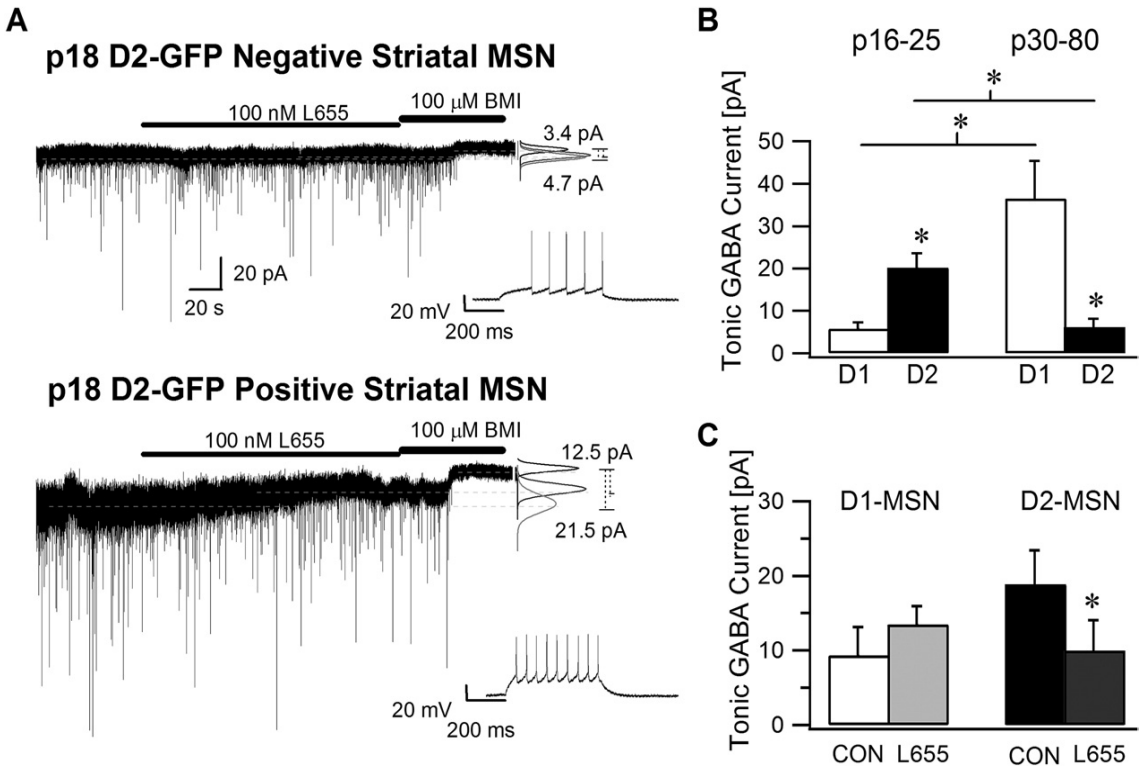

Fig. 3. Striatal medium spiny neurons expressing D2 receptors have larger tonic GABA currents in young mice. (A) Recordings from a representative D1-MSN (above) and D2-MSN (below) from juvenile (P18) D2-GFP mice show the tonic GABA current blocked by a saturating concentration of BMI (100 μM). The effect of the α5 selective $GABA_A$ receptor inverse agonist, L655,708 (100 nM) on tonic GABA currents in D1 and D2-MSN is also illustrated. As before, the graphs to the right show Gaussian fits to all-points histograms derived from 30 s periods in control and L655,708 and a 15 s recording in BMI with dashed lines indicating the means used to calculate the tonic current. Inset shows the characteristic firing pattern of the MSN recorded in response to a depolarizing current injection (+120 pA) from a holding potential of −70 mV. (B) Summary data compare the tonic GABA currents in juvenile D1- and D2-MSNs with the tonic GABA currents from adult D1 and D2-MSNs (same as control data as in Fig. 1C) under control conditions in the presence of glutamate receptor blockers and 5 μM GABA. (C) Histogram shows the effect of L655,708 (100 nM) on tonic GABA currents in juvenile D1- and D2-MSNs. All recordings were performed at a holding potential at −70 mV. Asterisk denotes a statistically significant ($P<0.05$) difference in mean values.

MSNs (20.2±.3.4 pA in $n=16$ cells from eight mice, $P<0.05$) (Fig. 3A, B). Notably, while there is an increase in tonic current in D1-MSNs during development (Young: 5.8±1.5 pA; Adult; 36.5±8.9 pA, $P<0.01$), there appears to be a developmental decrease in extrasynaptic GABA currents in D2-MSNs (Young: 20.2±.3.4 pA; Adult; 6.2± 2.0 pA, $P<0.01$) (Fig. 3B). The R_{in} and I_{hold} of young D1- and D2-MSNs measured in the presence of glutamate and $GABA_A$ receptor antagonists were not statistically different (D1-MSN: $R_{in}=147.32\pm6.25$ MΩ and I_{hold} @ −70 mV= −34.23±20.04 pA and D2-MSN: $R_{in}=186.83\pm18.93$ MΩ and I_{hold} @ −70 mV=−64.2±64.9 pA). Although the developmental changes in R_{in} and I_{hold} did not reach statistical significance, the observed trend is consistent with previous studies showing that MSNs in young mice have more depolarized resting membrane potentials and higher input resistances compared to MSNs from adult mice (Kirmse et al., 2008).

Interestingly, the contribution of $GABA_AR$ containing the α5 subunit to tonic GABA currents is also altered during development. In contrast to its effect in adult D1-MSN, where L655,708 (100 nM) decreased tonic GABA currents (Fig. 1D), L655,708 (100 nM) failed to block tonic GABA currents in D1-MSNs from young mice (9.3±3.8 pA in control and 13.4±2.5 pA in L655,708, $n=5$ cells from three mice, $P>0.05$) (Fig. 3C). Moreover, although L655,708 (100 nM) had no effect on tonic GABA currents in adult D2-MSNs (Fig. 1D), it significantly reduced tonic GABA currents in D2-MSNs from young mice (18.8±4.6 pA in control and 10.0±4.1 pA in L655,708, $n=7$ cells from three mice, $P<0.05$) (Fig. 3C). These findings reconcile our data with earlier reports in young mice (Ade et al., 2008) and demonstrate that developmental regulation of the $GABA_AR$ subunits contributing to tonic GABA currents differs between D1- and D2-MSNs.

Tonic GABA currents protect against excitotoxic neuronal injury

Given the correlation between our findings of enhanced tonic GABA currents in adult D1-MSNs and the relative sparing of the direct pathway in early neurodegenerative disease (Reiner et al., 1988; Albin et al., 1992; Deng et al., 2004), we examined whether extrasynaptic inhibition can

decrease excitotoxic damage. We subjected cortico–striatal slices from adult mice to excitotoxic damage by incubating slices from wild-type and *Gabrd*$^{-/-}$ mice in a selective NMDA receptor agonist, quinolinic acid (0.5 mM) for 1 h. Following the quinolinic acid treatment the cells were incubated in Calcein (2 μM) and Ethidium Homodimer-1 (4 μM) to identify the live (green calcein stained) and dead (red ethidium stained) cells. Exposure to quinolinic acid resulted in a greater cell loss in slices from *Gabrd*$^{-/-}$ mice (Fig. 4A, B). Summary data in Fig. 4C, show that following quinolinic acid exposure, 54.5$\pm$1.8% (n=259/478 cells from 10 slices in three mice) of the wild-type cells survived. However, a significantly lower proportion of cells from *Gabrd*$^{-/-}$ mice (43.1$\pm$2.2%; n=201/475 cells from nine slices in three mice, $P<0.05$) survived the 1 h incubation in quinolinic acid (Fig. 4C). Additional experiments were per-

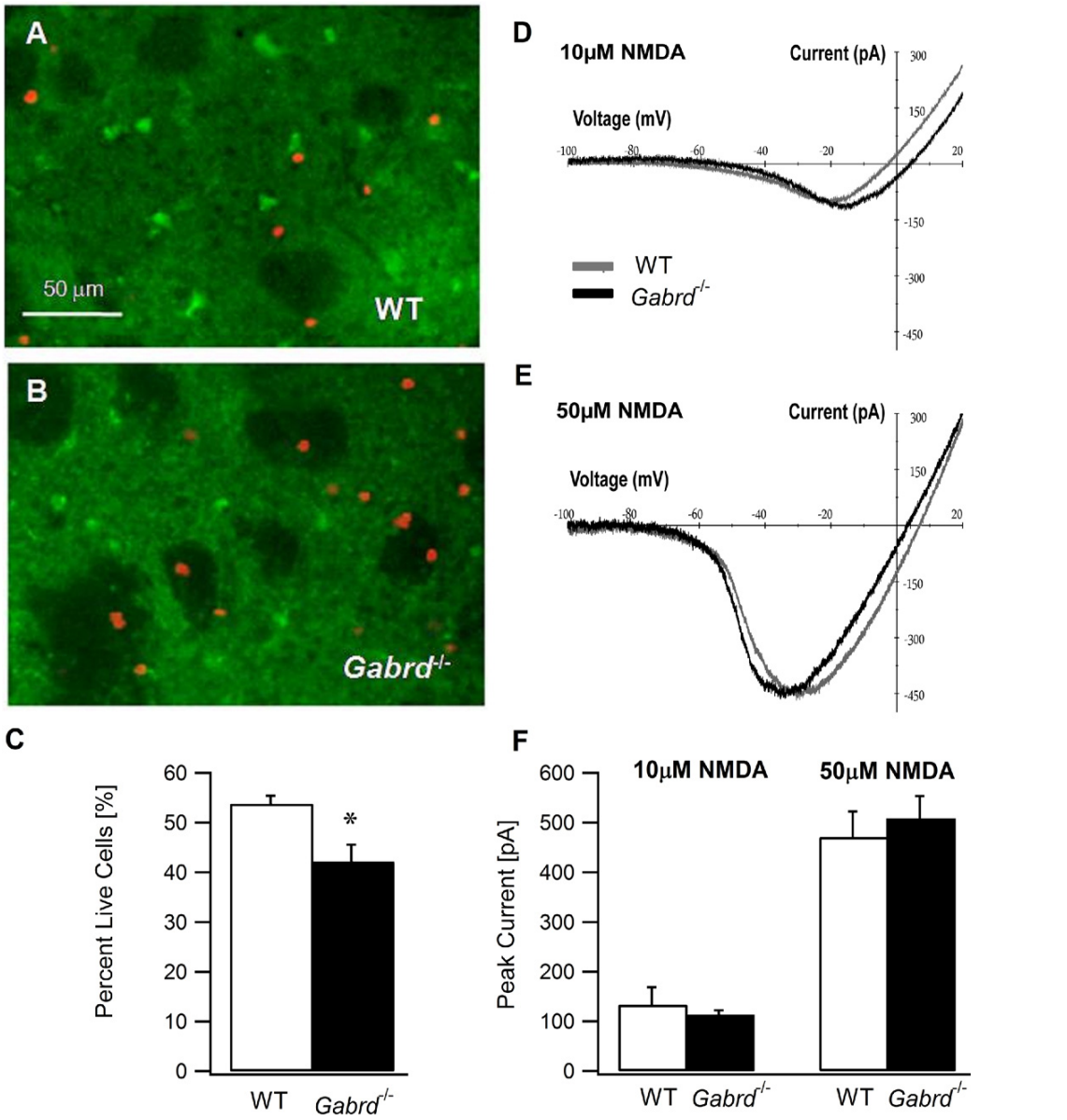

Fig. 4. Enhanced susceptibility of striatal MSNs in *Gabrd*$^{-/-}$ mice to excitotoxic cell death. (A, B) Confocal photomicrograph of cortico–striatal slices from a wild-type mouse (A) and a *Gabrd*$^{-/-}$ mouse (B) showing the assay for live and dead cells following *in vitro* exposure to quinolinic acid (0.5 mM, 1 h). The live cells are stained with Calcein (in green) and dead cells incorporate the nuclear stain Ethidium Homodimer-1 (in red). Both Calcein and Ethidium Homodimer-1 images of a given field of view were obtained at 10$\times$ using appropriate filters and overlaid for illustration. (C) Summary data show the percent of MSNs that survive an hour long *in vitro* exposure to the excitotoxin quinolinic acid (0.5 mM) in wild-type and *Gabrd*$^{-/-}$ mice. (D, E) Representative NMDA current–voltage plots obtained in MSNs from adult wild-type and *Gabrd*$^{-/-}$ mice illustrate comparable peak NMDA currents and voltage-dependence in the presence 10 μM (D) and 50 μM (E) NMDA. (F) Summary histogram shows that the peak NMDA currents are similar in MSNs of wild type and *Gabrd*$^{-/-}$ mice. Asterisk denote a statistically significant ($P<0.05$) difference.

formed to examine whether differences in NMDA currents between MSNs from wild-type and *Gabrd*$^{-/-}$ mice could contribute to the enhanced toxicity of quinolinic acid in *Gabrd*$^{-/-}$ mice. The peak currents induced by 10 and 50 μM NMDA during a voltage ramp protocol (see Experimental Procedures) and their voltage-dependence were not different between wild-type and *Gabrd*$^{-/-}$ mice (Fig. 3D–F; average peak currents in 10 μM NMDA: WT: 133.6±34.9 pA, n=4 cells and *Gabrd*$^{-/-}$: 113.6±8.5 pA, n=3 cells, P>0.1, unpaired t-test; in 50 μM NMDA: WT: 470.9±51.7 pA and *Gabrd*$^{-/-}$: 508.4±45.2 pA, P>0.1, unpaired t-test). These findings indicate that deletion of the $GABA_AR$ δ subunit does not enhance NMDA currents in MSNs. Since $GABA_AR$ δ subunit is the major determinant of tonic inhibition in the adult striatum, we reason that the increased cell vulnerability in *Gabrd*$^{-/-}$ mice indicates that tonic GABA conductance decreases excitotoxic cell death in adult MSN.

Finally, we investigated whether selectively enhancing tonic GABA currents could decrease the swelling and striatal cell death induced by exposure to NMDA. This *in vitro* model has been previously used to simulate excitotoxic cell death in Huntington's disease, making it an ideal assay to test our hypothesis (McGeer and McGeer, 1976; Schwarcz and Coyle, 1977; Colwell and Levine, 1996). Under IR-DIC imaging, we exposed striatal slices to NMDA (50 μM) for 10 min either in control aCSF or in the presence of muscimol (50 nM), a δ subunit selective $GABA_AR$ agonist (Shivers et al., 1989; Mihalek et al., 1999) which preferentially enhances tonic inhibition at the low concentrations used in this study (Glykys and Mody, 2006). As expected, exposing wild-type slices in control aCSF to NMDA for 10 min resulted in swelling of the striatal cells (Fig. 5A, B), with an increase in both the cell area (82.1±13.4% increase) and cell perimeter (30.1±7.1% increase, in n=17 cells from six slices in three mice, P<0.01). Muscimol (50 nM) decreased the magnitude of cell swelling induced by NMDA in slices from wild-type mice (Fig. 5C, D). In muscimol, NMDA increased cell area by 27.8±6.0% (P<0.01) and failed to increase the cell perimeter (8.4±2.8% increase, P>0.05 in n=36 cells from 10 slices in four mice). The effect of muscimol in reducing the excitotoxic increase in cell area (Fig. 5I) and perimeter was statistically significant (P<0.05). To determine whether GABA currents through receptors containing δ subunits underlie the neuroprotection by muscimol, we tested the ability of muscimol to decreases excitotoxic cell swelling in *Gabrd*$^{-/-}$ mice. As with the wild-type, NMDA perfusion caused swelling of striatal neurons in slices from *Gabrd*$^{-/-}$ mice incubated in aCSF (81.2±6.6% increase in cell area, P<0.01 and 24.6±2.9% increase in cell perimeter, P<0.05 in n=34 cells from nine slices in three mice) (Fig. 5E, F). However, in contrast to the results from the wild-type, muscimol (50 nM) did not decrease NMDA induced cell swelling in *Gabrd*$^{-/-}$ mice (87.4±10.9% increase in cell area, P<0.01 and 28.9±3.9% increase in cell perimeter, P<0.05 in n=41 cells from 10 slices in three mice) (Fig. 5G, H). Summary data (Fig. 5I) show the genotype specific difference in the effect of muscimol treatment which was confirmed by two way ANOVA (interaction between genotype and muscimol treatment: $F_{(1,125)}$=10.05; P<0.01; effect of treatment with muscimol: $F_{(1,125)}$=6.38; P<0.05; and effect of genotype: $F_{(1,125)}$=9.45; P<0.01). These results are consistent with a role for $GABA_A$ receptors containing δ subunits in mediating the neuroprotective action of muscimol. Taken together, these data demonstrate that tonic inhibition mediated by $GABA_AR$ containing δ subunits protects striatal neurons from excitotoxic cell injury.

DISCUSSION

Although it has been known that the striatal medium spiny neurons expressing D1- and D2-dopamine receptors are two distinct neuronal classes (Gerfen and Young, 1988), it has been difficult to characterize the physiological differences between the two MSNs subtypes. Recent experiments using D1- and D2-BAC transgenic mice (Gong et al., 2003; Heintz, 2004) have revealed differences in the synaptic and intrinsic properties of the two types of MSNs (Kreitzer and Malenka, 2007; Day et al., 2008; Gertler et al., 2008; Ade et al., 2008; Cepeda et al., 2008; Valjent et al., 2009). Our results demonstrate differences in the $GABA_AR$ subunits underlying tonic GABA currents between adult D1- and D2-MSNs. Our data indicate that a decrease in the contribution of the $GABA_AR$ α5 subunit in D2-MSNs and an increase in the tonic GABA currents mediated by $GABA_AR$ containing the δ subunit in adult D1-MSNs might underlie the developmental reversal in the tonic GABA current profile of MSNs. Unlike certain active and passive neuronal properties that distinguish D1- and D2-MSNs, which are not different between young and adult mice (Gertler et al., 2008), tonic GABA currents are larger in D2-MSNs in young (P16–25) mice and in D1-MSNs in the adult (>P30) mice. We demonstrate that striatal neurons from adult mice lacking the $GABA_AR$ δ subunit are more vulnerable to excitotoxic cell death and that pharmacologically-enhancing tonic inhibition decreases the excitotoxic cell swelling. Overall, our results are consistent with a neuroprotective role of tonic inhibition in striatal excitotoxic injury, which has been proposed to contribute to neurodegenerative diseases.

Developmental regulation of striatal tonic inhibition

Earlier studies have identified the developmental regulation of GABA receptor expression in the striatum (Laurie et al., 1992) and a progressive developmental enhancement of tonic inhibition in MSNs (Kirmse et al., 2008). Therefore, we expected an increase in the magnitude of tonic inhibition in striatal neurons during development. However, in agreement with Janssen et al. (2009), we found an alteration in the subset of striatal MSN that demonstrate larger tonic GABA currents with maturation of the circuit. What are the changes that account for this developmental switch in tonic inhibition? In young (P16–25) mice, an inverse agonist specific for the $GABA_A$ receptor α5 subunit appears to preferentially decrease tonic GABA currents in D2-MSNs and abolish the differences in extrasynaptic inhibition between the D1- and D2-MSNs (Fig. 3D and Ade et al., 2008). Thus, in young mice, the expression of

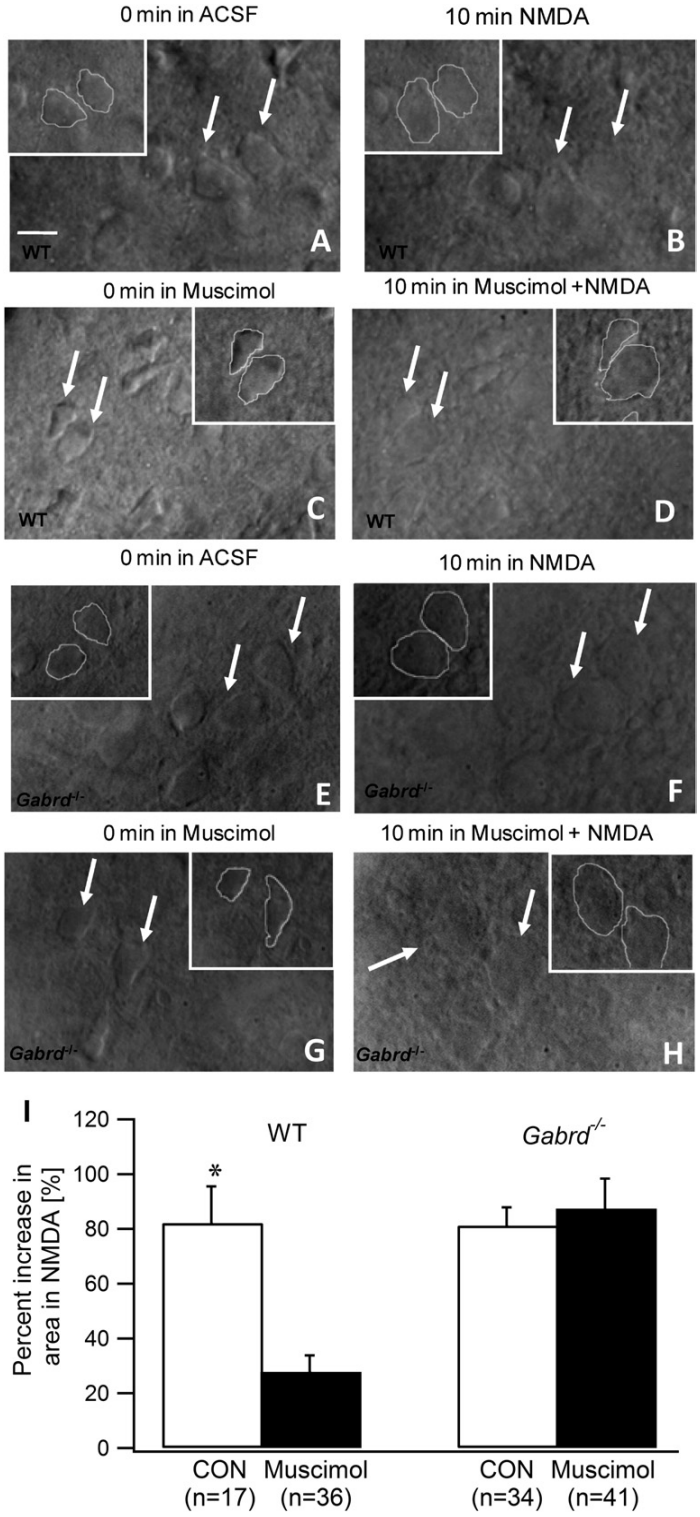

Fig. 5. Enhancement of tonic currents mediated by δ subunit-containing $GABA_A$Rs decreases excitotoxic cell swelling of MSNs. (A–D). Illustrative IR-DIC images of wild-type striatal MSN obtained using a 40× objective show the MSNs before (A) and 10 min after exposure 50 μM NMDA (B) show the swelling and indistinct outlines after NMDA exposure in aCSF ($n=17$ cells from six slices in three mice). Images from slices in which tonic inhibition was selectively enhanced by a 5 min perfusion of 50 nM muscimol before (C) and during the 10 min exposure to 50 μM NMDA (D) show that muscimol decreases NMDA induced swelling in MSNs ($n=36$ cells from 10 slices in four mice). Insets show outlines used to measure the area and perimeter of the cells indicated by

$GABA_AR$ $\alpha5$ subunits in D2-MSNs accounts for the enhanced tonic GABA currents. The $GABA_AR$ $\alpha5$ subunit selective inverse agonist L655,708 did not decrease the small tonic GABA currents observed in D1-MSNs suggesting that $GABA_ARs$ with other subunits might underlie these currents. THIP, a preferential agonist of GABA receptors containing δ subunits (Brown et al., 2002), augments tonic GABA currents in both D1- and D2-MSNs alike (Ade et al., 2008). Therefore, it is likely that $GABA_AR$ δ subunits contribute to part of the extrasynaptic inhibition in young mice. However, the absence of changes in the distribution of tonic GABA currents in MSNs from young *Gabrd*$^{-/-}$ mice (Janssen et al., 2009) indicates that the contribution of $GABA_AR$ δ subunits to tonic GABA currents in young MSNs is minimal. In the adult striatum, we find a marked increase in tonic GABA currents in D1-MSNs. The dramatic decrease in extrasynaptic GABA currents in MSN from *Gabrd*$^{-/-}$ mice (Fig. 3) suggests that increased expression of $GABA_AR$ δ subunits underlies the enhanced tonic inhibition in adult D1-MSNs. Furthermore, L655,708, which had no effect on D1-MSNs in young mice, decreases tonic GABA currents in adult D1-MSNs (Fig. 1D) indicating that in addition to δ subunits, the contribution of $GABA_AR$ $\alpha5$ subunits to tonic GABA currents is also increased in adult D1-MSNs. In contrast, the amplitude of tonic GABA currents undergoes a statistically significant developmental decrease in D2-MSNs. Moreover, tonic currents in adult D2-MSNs are not blocked by L655,708 which indicates a developmental decrease in the contribution of $GABA_AR$ $\alpha5$ subunits to tonic GABA currents in these cells. The results of our physiological studies are in agreement with earlier anatomical studies showing a decrease in the expression of $\alpha5$ subunit and an increase in expression of $\alpha4$ and δ subunit with striatal development (Laurie et al., 1992). This developmental switch in tonic inhibitory control of the striatal output neurons from the indirect pathway to those of the direct pathway is likely to alter the input processing in the striatal circuit.

Role in shaping membrane properties

There are several differences between the physiological properties of D1- and D2-MSNs. D1-MSNs rest at a more hyperpolarized membrane potential, have a lower input resistance (Gertler et al., 2008) and are less excitable than D2-MSNs. A recent study examined the mechanisms underlying the difference in passive membrane properties of adult D1 and D2-MSNs but failed to find differences in extrasynaptic inhibition between adult D1 and D2-MSNs (Gertler et al., 2008). Our findings that tonic GABA currents in adult D1-MSNs is greater than in D2-MSNs are consistent with a recent report (Janssen et al., 2009) and indicate a role for extrasynaptic inhibition in shaping the passive membrane properties of adult D1-MSNs. Since MSNs rest at hyperpolarized membrane potentials (Gertler et al., 2008) likely to be more negative than the reversal potential of GABA currents, it is not clear if tonic GABA currents would be depolarizing or hyperpolarizing. However, the shunting conductance provided by tonically open extrasynaptic GABA receptors is likely to contribute to the lower input resistance (Gertler et al., 2008) and decreased excitability (Kreitzer and Malenka, 2007) of adult D1-MSNs. Indeed, the oscillation of MSN membrane potential between up and down states close to the GABA reversal potential can render GABA currents either depolarizing or hyperpolarizing (Bracci and Panzeri, 2006). However, the membrane shunting effects of tonic GABAergic conductance should decrease the excitability of MSN with tonic GABA currents and reduce excitotoxic damage. It is intriguing to speculate that a shunting tonic inhibition in the adult striatum may selectively decrease the excitability of the direct pathway (D1-MSN), allowing for selective facilitation of behaviorally relevant inputs, while the indirect pathway (D2-MSN), with a much lower level of tonic inhibition, can be more readily activated to suppress unintended movement.

Protection against excitotoxic cell damage

Loss of striatal medium spiny neurons is the pathological hallmark of Huntington's disease, an autosomal dominant neurodegenerative movement disorder (Huang et al., 1995; Estrada Sanchez et al., 2008). Early experiments have shown that *in vivo* injection of the NMDA agonist, quinolinic acid, into the striatum can reproduce the cell loss and behavioral alterations in Huntington's disease. Studies on striatal tissue from patients with Huntington's disease have demonstrated that fibers containing enkephalin, presumed to arise from D2-MSNs, are selectively lost relatively early in the disease process while the striato–nigral fibers enriched in Substance P are relatively intact (Reiner et al., 1988). Interestingly, D1 but not D2 dopamine receptors have been shown to enhance potentially excitotoxic NMDA currents in MSNs (Surmeier et al., 2007), suggesting that the susceptibility to glutamate alone may not account for the differential cell loss. Our findings that tonic GABA currents are enhanced in adult D1-MSN which appear less vulnerable to degeneration are consistent with a potential neuroprotective role for tonic inhibition. Our results demonstrating increased excitotoxic striatal cell loss without changes in NMDA currents in *Gabrd*$^{-/-}$ mice, in conjunction with larger δ subunit mediated tonic GABA currents in adult MSNs, support the role for tonic inhibition in protecting against excitotoxic cell death in D1-MSN.

Huntington's disease is characterized by progressive and differential neuronal loss with early degeneration of

the arrows. (E–H). Images of striatal MSNs from *Gabrd*$^{-/-}$ mice before (E) and 10 min after exposure 50 μM NMDA (F) show the NMDA induced swelling (n=34 cells from nine slices in three mice). Images obtained following enhancement of tonic inhibition by muscimol before (G) and during the 10 min exposure to NMDA (H) show that muscimol does not protect against NMDA induced swelling of MSNs in *Gabrd*$^{-/-}$ mice (n=41 cells from 10 slices in three mice). Insets show outlines used to measure the area and perimeter of the cells indicated by the arrows. Scale bar in (A) represents 10 μm. (I) Summary histogram shows the degree of NMDA induced increase in cell area in wild-type and *Gabrd*$^{-/-}$ mice in the absence and presence of muscimol. Asterisk denotes a statistically significant (P<0.05) difference.

$GABA_AR$ $\alpha5$ subunits in D2-MSNs accounts for the enhanced tonic GABA currents. The $GABA_AR$ $\alpha5$ subunit selective inverse agonist L655,708 did not decrease the small tonic GABA currents observed in D1-MSNs suggesting that $GABA_ARs$ with other subunits might underlie these currents. THIP, a preferential agonist of GABA receptors containing δ subunits (Brown et al., 2002), augments tonic GABA currents in both D1- and D2-MSNs alike (Ade et al., 2008). Therefore, it is likely that $GABA_AR$ δ subunits contribute to part of the extrasynaptic inhibition in young mice. However, the absence of changes in the distribution of tonic GABA currents in MSNs from young *Gabrd*$^{-/-}$ mice (Janssen et al., 2009) indicates that the contribution of $GABA_AR$ δ subunits to tonic GABA currents in young MSNs is minimal. In the adult striatum, we find a marked increase in tonic GABA currents in D1-MSNs. The dramatic decrease in extrasynaptic GABA currents in MSN from *Gabrd*$^{-/-}$ mice (Fig. 3) suggests that increased expression of $GABA_AR$ δ subunits underlies the enhanced tonic inhibition in adult D1-MSNs. Furthermore, L655,708, which had no effect on D1-MSNs in young mice, decreases tonic GABA currents in adult D1-MSNs (Fig. 1D) indicating that in addition to δ subunits, the contribution of $GABA_AR$ $\alpha5$ subunits to tonic GABA currents is also increased in adult D1-MSNs. In contrast, the amplitude of tonic GABA currents undergoes a statistically significant developmental decrease in D2-MSNs. Moreover, tonic currents in adult D2-MSNs are not blocked by L655,708 which indicates a developmental decrease in the contribution of $GABA_AR$ $\alpha5$ subunits to tonic GABA currents in these cells. The results of our physiological studies are in agreement with earlier anatomical studies showing a decrease in the expression of $\alpha5$ subunit and an increase in expression of $\alpha4$ and δ subunit with striatal development (Laurie et al., 1992). This developmental switch in tonic inhibitory control of the striatal output neurons from the indirect pathway to those of the direct pathway is likely to alter the input processing in the striatal circuit.

Role in shaping membrane properties

There are several differences between the physiological properties of D1- and D2-MSNs. D1-MSNs rest at a more hyperpolarized membrane potential, have a lower input resistance (Gertler et al., 2008) and are less excitable than D2-MSNs. A recent study examined the mechanisms underlying the difference in passive membrane properties of adult D1 and D2-MSNs but failed to find differences in extrasynaptic inhibition between adult D1 and D2-MSNs (Gertler et al., 2008). Our findings that tonic GABA currents in adult D1-MSNs is greater than in D2-MSNs are consistent with a recent report (Janssen et al., 2009) and indicate a role for extrasynaptic inhibition in shaping the passive membrane properties of adult D1-MSNs. Since MSNs rest at hyperpolarized membrane potentials (Gertler et al., 2008) likely to be more negative than the reversal potential of GABA currents, it is not clear if tonic GABA currents would be depolarizing or hyperpolarizing. However, the shunting conductance provided by tonically open extrasynaptic GABA receptors is likely to contribute to the lower input resistance (Gertler et al., 2008) and decreased excitability (Kreitzer and Malenka, 2007) of adult D1-MSNs. Indeed, the oscillation of MSN membrane potential between up and down states close to the GABA reversal potential can render GABA currents either depolarizing or hyperpolarizing (Bracci and Panzeri, 2006). However, the membrane shunting effects of tonic GABAergic conductance should decrease the excitability of MSN with tonic GABA currents and reduce excitotoxic damage. It is intriguing to speculate that a shunting tonic inhibition in the adult striatum may selectively decrease the excitability of the direct pathway (D1-MSN), allowing for selective facilitation of behaviorally relevant inputs, while the indirect pathway (D2-MSN), with a much lower level of tonic inhibition, can be more readily activated to suppress unintended movement.

Protection against excitotoxic cell damage

Loss of striatal medium spiny neurons is the pathological hallmark of Huntington's disease, an autosomal dominant neurodegenerative movement disorder (Huang et al., 1995; Estrada Sanchez et al., 2008). Early experiments have shown that *in vivo* injection of the NMDA agonist, quinolinic acid, into the striatum can reproduce the cell loss and behavioral alterations in Huntington's disease. Studies on striatal tissue from patients with Huntington's disease have demonstrated that fibers containing enkephalin, presumed to arise from D2-MSNs, are selectively lost relatively early in the disease process while the striato–nigral fibers enriched in Substance P are relatively intact (Reiner et al., 1988). Interestingly, D1 but not D2 dopamine receptors have been shown to enhance potentially excitotoxic NMDA currents in MSNs (Surmeier et al., 2007), suggesting that the susceptibility to glutamate alone may not account for the differential cell loss. Our findings that tonic GABA currents are enhanced in adult D1-MSN which appear less vulnerable to degeneration are consistent with a potential neuroprotective role for tonic inhibition. Our results demonstrating increased excitotoxic striatal cell loss without changes in NMDA currents in *Gabrd*$^{-/-}$ mice, in conjunction with larger δ subunit mediated tonic GABA currents in adult MSNs, support the role for tonic inhibition in protecting against excitotoxic cell death in D1-MSN.

Huntington's disease is characterized by progressive and differential neuronal loss with early degeneration of

the arrows. (E–H). Images of striatal MSNs from *Gabrd*$^{-/-}$ mice before (E) and 10 min after exposure 50 μM NMDA (F) show the NMDA induced swelling (n=34 cells from nine slices in three mice). Images obtained following enhancement of tonic inhibition by muscimol before (G) and during the 10 min exposure to NMDA (H) show that muscimol does not protect against NMDA induced swelling of MSNs in *Gabrd*$^{-/-}$ mice (n=41 cells from 10 slices in three mice). Insets show outlines used to measure the area and perimeter of the cells indicated by the arrows. Scale bar in (A) represents 10 μm. (I) Summary histogram shows the degree of NMDA induced increase in cell area in wild-type and *Gabrd*$^{-/-}$ mice in the absence and presence of muscimol. Asterisk denotes a statistically significant (P<0.05) difference.

the striatal projections from presumed D2-MSNs to the external segment of the Globus Pallidus. Since glutamate excitotoxicity is known to contribute to striatal cell loss, several clinical trials have examined the effects of various NMDA receptor antagonists to prevent glutamate toxicity in neurodegenerative diseases (Murman et al., 1997; Kremer et al., 1999; Lucetti et al., 2002; Beister et al., 2004). However, the outcome of these studies have been variable (Estrada Sanchez et al., 2008). Our results show that enhancing tonic inhibition decreases NMDA-induced cell swelling in MSN and suggest that selective enhancement of extrasynaptic GABAergic inhibition could reduce excitotoxic injury to the striatum.

CONCLUSION

We have demonstrated a developmental switch in the MSN subtype expressing tonic GABA currents, and using pharmacological and genetic tools we have identified the respective $GABA_A$ receptor subunits involved. We further show that tonically active $GABA_A$ receptors can protect against excitotoxic damage of striatal neurons. Therefore, the differential expression of extrasynaptic $GABA_A$ receptors can influence developmental changes in striatal information processing and may thwart striatal neuronal vulnerability in neurological diseases.

Acknowledgments—We thank Dr. X William Yang for providing us the Drd2-EGFP and Drd1a-EGFP mice and Dr. Yijun Cui for help with genotyping the mice, and Dr. Seema Tiwari-Woodruff for help with confocal imaging. We also thank Mahsan Rafizadeh and Reyes Main Lazaro for their help with maintaining the animal colonies and genotyping. This work was supported by NIH Grant NS30549 and the Coelho Endowment to I.M.

REFERENCES

Ade KK, Janssen MJ, Ortinski PI, Vicini S (2008) Differential tonic GABA conductances in striatal medium spiny neurons. J Neurosci 28:1185–1197.

Albin RL, Reiner A, Anderson KD, Dure LS, Handelin B, Balfour R, Whetsell WO Jr, Penney JB, Young AB (1992) Preferential loss of striato-external pallidal projection neurons in presymptomatic Huntington's disease. Ann Neurol 31:425–430.

Balleine BW, Delgado MR, Hikosaka O (2007) The role of the dorsal striatum in reward and decision-making. J Neurosci 27:8161–8165.

Beister A, Kraus P, Kuhn W, Dose M, Weindl A, Gerlach M (2004) The N-methyl-D-aspartate antagonist memantine retards progression of Huntington's disease. J Neural Transm Suppl 68:117–122.

Bracci E, Panzeri S (2006) Excitatory GABAergic effects in striatal projection neurons. J Neurophysiol 95:1285–1290.

Brown N, Kerby J, Bonnert TP, Whiting PJ, Wafford KA (2002) Pharmacological characterization of a novel cell line expressing human alpha(4)beta(3)delta GABA(A) receptors. Br J Pharmacol 136:965–974.

Cepeda C, Andre VM, Yamazaki I, Wu N, Kleiman-Weiner M, Levine MS (2008) Differential electrophysiological properties of dopamine D1 and D2 receptor-containing striatal medium-sized spiny neurons. Eur J Neurosci 27:671–682.

Colwell CS, Levine MS (1996) Glutamate receptor-induced toxicity in neostriatal cells. Brain Res 724:205–212.

Day M, Wokosin D, Plotkin JL, Tian X, Surmeier DJ (2008) Differential excitability and modulation of striatal medium spiny neuron dendrites. J Neurosci 28:11603–11614.

Deng YP, Albin RL, Penney JB, Young AB, Anderson KD, Reiner A (2004) Differential loss of striatal projection systems in Huntington's disease: a quantitative immunohistochemical study. J Chem Neuroanat 27:143–164.

Estrada Sanchez AM, Mejia-Toiber J, Massieu L (2008) Excitotoxic neuronal death and the pathogenesis of Huntington's disease. Arch Med Res 39:265–276.

Farrant M, Nusser Z (2005) Variations on an inhibitory theme: phasic and tonic activation of GABA(A) receptors. Nat Rev Neurosci 6:215–229.

Fujiyama F, Fritschy JM, Stephenson FA, Bolam JP (2000) Synaptic localization of GABA(A) receptor subunits in the striatum of the rat. J Comp Neurol 416:158–172.

Gerfen CR, Engber TM, Mahan LC, Susel Z, Chase TN, Monsma FJ Jr, Sibley DR (1990) D1 and D2 dopamine receptor-regulated gene expression of striatonigral and striatopallidal neurons. Science 250:1429–1432.

Gerfen CR, Young WS III (1988) Distribution of striatonigral and striatopallidal peptidergic neurons in both patch and matrix compartments: an in situ hybridization histochemistry and fluorescent retrograde tracing study. Brain Res 460:161–167.

Gertler TS, Chan CS, Surmeier DJ (2008) Dichotomous anatomical properties of adult striatal medium spiny neurons. J Neurosci 28:10814–10824.

Glykys J, Mody I (2006) Hippocampal network hyperactivity after selective reduction of tonic inhibition in GABA A receptor alpha5 subunit-deficient mice. J Neurophysiol 95:2796–2807.

Glykys J, Mody I (2007) The main source of ambient GABA responsible for tonic inhibition in the mouse hippocampus. J Physiol 582:1163–1178.

Gong S, Zheng C, Doughty ML, Losos K, Didkovsky N, Schambra UB, Nowak NJ, Joyner A, Leblanc G, Hatten ME, Heintz N (2003) A gene expression atlas of the central nervous system based on bacterial artificial chromosomes. Nature 425:917–925.

Graveland GA, Williams RS, DiFiglia M (1985) Evidence for degenerative and regenerative changes in neostriatal spiny neurons in Huntington's disease. Science 227:770–773.

Heintz N (2004) Gene expression nervous system atlas (GENSAT). Nat Neurosci 7:483.

Hevers W, Luddens H (1998) The diversity of GABAA receptors. Pharmacological and electrophysiological properties of GABAA channel subtypes. Mol Neurobiol 18:35–86.

Huang Q, Zhou D, Sapp E, Aizawa H, Ge P, Bird ED, Vonsattel JP, DiFiglia M (1995) Quinolinic acid-induced increases in calbindin D28k immunoreactivity in rat striatal neurons in vivo and in vitro mimic the pattern seen in Huntington's disease. Neuroscience 65:397–407.

Janssen MJ, Ade KK, Fu Z, Vicini S (2009) Dopamine modulation of GABA tonic conductance in striatal output neurons. J Neurosci 29:5116–5126.

Kawaguchi Y (1993) Physiological, morphological, and histochemical characterization of three classes of interneurons in rat neostriatum. J Neurosci 13:4908–4923.

Kawaguchi Y, Wilson CJ, Augood SJ, Emson PC (1995) Striatal interneurones: chemical, physiological and morphological characterization. Trends Neurosci 18:527–535.

Kawaguchi Y, Wilson CJ, Emson PC (1989) Intracellular recording of identified neostriatal patch and matrix spiny cells in a slice preparation preserving cortical inputs. J Neurophysiol 62:1052–1068.

Kirmse K, Dvorzhak A, Kirischuk S, Grantyn R (2008) GABA transporter 1 tunes GABAergic synaptic transmission at output neurons of the mouse neostriatum. J Physiol 586:5665–5678.

Koos T, Tepper JM, Wilson CJ (2004) Comparison of IPSCs evoked by spiny and fast-spiking neurons in the neostriatum. J Neurosci 24:7916–7922.

Kreitzer AC, Malenka RC (2007) Endocannabinoid-mediated rescue of striatal LTD and motor deficits in Parkinson's disease models. Nature 445:643–647.

Bibliography

Aimone JB, Deng W, Gage FH (2010a) Adult neurogenesis: integrating theories and separating functions. *Trends in cognitive sciences* 14:325–337. 27, 28

Aimone JB, Deng W, Gage FH (2010b) Put them out to pasture? What are old granule cells good for, anyway...? *Hippocampus* . 28

Aivar P, Valero M, Bellistri E, Menendez de la Prida L (2014) Extracellular calcium controls the expression of two different forms of ripple-like hippocampal oscillations. *The Journal of neuroscience : the official journal of the Society for Neuroscience* 34:2989–3004. 18

Babb TL, Kupfer WR, Pretorius JK, Crandall PH, Levesque MF (1991) Synaptic reorganization by mossy fibers in human epileptic fascia dentata. *Neuroscience* 42:351–363. 3

Behr J, Lyson KJ, Mody I (1998) Enhanced propagation of epileptiform activity through the kindled dentate gyrus. *Journal of Neurophysiology* 79:1726–1732. 3

Bengzon J, Kokaia Z, Elmér E, Nanobashvili A, Kokaia M, Lindvall O (1997) Apoptosis and proliferation of dentate gyrus neurons after single and intermittent limbic seizures. *Proceedings of the National Academy of Sciences of the United States of America* 94:10432–10437. 28

Bouilleret V, Ridoux V, Depaulis A, Marescaux C, Nehlig A, Le Gal La Salle G (1999) Recurrent seizures and hippocampal sclerosis following intrahippocampal kainate injection in adult mice: electroencephalography, histopathology and synaptic reorganization similar to mesial temporal lobe epilepsy. *Neuroscience* 89:717–729. 9

Bragin A, Benassi SK, Kheiri F, Engel J (2011) Further evidence that pathologic high-frequency oscillations are bursts of population spikes derived from recordings of identified cells in dentate gyrus. *Epilepsia* 52:45–52. 18

Bragin A, Engel J, Staba RJ (2010) High-frequency oscillations in epileptic brain. *Current opinion in neurology* 23:151–156. 36

Bragin A, Engel J, Wilson CL, Fried I, Mathern GW (1999) Hippocampal and entorhinal cortex high-frequency oscillations (100-500 Hz) in human epileptic brain and in kainic acid-treated rats with chronic seizures. *Epilepsia* 40:127–137. 3, 39

Bragin A, Mody I, Wilson CL, Engel J (2002) Local generation of fast ripples in epileptic brain. *The Journal of neuroscience : the official journal of the Society for Neuroscience* 22:2012–2021. 3, 17, 39

Bragin A, Wilson CL, Engel J (2000) Chronic epileptogenesis requires development of a network of pathologically interconnected neuron clusters: a hypothesis. *Epilepsia* 41 Suppl 6:S144–52. 2

Bragin A, Wilson CL, Almajano J, Mody I, Engel J (2004) High-frequency oscillations after status epilepticus: epileptogenesis and seizure genesis. *Epilepsia* 45:1017–1023. 3, 15, 17, 39

Bragin A, Wilson CL, Engel J (2003) Spatial stability over time of brain areas generating fast ripples in the epileptic rat. *Epilepsia* 44:1233–1237. 3, 17, 39

Bragin A, Wilson CL, Engel J (2007) Voltage depth profiles of high-frequency oscillations after kainic acid-induced status epilepticus. *Epilepsia* 48 Suppl 5:35–40. 3, 12, 39

Buckmaster PS, Dudek FE (1997) Neuron loss, granule cell axon reorganization, and functional changes in the dentate gyrus of epileptic kainate-treated rats. *The Journal of comparative neurology* 385:385–404. 3, 28

Buckmaster PS, Dudek FE (1999) In vivo intracellular analysis of granule cell axon reorganization in epileptic rats. *Journal of Neurophysiology* 81:712–721. 28

Buckmaster PS, Jongen-Rêlo AL (1999) Highly specific neuron loss preserves lateral inhibitory circuits in the dentate gyrus of kainate-induced epileptic rats. *The Journal of neuroscience : the official journal of the Society for Neuroscience* 19:9519–9529. 11, 18

Buzsáki G (2006) *Rhythms of the brain* Oxford University Press, New York. 3, 14

Buzsáki G, Horváth Z, Urioste R, Hetke J, Wise K (1992) High-frequency network oscillation in the hippocampus. *Science (New York, NY)* 256:1025–1027. 14

Buzsáki G, Wang XJ (2012) Mechanisms of Gamma Oscillations. *Annual Review of Neuroscience* 35:203–225. 36

Cameron HA, McKay R (2001) Adult neurogenesis produces a large pool of new granule cells in the dentate gyrus. *The Journal of comparative neurology* 435:406–417. 27

Chrobak JJ, Buzsáki G (1996) High-frequency oscillations in the output networks of the hippocampal-entorhinal axis of the freely behaving rat. *The Journal of neuroscience : the official journal of the Society for Neuroscience* 16:3056–3066. 3

Colquhoun D (1994) Practical analysis of single channel records In Ogden D, editor, *Microelectrode Techniques*, pp. 101–139. The Company of Biologists, Cambridge. 8, 13

Coulter, Sloviter, Macdonald (1999) Chronic epileptogenic cellular alterations in the limbic system after status epilepticus - Status epilepticus-induced neuronal injury and network reorganization - Discussion and questions from the audience. *Epilepsia* 40:S40–S41. 28

Csaba Z, Pirker S, Lelouvier B, Simon A, Videau C, Epelbaum J, Czech T, Baumgartner C, Sperk G, Dournaud P (2005) Somatostatin receptor type 2 undergoes plastic changes in the human epileptic dentate gyrus. *Journal of neuropathology and experimental neurology* 64:956–969. 11

Csaba Z, Richichi C, Bernard V, Epelbaum J, Vezzani A, Dournaud P (2004) Plasticity of

somatostatin and somatostatin sst2A receptors in the rat dentate gyrus during kindling epileptogenesis. *The European journal of neuroscience* 19:2531–2538. 11

Csicsvari J, Hirase H, Mamiya A, Buzsáki G (2000) Ensemble patterns of hippocampal CA3-CA1 neurons during sharp wave-associated population events. *Neuron* 28:585–594. 18

Desmond NL, Levy WBa (1982) A Quantitative Anatomical Study of the Granule Cell Dendritic Fields of the Rat Dentate Gyrus Using a Novel Probabilistic Method. *The Journal of comparative neurology* 212:131–145. 29

Dombeck DA, Khabbaz AN, Collman F, Adelman TL, Tank DW (2007) Imaging large-scale neural activity with cellular resolution in awake, mobile mice. *Neuron* 56:43–57. 6

Dyhrfjeld-Johnsen J, Santhakumar V, Morgan RJ, Huerta R, Tsimring L, Soltesz I (2007) Topological determinants of epileptogenesis in large-scale structural and functional models of the dentate gyrus derived from experimental data. *Journal of Neurophysiology* 97:1566–1587. 19, 29, 39

Engel J (1996) Clinical evidence for the progressive nature of epilepsy In Heinemann U, editor, *Progressive nature of epileptogenesis*, pp. 9–20. Elsevier Science, New York. 2

Engel J, Bragin A, Staba RJ, Mody I (2009) High-frequency oscillations: what is normal and what is not? *Epilepsia* 50:598–604. 12, 14, 36

Engel J, da Silva FL (2012) High-frequency oscillations - where we are and where we need to go. *Progress in neurobiology* 98:316–318. 18

Engel J, Pitkänen A, Loeb JA, Dudek FE, Bertram EH, Cole AJ, Moshe SL, Wiebe S, Jensen FE, Mody I, Nehlig A, Vezzani A (2013) Epilepsy biomarkers. *Epilepsia* 54 Suppl 4:61–69. 15

Eriksson PS, Perfilieva E, Björk-Eriksson T, Alborn AM, Nordborg C, Peterson DA, Gage FH (1998) Neurogenesis in the adult human hippocampus. *Nature medicine* 4:1313–1317. 27

Espósito MS, Piatti VC, Laplagne DA, Morgenstern NA, Ferrari CC, Pitossi FJ, Schinder AF (2005) Neuronal differentiation in the adult hippocampus recapitulates embryonic development. *The Journal of neuroscience : the official journal of the Society for Neuroscience* 25:10074–10086. 27

Franck JE, PokoRNY J, Kunkel DD, Schwartzkroin PA (1995) Physiological and Morphologic Characteristics of Granule Cell Circuitry in Human Epileptic Hippocampus. *Epilepsia* 36:543–558. 28

French JA, Williamson PD, Thadani VM, Darcey TM, Mattson RH, Spencer SS, Spencer DD (1993) Characteristics of medial temporal lobe epilepsy: I. Results of history and physical examination. *Annals of Neurology* 34:774–780. 2

Fritschy JM (2004) A new animal model of temporal lobe epilepsy. 9

Ge S, Yang CH, Hsu KS, Ming Gl, Song H (2007) A critical period for enhanced synaptic plasticity in newly generated neurons of the adult brain. *Neuron* 54:559–566. 28

Goldberg EM, Coulter DA (2013) Mechanisms of epileptogenesis: a convergence on neural circuit dysfunction. *Nature reviews Neuroscience* 14:337–349. 3, 19

Harvey CD, Collman F, Dombeck DA, Tank DW (2009) Intracellular dynamics of hippocampal place cells during virtual navigation. *Nature* 461:941–946. 6

Heinemann U, Beck H, Dreier JP, Ficker E, Stabel J, Zhang CL (1992) The dentate gyrus as a regulated gate for the propagation of epileptiform activity. *Epilepsy research. Supplement* 7:273–280. 3

Hesdorffer DC, Logroscino G, Cascino G, Annegers JF, Hauser WA (1998) Risk of unprovoked seizure after acute symptomatic seizure: effect of status epilepticus. *Annals of Neurology* 44:908–912. 2

Houser CR (1990) Granule cell dispersion in the dentate gyrus of humans with temporal lobe epilepsy. *Brain Research* 535:195–204. 3, 7

Ibarz JM, Foffani G, Cid E, Inostroza M, Menendez de la Prida L (2010) Emergent dynamics of fast ripples in the epileptic hippocampus. *The Journal of neuroscience : the official journal of the Society for Neuroscience* 30:16249–16261. 18

Jacobs J, Staba R, Asano E, Otsubo H, Wu JY, Zijlmans M, Mohamed I, Kahane P, Dubeau F, Navarro V, Gotman J (2012) High-frequency oscillations (HFOs) in clinical epilepsy. *Progress in neurobiology* 98:302–315. 18

Jadhav SP, Kemere C, German PW, Frank LM (2012) Awake Hippocampal Sharp-Wave Ripples Support Spatial Memory. *Science (New York, NY)* 336:1454–1458. 3

Jefferys JGR, Menendez de la Prida L, Wendling F, Bragin A, Avoli M, Timofeev I, Lopes da Silva FH (2012) Mechanisms of physiological and epileptic HFO generation. *Progress in neurobiology* 98:250–264. 18

Jiao Y, Nadler JV (2007) Stereological analysis of GluR2-immunoreactive hilar neurons in the pilocarpine model of temporal lobe epilepsy: correlation of cell loss with mossy fiber sprouting. *Experimental Neurology* 205:569–582. 18

Kobayashi M, Buckmaster PS (2003) Reduced inhibition of dentate granule cells in a model of temporal lobe epilepsy. *The Journal of neuroscience : the official journal of the Society for Neuroscience* 23:2440–2452. 17

Kron MM, Zhang H, Parent JM (2010) The developmental stage of dentate granule cells

dictates their contribution to seizure-induced plasticity. *The Journal of neuroscience : the official journal of the Society for Neuroscience* 30:2051–2059. 28, 35

Kumar SS, Jin X, Buckmaster PS, Huguenard JR (2007) Recurrent Circuits in Layer II of Medial Entorhinal Cortex in a Model of Temporal Lobe Epilepsy. *The Journal of neuroscience : the official journal of the Society for Neuroscience* 27:1239–1246. 17

Lauer M, Beckmann H, Senitz D (2003) Increased frequency of dentate granule cells with basal dendrites in the hippocampal formation of schizophrenics. *Psychiatry research* 122:89–97. 29

Lieberman DN, Mody I (1999) Properties of single NMDA receptor channels in human dentate gyrus granule cells. *The Journal of physiology* 518 (Pt 1):55–70. 8, 13

Lothman EW, Stringer JL, Bertram EH (1992) The dentate gyrus as a control point for seizures in the hippocampus and beyond. *Epilepsy research. Supplement* 7:301–313. 3

Lukasiuk K, Pitkänen A (2012) Molecular basis of acquired epileptogenesis. *Handbook of clinical neurology* 107:3–12. 3

Ma DK, Bonaguidi MA, Ming Gl, Song H (2009) Adult neural stem cells in the mammalian central nervous system. *Cell research* 19:672–682. 27

Maglóczky Z, Freund TF (1993) Selective neuronal death in the contralateral hippocampus following unilateral kainate injections into the CA3 subfield. *Neuroscience* 56:317–335. 18

Margerison JH, Corsellis JA (1966) Epilepsy and the temporal lobes. A clinical, electroencephalographic and neuropathological study of the brain in epilepsy, with particular reference to the temporal lobes. *Brain : a journal of neurology* 89:499–530. 10, 18

Marx M, Haas CA, Häussler U (2013) Differential vulnerability of interneurons in the epileptic hippocampus. *Frontiers in Cellular Neuroscience* 7:167. 4, 9, 39

Mayanagi Y, Walker AE (1975) DC potentials of temporal lobe seizures in the monkey. *Journal of neurology* 209:199–215. 12

McAuliffe JJ, Bronson SL, Hester MS, Murphy BL, Dahlquist-Topalá R, Richards DA, Danzer SC (2011) Altered patterning of dentate granule cell mossy fiber inputs onto CA3 pyramidal cells in limbic epilepsy. *Hippocampus* 21:93–107. 7, 10

McCormick DA, Contreras D (2001) On the cellular and network bases of epileptic seizures. *Annual review of physiology* 63:815–846. 17

McManus OB, Blatz AL, Magleby KL (1987) Sampling, log binning, fitting, and plotting durations of open and shut intervals from single channels and the effects of noise. *Pflgers Archiv European Journal of Physiology* 410:530–553. 8

Menendez de la Prida L, Trevelyan AJ (2011) Cellular mechanisms of high frequency oscillations in epilepsy: on the diverse sources of pathological activities. *Epilepsy Research* 97:308–317. 18

Mitsuya K, Nitta N, Suzuki F (2009) Persistent zinc depletion in the mossy fiber terminals in the intrahippocampal kainate mouse model of mesial temporal lobe epilepsy. *Epilepsia* 50:1979–1990. 10, 39

Morgan RJ, Soltesz I (2008) Nonrandom connectivity of the epileptic dentate gyrus predicts a major role for neuronal hubs in seizures. *Proceedings of the National Academy of Sciences of the United States of America* 105:6179–6184. 19, 29, 35

Noebels JL, Avoli M, Rogawski MA, Olsen RW, Delgado-Escueta AV, Sloviter RS, Bumanglag AV, Schwarcz R, Frotscher M (2012) *Abnormal dentate gyrus network circuitry in temporal lobe epilepsy* Jasper's Basic Mechanisms of the Epilepsies. National Center for Biotechnology Information (US), Bethesda (MD), 4th edition. 3, 18, 19

Overstreet-Wadiche LS, Bromberg DA, Bensen AL, Westbrook GL (2006) Seizures accelerate functional integration of adult-generated granule cells. *The Journal of neuroscience : the official journal of the Society for Neuroscience* 26:4095–4103. 28, 38

Parent JM, Yu TW, Leibowitz RT, Geschwind DH, Sloviter RS, Lowenstein DH (1997) Dentate granule cell neurogenesis is increased by seizures and contributes to aberrant network reorganization in the adult rat hippocampus. *The Journal of neuroscience : the official journal of the Society for Neuroscience* 17:3727–3738. 28

Pathak HR, Weissinger F, Terunuma M, Carlson GC, Hsu FC, Moss SJ, Coulter DA (2007) Disrupted dentate granule cell chloride regulation enhances synaptic excitability during development of temporal lobe epilepsy. *The Journal of neuroscience : the official journal of the Society for Neuroscience* 27:14012–14022. 18

Patrylo PR, Dudek FE (1998) Physiological unmasking of new glutamatergic pathways in the dentate gyrus of hippocampal slices from kainate-induced epileptic rats. *Journal of Neurophysiology* 79:418–429. 19, 28

Penfield W (1961) Introduction. 2

Pernía-Andrade AJ, Jonas P (2014) Theta-Gamma-Modulated Synaptic Currents in Hippocampal Granule Cells In Vivo Define a Mechanism for Network Oscillations. *Neuron* 81:140–152. 17

Queiroz CM, Gorter JA, Lopes da Silva FH, Wadman WJ (2009) Dynamics of evoked local field potentials in the hippocampus of epileptic rats with spontaneous seizures. *Journal of Neurophysiology* 101:1588–1597. 12

Ratzliff A, Santhakumar V, Howard A, Soltesz I (2002) Mossy cells in epilepsy: rigor mortis or vigor mortis? *Trends in Neurosciences* 25:140–144. 39

Riban V, Bouilleret V, Pham-Lê BT, Fritschy JM, Marescaux C, Depaulis A (2002) Evolution of hippocampal epileptic activity during the development of hippocampal sclerosis in a mouse model of temporal lobe epilepsy. *Neuroscience* 112:101–111. 4, 6, 9, 11

Santhakumar V, Aradi I, Soltesz I (2005) Role of mossy fiber sprouting and mossy cell loss in hyperexcitability: a network model of the dentate gyrus incorporating cell types and axonal topography. *Journal of Neurophysiology* 93:437–453. 19, 29

Santhakumar V, Bender R, Frotscher M, Ross ST, Hollrigel GS, Toth Z, Soltesz I (2000) Granule cell hyperexcitability in the early post-traumatic rat dentate gyrus: the 'irritable mossy cell' hypothesis. *The Journal of physiology* 524 Pt 1:117–134. 18, 39

Scharfman HE, Myers CE (2012) Hilar mossy cells of the dentate gyrus: a historical perspective. *Frontiers in Neural Circuits* 6. 10, 11

Schmidt-Hieber C, Jonas P, Bischofberger J (2004) Enhanced synaptic plasticity in newly generated granule cells of the adult hippocampus. *Nature* 429:184–187. 28

Schwartz SP, Coleman PD (1981) Neurons of origin of the perforant path. *Experimental Neurology* 74:305–312. 17

Seress L, Mrzljak L (1987) Basal dendrites of granule cells are normal features of the fetal and adult dentate gyrus of both monkey and human hippocampal formations. *Brain Research* 405:169–174. 29

Siapas AG, Wilson MA (1998) Coordinated Interactions between Hippocampal Ripples and Cortical Spindles during Slow-Wave Sleep. *Neuron* 21:1123–1128. 3

Sigworth FJ, Sine SM (1987) Data transformations for improved display and fitting of single-channel dwell time histograms. *Biophysical Journal* 52:1047–1054. 8

Sloviter RS (1987) Decreased Hippocampal Inhibition and a Selective Loss of Interneurons in Experimental Epilepsy. *Science (New York, NY)* 235:73–76. 18

Sloviter RS, Bumanglag AV (2013) Defining "epileptogenesis" and identifying "antiepileptogenic targets" in animal models of acquired temporal lobe epilepsy is not as simple as it might seem. *Neuropharmacology* 69:3–15. 12

Sloviter RS, Zappone CA, Harvey BD, Frotscher M (2006) Kainic acid-induced recurrent mossy fiber innervation of dentate gyrus inhibitory interneurons: possible anatomical substrate of granule cell hyper-inhibition in chronically epileptic rats. *The Journal of comparative neurology* 494:944–960. 3, 18

Song H, Kempermann G, Overstreet-Wadiche LS, Zhao C, Schinder AF, Bischofberger J (2005) New neurons in the adult mammalian brain: synaptogenesis and functional integration. *The Journal of neuroscience : the official journal of the Society for Neuroscience* 25:10366–10368. 27

Spigelman I, Yan XX, Obenaus A, Lee EY, Wasterlain CG, Ribak CE (1998) Dentate granule cells form novel basal dendrites in a rat model of temporal lobe epilepsy. *Neuroscience* 86:109–120. 29

Staba RJ (2012) *Normal and Pathologic High-Frequency Oscillations* Jasper's Basic Mechanisms of the Epilepsies. National Center for Biotechnology Information (US), Bethesda (MD), 4th edition. 18

Staba RJ, Wilson CL, Bragin A, Jhung D, Fried I, Engel J (2004) High-frequency oscillations recorded in human medial temporal lobe during sleep. *Annals of Neurology* 56:108–115. 3, 12, 15

Stables JP, Bertram E, Dudek FE, Holmes G, Mathern G, Pitkänen A, White HS (2003) Therapy discovery for pharmacoresistant epilepsy and for disease-modifying therapeutics: summary of the NIH/NINDS/AES models II workshop. In *Epilepsia*, pp. 1472–1478. National Institute of Neurological Disorders and Stroke, National Institutes of Health, Bethesda, MD 20892, USA. 2

Staley KJ, Dudek FE (2006) Interictal Spikes and Epileptogenesis. *Epilepsy Currents* 6:199–202. 17

Stegen M, Young CC, Haas CA, Zentner J, Wolfart J (2009) Increased leak conductance in dentate gyrus granule cells of temporal lobe epilepsy patients with Ammon's horn sclerosis. *Epilepsia* 50:646–653. 37

Steward O, Scoville SA (1976) Cells of origin of entorhinal cortical afferents to the hippocampus and fascia dentata of the rat. *The Journal of comparative neurology* 169:347–370. 17

Sun C, Mtchedlishvili Z, Bertram EH, Erisir A, Kapur J (2007) Selective loss of dentate hilar interneurons contributes to reduced synaptic inhibition of granule cells in an electrical stimulation-based animal model of temporal lobe epilepsy. *The Journal of comparative neurology* 500:876–893. 18

Sutula T, Cascino G, Cavazos J, Parada I, Ramirez L (1989) Mossy fiber synaptic reorganization in the epileptic human temporal lobe. *Annals of Neurology* 26:321–330. 3, 10, 19

Suzuki F, Junier MP, Guilhem D, Sørensen JC, Onteniente B (1995) Morphogenetic Effect of Kainate on Adult Hippocampal-Neurons Associated with a Prolonged Expression of Brain-Derived Neurotrophic Factor. *Neuroscience* 64:665–674. 4, 9

Tashiro A, Zhao C, Gage FH (2006) Retrovirus-mediated single-cell gene knockout technique in adult newborn neurons in vivo. *Nature Protocols* 1:3049–3055. 29, 30

Tauck DL, Nadler JV (1985) Evidence of functional mossy fiber sprouting in hippocampal formation of kainic acid-treated rats. *The Journal of neuroscience : the official journal of the Society for Neuroscience* 5:1016–1022. 3, 7, 10, 19, 28

Thind KK, Ribak CE, Buckmaster PS (2008) Synaptic input to dentate granule cell basal

dendrites in a rat model of temporal lobe epilepsy. *The Journal of comparative neurology* 509:190–202. 29, 35

Toni N, Laplagne DA, Zhao C, Lombardi G, Ribak CE, Gage FH, Schinder AF (2008) Neurons born in the adult dentate gyrus form functional synapses with target cells. *Nature Neuroscience* 11:901–907. 27

van Praag H, Schinder AF, Christie BR, Toni N, Palmer TD, Gage FH (2002) Functional neurogenesis in the adult hippocampus. *Nature* 415:1030–1034. 27

Volz F, Bock HH, Gierthmuehlen M, Zentner J, Haas CA, Freiman TM (2011) Stereologic estimation of hippocampal GluR2/3- and calretinin-immunoreactive hilar neurons (presumptive mossy cells) in two mouse models of temporal lobe epilepsy. *Epilepsia* 52:1579–1589. 4, 9, 10, 11, 18, 39

von Campe G, Spencer DD, de Lanerolle NC (1997) Morphology of dentate granule cells in the human epileptogenic hippocampus. *Hippocampus* 7:472–488. 28

Wadman WJ, Juta AJ, Kamphuis W, Somjen GG (1992) Current source density of sustained potential shifts associated with electrographic seizures and with spreading depression in rat hippocampus. *Brain Research* 570:85–91. 12

Walter C, Murphy BL, Pun RYK, Spieles-Engemann AL, Danzer SC (2007) Pilocarpine-Induced Seizures Cause Selective Time-Dependent Changes to Adult-Generated Hippocampal Dentate Granule Cells. *The Journal of neuroscience : the official journal of the Society for Neuroscience* 27:7541–7552. 29

Wieser HG, ILAE Commission on Neurosurgery of Epilepsy (2004) ILAE Commission Report. Mesial temporal lobe epilepsy with hippocampal sclerosis. In *Epilepsia*, pp. 695–714. Department of Neurology, University Hospital Zurich, Zurich, Switzerland. 4

Wuarin JP, Dudek FE (1996) Electrographic seizures and new recurrent excitatory circuits in the dentate gyrus of hippocampal slices from kainate-treated epileptic rats. *The Journal of neuroscience : the official journal of the Society for Neuroscience* 16:4438–4448. 19, 28

Ylinen A, Bragin A, Nádasdy Z, Jandó G, Szabo I, Sik A, Buzsáki G (1995a) Sharp Wave-Associated High-Frequency Oscillation (200-Hz) in the Intact Hippocampus - Network and Intracellular Mechanisms. *The Journal of neuroscience : the official journal of the Society for Neuroscience* 15:30–46. 14

Ylinen A, Soltesz I, Bragin A, Penttonen M, Sik A, Buzsáki G (1995b) Intracellular correlates of hippocampal theta rhythm in identified pyramidal cells, granule cells, and basket cells. *Hippocampus* 5:78–90. 18

Young CC, Stegen M, Bernard R, Müller M, Bischofberger J, Veh RW, Haas CA, Wolfart J (2009) Upregulation of inward rectifier K+ (Kir2) channels in dentate gyrus granule cells in temporal lobe epilepsy. *The Journal of physiology* 587:4213–4233. 37

Zhang W, Buckmaster PS (2009) Dysfunction of the dentate basket cell circuit in a rat model of temporal lobe epilepsy. *The Journal of neuroscience : the official journal of the Society for Neuroscience* 29:7846–7856. 19

Zhao CS, Overstreet-Wadiche LS (2008) Integration of adult generated neurons during epileptogenesis. *Epilepsia* 49 Suppl 5:3–12. 38

Zhao C, Teng EM, Summers RG, Ming Gl, Gage FH (2006) Distinct morphological stages of dentate granule neuron maturation in the adult mouse hippocampus. *The Journal of neuroscience : the official journal of the Society for Neuroscience* 26:3–11. 27